DOE/BC/14852-10
Distribution Category UC-122

SCALE-UP OF MISCIBLE FLOOD PROCESSES FOR HETEROGENEOUS RESERVOIRS

Second Annual Report

By
Franklin M. Orr, Jr.

March 1995

Work Performed Under Contract No. DE-AC22-92BC14852

Prepared for
U.S. Department of Energy
Assistant Secretary for Fossil Energy

Jerry Casteel, Project Manager
Bartlesville Project Office
P.O. Box 1398
Bartlesville, OK 74005

Prepared by
Stanford University
Petroleum Engineering Department
Stanford, California 94305-2220

DISCLAIMER

DISCLAIMER

Portions of this document may be illegible in electronic image products. Images are produced from the best available original document.

Abstract

Progress is reported for a comprehensive investigation of the scaling behavior of gas injection processes in heterogeneous reservoirs. The interplay of phase behavior, viscous fingering, gravity segregation, capillary imbibition and drainage, and reservoir heterogeneity is examined in a series of simulations and experiments.

Use of streamtube to model multiphase flow is demonstrated to be a fast and accurate approach for displacements that are dominated by reservoir heterogeneity. The streamtube technique is particularly powerful for multiphase compositional displacements because it represents the effects of phase behavior with a one-dimensional flow and represents the effects of heterogeneity through the locations of streamtubes.

A new approach for fast calculations of critical tie-lines directly from criticality conditions is reported. A global triangular structure solution for four-component flow systems, whose tie-lies meet at the edge of a quanternary phase diagram or lie in planes is presented. Also demonstrated is the extension of this solution to multicomponent systems under the same assumptions.

The interplay of gravity, capillary and viscous forces on final residual oil saturation is examined experimentally and theoretically. The analysis of vertical equilibrium conditions for three-phase gravity drainage shows that almost all oil can be recovered from the top part of a reservoir. The prediction of spreading and stability of thin film is performed to investigate three-phase gravity drainage mechanisms. Finally, experimental results from gravity drainage of crude oil in the presence of CO_2 suggest that gravity drainage could be an efficient oil recovery process for vertically fractured reservoirs.

Acknowledgements

This report summarizes work by an extended group of Stanford students, faculty, and research staff. The range of physical mechanisms considered testifies to their versatility: experiments, simulations, and analytical theory for flow of complex mixtures and phases, instabilities, heterogeneities, gravity and capillary forces. The richness of the physical interactions we study is an indication of the range of intellectual interaction we are fortunate to share.

Special credit for this report goes to Dengen Zhou, who took responsibility for assembling the completed package from a large set of computer files, cryptic editorial remarks, and annotated text fragments. He also contributed substantially to much of the work reported, especially the analysis of three-phase flow and gravity drainage in Chapter 4. MS student Bruno Aleónard contributed a significant section on his calculation of critical loci and minimum miscibility pressures. Marco Thiele and Prof. Martin Blunt report on their new and very efficient technique for simulations for heterogeneous reservoirs. Prof. Blunt also contributed to research on three-phase flow and gravity drainage. MS student Darryl Fenwick reports on calculations of film behavior to investigate three-phase flows in gas injection processes.

All of us also thank Yolanda Williams, Pat Ota, and Jeanne Mankinen for their significant support of our work. Their careful attention to the financial, purchasing, and communications aspects of our project gives the researchers the time needed for research.

The work reported here was much influenced by many conversations and assistance from our colleagues in Petroleum Engineering at Stanford. In particular, we are indebted to Khalid Aziz, Bill Brigham, Tom Hewett, Roland Horne, André Journel, and, of course, their students, for creating an unsurpassed environment for research.

The research described here was supported by the U.S. Department of Energy under Grant No. DE-FG22-92BC14852. We thank Tom Wesson, Jerry Casteel and their colleagues at the Bartlesville Project Office for their continued interest and support. In addition, twelve companies provided support through the Stanford Gas Injection Affiliates Program: AGIP/RIGR, Arco Oil and Gas Co., BP Exploration Co. Ltd., Chevron Oil Field Research Co., Conoco Inc., Exxon Production Research Co., Japan National Oil Corporation, Mobil Oil Corporation, Norsk Hydro, Petronas, Texaco Inc., and UNOCAL. They have our heartfelt thanks, as well.

We are also indebted to Norsk Hydro for allowing Thormod Johansen to collaborate with me and former Ph.D. student Birol Dindoruk on the mathematical theory of multiphase, multicomponent flow.

Lynn Orr
Stanford
October 1994

Contents

List of Tables

List of Figures

1. Introduction

When gas injected into an oil reservoir at high pressure, a richly complex set of physical mechanisms comes into play. Components transfer between oil and gas phases, viscous fingers form, geological heterogeneities move fluids in wonderfully complicated ways, and capillary and gravity forces drive flows. In this report, we examine the scaling of the interactions of those mechanisms. The goal of the work is to provide a base of physical understanding upon which can be built the design of gas injection processes for heterogeneous reservoirs.

In Chapter 2 we describe an efficient technique for calculating the performance of a gas injection process in a heterogeneous reservoir. The method is a version of a streamtube technique, in which the effects of heterogeneity in a two-dimensional porous medium are represented by flow through a series of streamtubes while the effects of the displacement process, whether it is a miscible flood, a waterflood or a compositional displacement, are represented by a one-dimensional solution for that displacement process. Thus, this approach decouples the calculation of the physical mechanisms of the displacement process from the representation of the effects of macroscopic heterogeneities. The effects of changing mobilities are included by updating the locations of streamtubes periodically. The technique works best for flows in which heterogeneities influence strongly the flow path of injected fluids, a situation that is common in field-scale flows. We demonstrate the approach for a variety of displacement processes and show that it is orders of magnitude more efficient than conventional finite difference simulation.

In Chapter 3 we consider how multicontact miscibility develops in multicomponent systems. Standard theory for development of miscibility is based on analysis of three-component systems, and minimum miscibility pressures (MMP's) or minimum enrichments for miscibility (MME's) are often calculated by mixing cell methods that determine when either the injection gas or displaced oil lies on a critical tie line. Those methods fail for systems with more than three components if development of miscibility is controlled by tie lines other than the injection or initial tie lines. That situation arises for condensing/vaporizing gas drives, which arise in many CO_2 floods and in the displacement underway at Prudhoe Bay, for example. In Chapter 3 we describe a new technique for direct calculation of the MMP for such situations. The new method works well for condensing/vaporizing gas drives, and it is significantly more efficient than other approaches in widespread use. Also in Chapter 3 we report additional results of mathematical analysis of multicomponent systems that will guide the development of a theory for systems with an arbitrary number of components.

In Chapter 4, we examine in some detail how capillary, gravity, and viscous forces interact to determine residual oil saturations. The goal here is to determine what conditions are required to give low residual saturations and then to see how those conditions can be created by designing gas injection processes appropriately. In the first part of Chapter 3 we develop a theoretical basis for observations that both viscous forces and gravity forces can contribute to reduction of residual oil saturations, and we report additional experimental observations that support the theory. Then we consider the important area of three-phase flow. We examine when and how oil films form on water in the presence of gas, and we consider how those films transport oil due to viscous and gravity forces. Finally, we report experimental results of gravity drainage of crude oil in the presence of high pressure CO_2. Those results suggest that high pressure gas injection processes can be used to recover oil from fractured reservoirs.

The combination of experimental and theoretical results presented here is part of a comprehensive investigation of the scaling of gas injection processes for heterogeneous reservoirs. This report raises as many questions as it answers, an inevitable situation for research that is thoroughly

"in progress." Nevertheless the progress reported here represents a significant step toward the goal of improved design capability based on understanding of the scaling of the underlying physical mechanisms of flow.

2. Modeling Multiphase Flow in Heterogeneous Media Using Streamtubes

Marco R. Thiele and Martin J. Blunt

2.1 Introduction

The primary objective of the streamtube approach is to enable fast, yet accurate numerical solutions to displacements through strongly heterogeneous systems while retaining the details of the underlying physical models seen in one-dimensional solutions. The fundamental assumption in using the streamtube approach rests on the belief that field scale displacements are dominated by reservoir heterogeneity: by capturing flow paths and their relative importance as one-dimensional transport conduits between wells, while honoring the physical displacement mechanism along these conduits, allows difficult enhanced oil recovery displacements to be modeled successfully. Fast and slow flow regions in the reservoir can be represented using quasi one-dimensional streamtubes. Streamtubes can be visualized as an array of pipes, having variable geometries and connecting the injector and producer wells. The shape of each pipe (streamtube) is dictated by the reservoir geology and, most importantly, each pipe is assumed to conserve mass: what goes into a pipe must come out.

The motivation for this research originated from recent advances in the one-dimensional theory of multicomponent, two-phase, compositional displacements [67, 30, 100] and a desire to extend the sophisticated physical models to two-dimensional heterogeneous systems. Traditional numerical solutions to two- and three-dimensional compositional problems are prohibitively expensive, while returning less than satisfactory solutions due to substantial numerical errors. Motivation for a fast numerical technique was also sparked by the now established statistical methods used in reservoir description. Many equiprobable realizations of a particular reservoir, conditioned possibly on log data, core analysis, and seismic data, allow probabilities to be attached to cumulative oil recoveries, but processing the hundreds of geostatistical realizations using traditional reservoir simulation techniques is numerically very expensive, if not impossible. The streamtube approach, on the other hand, allows just that: capturing the first order effect of reservoir heterogeneity, while requiring orders of magnitude less computation time, opening up the opportunity to very rapid evaluation of displacement efficiencies and a statistical approach to reservoir forecasting [122, 123].

Streamlines and streamtubes are well established in the general field of subsurface fluid flow modeling and have given rise to a large body of literature. Unfortunately, the groundwater and petroleum literatures have evolved quite independently from each other and little cross referencing has taken place on the subject. In part, this is due to the difference in the fundamental problem the two fields are concerned with: regional, single phase flow with emphasis on aquatic chemistry in groundwater mechanics versus confined, multiphase, multicomponent flow in petroleum engineering. Important contributions in the petroleum literature are due to Higgins and Leighton [54, 55], Higgins *et al.* [56], Parsons [104], Martin and Wegner [84], Lake *et al.* [76], Emanuel *et al.* [38], and Hewett and Behrens [53]. A comprehensive review of the relevant literature as well additional details of the approach outlined in this report are given by Thiele [122] and Thiele *et al.* [123].

Streamtubes and The Riemann Approach

The method used for modeling modeling multiphase, multicomponent displacement mechanisms centers on the idea of a streamtube as a quasi one-dimensional object. Two-dimensional solutions are then constructed by mapping one-dimensional solutions to the appropriate mass conservation equations along each streamtube. Because the streamtubes are treated as one-dimensional objects, the conservation equations are solved using Riemann boundary conditions (for which analytical solutions can be found) and mapped along streamtubes as Riemann solutions. For any new time step, the solution along a streamtube is always found by integrating from 0 to $t_D + \Delta t_D$ rather than from t_D to $t_D + \Delta t_D$. Mapping the one-dimensional solution in this manner along the streamtubes is referred to as the 'Riemann approach' throughout the text.

Nonlinearity

The fundamental difficulty in solving the partial differential equations (PDE's) governing the flow through porous media is their nonlinear formulation. In other words, in order to account for the relevant physics of fluid flow, the coefficients that appear in the governing equations (relative permeabilities, viscosities, densities, etc...) become functions of the independent variables of the problem, usually phase saturations and/or overall compositions. A special case occurs when the coefficients are assumed constant with respect to the independent variables[1], as is done in unit mobility ratio (M=1) flow. In that case the streamtubes are fixed with time and the flow is said to be linear. To account for the inherent nonlinearity of all other displacements, the streamtube approach periodically updates the streamtubes (i.e. solves the elliptic PDE for the streamfunction) and maps the one-dimensional solution to the particular transport problem onto the new streamtubes using the Riemann approach. This approach is different from the method introduced by Higgins and Leighton [54, 55], where the streamtubes are assumed to be fixed and the nonlinearity is accounted for by changing the flow rate of each streamtubes according to its resistance. The term 'nonlinearity' is used here to specifically identify the changing velocity field with time, as reflected by the dependence of the total mobility coefficients in the elliptic PDE for the streamfunction on saturation and/or compositions.

Class of Problems

The streamtube approach is meant to solve problems that are dominated by reservoir heterogeneity and convective forces. Only cross-sectional problems are discussed here, although there are no dimensional limitations and the method can be used in areal, multiwell configurations as well as in three dimensions[2]. In the examples considered here, solutions by the streamtube approach are restricted to problems with constant initial and injected conditions (Riemann boundary conditions). Finally, the one-dimensional nature of the streamtubes requires transverse flow mechanisms (normal to the streamtube boundaries) to be of negligible importance.

[1] Although the coefficients may still vary spatially like permeability, for example.

[2] Although not as easily derived as in two-dimensions, three dimensional streamtubes arise by considering the intersection of stream surfaces [7]. Once a three-dimensional streamtube is defined, all the arguments with regard to mapping one-dimensional solutions along a streamtube in two dimensions can be applied directly to a streamtube in three dimensions.

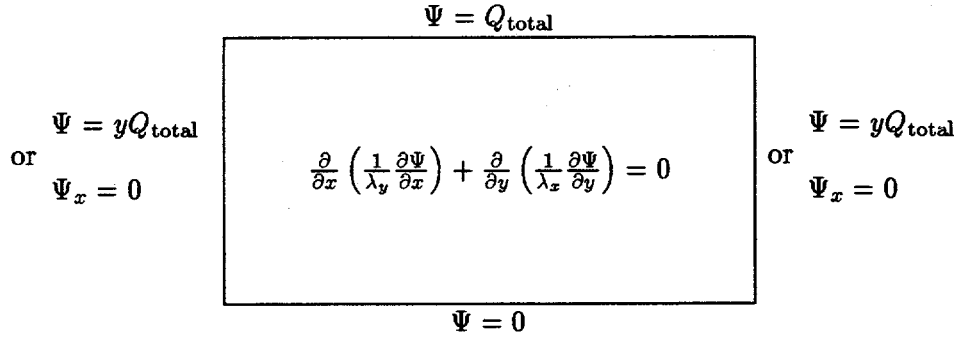

Figure 2.1: *Possible boundary conditions of the streamfunction* Ψ.

2.2 The Mathematics of Streamtubes

Streamtubes can be found by solving directly for the streamfunction using [7]

$$\frac{\partial}{\partial x}\left(\frac{1}{\lambda_y}\frac{\partial \Psi}{\partial x}\right) + \frac{\partial}{\partial y}\left(\frac{1}{\lambda_x}\frac{\partial \Psi}{\partial y}\right) = 0 \ , \tag{2.1}$$

where λ_x and λ_y are the total mobilities in the x and y direction given by

$$\lambda_x = \sum_{j=1}^{N_p} \frac{k_x k_{rj}}{\mu_j} \ ; \ \lambda_y = \sum_{j=1}^{N_p} \frac{k_y k_{rj}}{\mu_j} \ . \tag{2.2}$$

j is the phase index, N_p is the total number of phases present, k_x and k_y are the absolute permeabilities in the x- and y-direction respectively, k_{rj} the phase relative permeability, and μ_j the phase viscosity.

For cross-sectional domains the boundary conditions for Eq. 2.1 are particularly easy to formulate (Fig. 2.2), since the flow rate between two streamlines is simply given by the difference in value of the streamfunction associated with each streamline. Thus, since the top and bottom no flow boundaries and are themselves streamlines, the difference in the value of the streamfunction between the two must equal to the total flowrate. An obvious choice then is to set the bottom boundary to $\Psi = 0$ and the top boundary to $\Psi = Q_{\text{total}}$[3]. Similarly, a uniform rate distribution along the inlet or outlet face must be given by a linear distribution of Ψ from 0 to Q_{total}. Thus,

$$\Psi_{\text{in/out}} = yQ_{\text{total}} \ ; \ 0 \leq y \leq 1 \ . \tag{2.3}$$

To find the equivalent of a constant pressure/total rate boundary condition in terms of the streamfunction it is necessary to consider the Cauchy-Riemann equation

$$\frac{1}{\lambda_y}\frac{\partial \Psi}{\partial x} = -\frac{\partial P}{\partial y} \ .$$

A constant pressure boundary states that gradient in the y direction must be zero. For a nonzero coefficient λ_y^{-1} it follows that

$$\frac{\partial P}{\partial y} = 0 \implies \frac{\partial \Psi}{\partial x} = 0 \ . \tag{2.4}$$

[3]Clearly, the opposite choice is just as good.

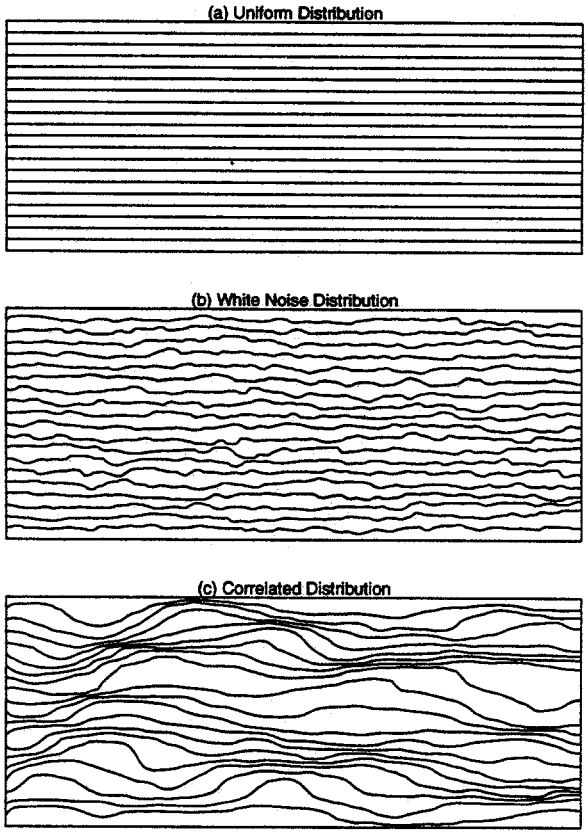

Figure 2.2: Streamtube geometries as a function of permeability correlation. From top to bottom: (a) homogeneous distribution , (b) white noise (no correlation), and (c) correlated permeability field.

Total flow is automatically honored by the value associated with the top and bottom limiting streamlines. The two possible boundary conditions for the the inlet and outlet end are summarized in Fig. 2.1. Once the streamfunction has been solved for the particular heterogeneous domain of interest, streamtubes are defined by considering two adjacent streamlines. A system of N streamlines will define $N-1$ streamtubes.

The advantage of using streamtubes versus streamlines as the fundamental object on which to map a one dimensional solution is that streamtubes offer a visual interpretation of the local flow velocity whereas streamlines do not. By tracing a single streamline from inlet to outlet nothing is yet known about how fast a particle moves along that streamline. A streamtube on the other hand, allows identification of slow and fast flow regions: thick sections of a streamtube correspond to slow flow regions, thin sections to fast flow regions. The geometry of the streamtubes therefore captures the distribution of the flow velocity imposed by the underlying permeability field as demonstrated in Fig. 2.2. The correlated permeability field in Fig. 2.2 was generated using a moving window algorithm [122].

2.3 Tracer Displacements

For tracer displacements the elliptic equation governing the potential flow field is decoupled from the mass conservation equations. The problem is linear and consequently the streamtubes are fixed in time and must be solved for only once. Two possible analytical solutions can be mapped along streamtubes in the tracer case: (1) a no-diffusion solution given by an indifferent

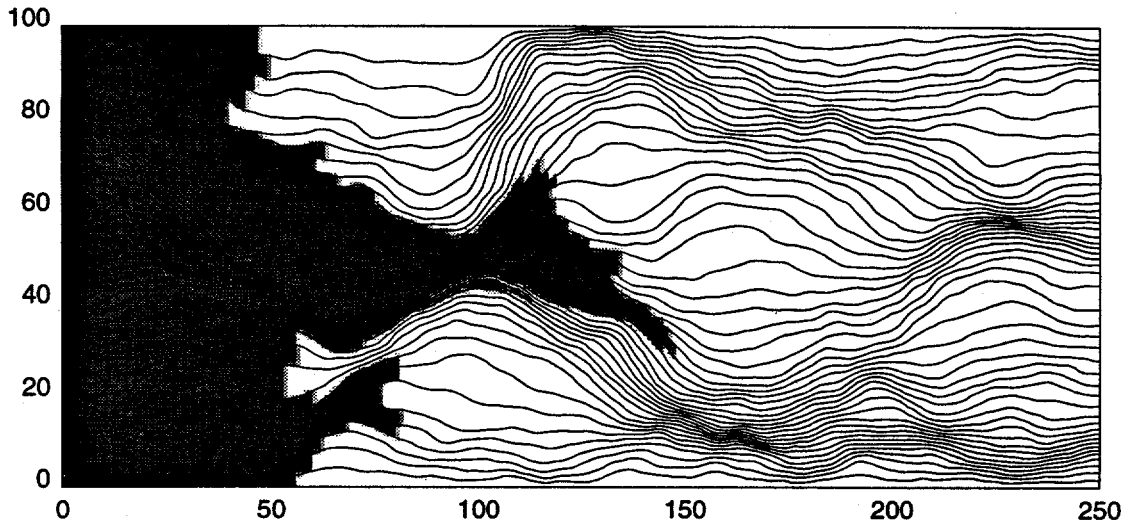

Figure 2.3: Example solution for the two dimensional domain by mapping the diffusion-free tracer solution at $t_D = 0.3$ along streamtubes.

wave traveling at unit velocity, expressed mathematically as

$$C_D(x_D, t_D) = \begin{cases} 1 & \text{for } x_D \leq t_D \\ 0 & \text{for } x_D \geq t_D \end{cases} \tag{2.5}$$

and (2) a convection-diffusion solution given by

$$C_D(x_D, t_D) = \frac{1}{2}\text{erfc}\left(\frac{x_D - t_D}{2\sqrt{\frac{t_D}{N_{Pe}}}}\right) \quad . \tag{2.6}$$

C_D, x_D, and t_D are the usual definitions of dimensionless concentration, distance, and time, and N_{Pe} is the Peclet number, a dimensionless number expressing the extent of physical diffusion/dispersion. The larger the Peclet number the less diffusion/dispersion exists. Field-scale Peclet numbers can range from 10–10,000 [6]. An example tracer solution for a heterogeneous reservoir of 250x100 grid blocks using 50 streamtubes and the no-diffusion solution (Eq. 2.5) is shown in Fig. 2.3. Using Eq. 2.6, on the other hand, allows the addition of physical longitudinal diffusion to the two-dimensional solution of Fig. 2.3. Example solutions at $t_D = 0.3$ and three Peclet numbers ($N_{Pe} \rightarrow \infty$, $N_{Pe} = 1000$, and $N_{Pe} = 100$) are shown in Fig. 2.4. It is important to realize that mapping Eq. 2.6 can not account for transverse diffusion.

Scale of the 2D Solution

Mapping a convection-diffusion solution onto the streamtubes attaches a length scale to the heterogeneous system. For a low variance, second-order stationary, permeability field the Peclet number may be expressed as [94, 45, 23]

$$N_{Pe} \propto \frac{1}{\sigma^2}\frac{L}{L_{rep}} \quad , \tag{2.7}$$

where σ^2 is the variance of the permeability field, L is the system length, and L_{rep} is a representative length scale beyond which the system looks 'diffusive' (or Fickian). The question in applying in the

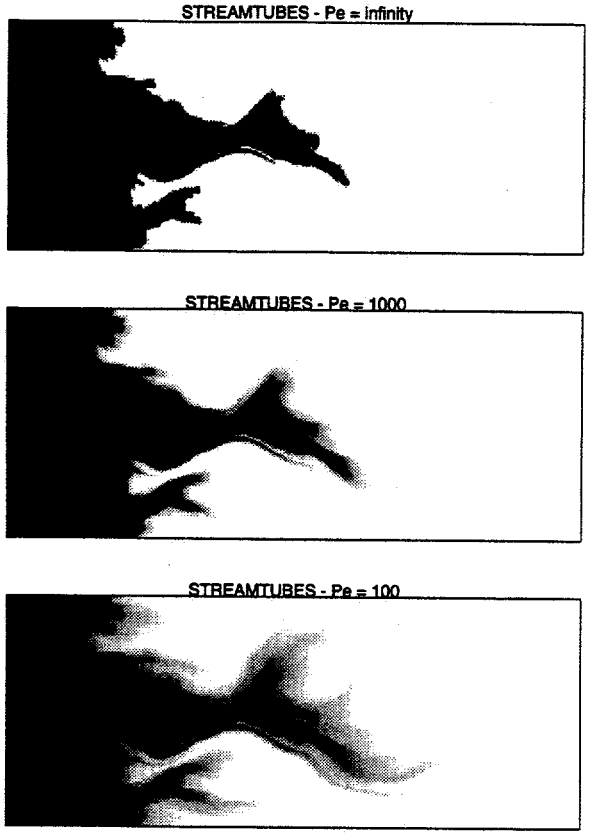

Figure 2.4: Including physical diffusion in M=1 displacement by mapping the convection-diffusion equation along each streamtube. Examples at $N_{Pe} \rightarrow \infty$, $N_{Pe} = 1000$, and $N_{Pe} = 100$.

CD–model to field–scale streamtubes is whether a sub–field scale L_{rep} exists that allows the CD–solution to hold along field–scale streamtubes. Considering that the streamtubes, by definition, will conform to the flow units (heterogeneity) of the system, the assumption of treating each streamtube as a pseudo-homogeneous unit that reaches a diffusive limit is not unreasonable. In other words, a small L_{rep} does not necessarily preclude the streamtubes to be on a field scale. For example, successful matching of field tracer data using this approach has been demonstrated by Abbaszadeh–Dehghani [1]. Thus, mapping the CD-model along field-scale streamtubes is an attempt to capture sub-tube heterogeneities which are represented numerically by specifying an appropriate Peclet number. It represents a 'nested' approach to modeling heterogeneities that dominate at different scale: the streamtubes capture the large-scale heterogeneities of the reservoir while the CD-solution models sub-grid block/sub-streamtube features.

Quantifying Numerical Diffusion

Mapping analytical solutions, such as Eq. 2.5 or Eq. 2.6, onto streamtubes results in two-dimensional solutions that are completely devoid of numerical diffusion. Streamtubes solutions can therefore be used to quantify the extent of numerical diffusion in other numerical solutions obtained using finite differences or finite elements. An example of a such comparison is given in Fig. 2.5, which shows the tracer solution without physical diffusion at $t_D = 0.3$ compared to solutions with no physical diffusion (but some numerical diffusion) obtained using Mistress, a BP research code with flux corrected transport[4] [19] and Eclipse, a commercially available reservoir simulator with single point upstream weighting. In the limit of a large number of streamtubes, the streamtube solution is the exact limiting solution for the no diffusion case, and can be used to calculate the

[4]Using Courant–Friedrichs–Lewy (CFL) number of 0.2.

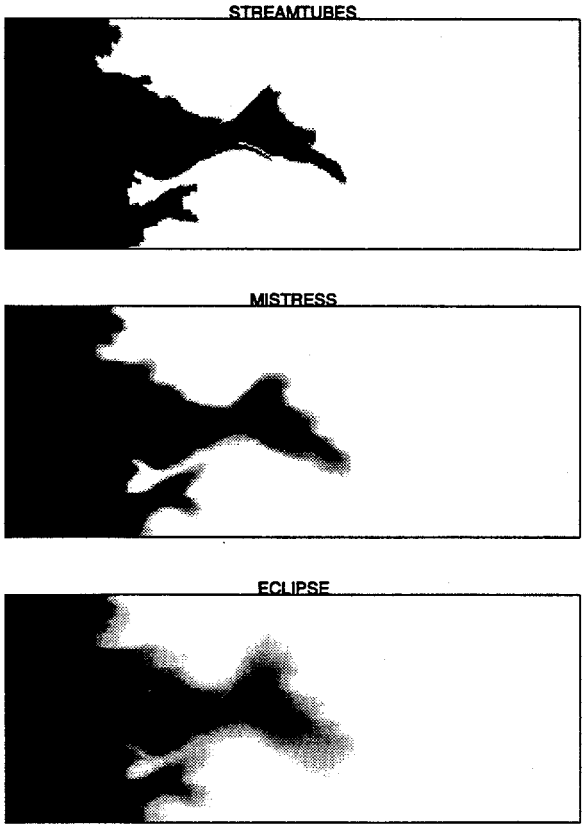

Figure 2.5: Comparison of concentration profiles showing extent of numerical diffusion in finite difference simulators. Streamtube method versus Mistress, a BP research code with flux corrected transport and Eclipse, a commercially available reservoir simulator with single point upstream weighting and automatic time step selection.

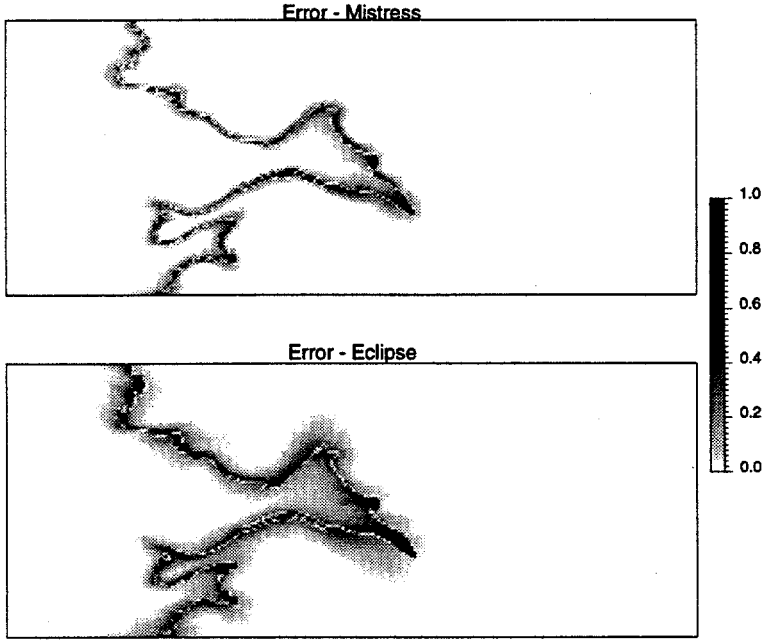

Figure 2.6: Spatial distribution of the error caused by numerical diffusion in the Mistress and Eclipse simulations shown in Fig. 2.5.

spatial error

$$\Delta C_{\text{err}} = \mid C(x,y)_{\text{Stubes}} - C(x,y)_{\text{FD}} \mid \ , \tag{2.8}$$

where the subscript FD stands for finite difference. A spatial rendering of ΔC_{err} is shown in Fig. 2.6. The results shown in Fig. 2.5 demonstrate that numerical solutions are clearly affected by numerical diffusion, although the basic flow pattern dictated by the permeability field is arguably the same in all cases.

2.4 Immiscible Displacements

When Higgins and Leighton [54, 55] introduced the streamtube approach as a method to predict two–phase flow in a five–spot pattern, they reported excellent agreement with experimental data for mobility ratios ranging from 0.083 to 754. Other authors [56, 33, 80, 84] also reported good matches with either field or laboratory data for similar values of mobility ratios. All authors were able to account for the nonlinearity inherent in the total velocity field by keeping the streamtubes fixed and adjusting the flowrates instead. In this work, the waterflood problem is approached differently and used principally to demonstrate the applicability of the proposed Riemann approach to more difficult multiphase, multicomponent displacements.

The principal difference to work done by previous authors lies is in the mapping of the one-dimensional solution along periodically changing streamtubes. In the Riemann approach, the one-dimensional solution is treated as a solution to a Riemann problem, although the streamtubes change with time. The solution along a new streamtube for the time level $t_D + \Delta t_D$ is not given by an integration from t_D to $t_D + \Delta t_D$, as in conventional time-stepping algorithms, but rather as an integration from 0 to $t_D + \Delta t_D$, where the initial conditions are assumed to be constant right and left states. Thus, the Riemann approach centers on treating each streamtube as a true one-dimensional system on which the Buckley-Leverett solution is mapped repeatedly for different times, the difference to the tracer case being that the streamtubes are now updated periodically. The underlying assumption in the Riemann approach is that the fluid entering a streamtube remains in the streamtube and exits only at the outlet end, even if the streamtube changes location and geometry as a function of time.

Reasons for the Riemann Approach

A legitimate question is to ask what motivates the Riemann approach. The answer centers on the attempt to capture the nonlinearities that exist in multiphase flow. Only three authors Martin *et al.* [85], Martin and Wegner [84], Renard [107] address the idea of updating the streamtubes rather than using total flow resistance. Mathematically, updating the streamtubes is an appealing approach because local flow velocities are updated, and the original definition of a streamtube as carrying a volumetric rate equal to the difference in the value of its bounding streamlines is maintained. However, updating the streamtubes poses one problem related to the initial conditions associated with each streamtube: each time a streamtube is updated it must be initialized so that the conservation equation(s) can be solved. The only reasonable possibility to assign new initial conditions along an updated streamtube is to use the old, two–dimensional saturation distribution on the underlying cartesian grid. Because updating a streamtube literally means changing its position in x–y space, it is easy to see that the new initial conditions will not correspond to the old saturation distribution along the streamtube. The resulting hyperbolic problem that must be solved then will be one with general type initial conditions. No analytical solutions exist for such problems and the saturation distribution along the new streamtube can be moved forward in time (1) numerically by using a standard one–dimensional finite–difference solution along each streamtube [13], or (2) by using a moving interface, front–tracking algorithm [112, 32, 48, 14]. The

Riemann approach, on the other hand, completely circumvents the problem of initial conditions that arises with streamtube updating. The two–dimensional solution is approximated by N one–dimensional solutions along streamtubes that are treated as true Riemann solutions along changing streamtubes.

The 1D Buckley–Leverett Solution

The one-dimensional Buckley–Leverett solution is well known and well documented in the petroleum literature [16, 24, 77] and is generally used in its dimensionless form

$$\frac{\partial S_w}{\partial t_D} + \frac{\partial f_w}{\partial x_D} = 0 \ , \tag{2.9}$$

where $t_D = tu_t/L$ and $x_D = \phi x/L$ are usual definitions of dimensionless time and distance respectively, u_t is the total (constant) Darcy velocity given by $u_t = u_w + u_o$, and f_w is the fractional flow of water given by

$$f_w = \frac{u_w}{u_w + u_o} = \frac{1}{1 + \frac{k_{ro}\mu_w}{k_{rw}\mu_o}} \ . \tag{2.10}$$

k_{ro}, k_{rw}, μ_o, and μ_w are the relative permeabilities and viscosities of oil and water as indicated by the subscript[5]. The solution to Eq. 2.9 subject to Riemann conditions of the form

$$S_w(x_D, 0) \begin{cases} S_{wl} & \text{for } x_D \leq 0 \\ S_{wr} & \text{for } x_D \geq 0 \end{cases} \ , \tag{2.11}$$

where the subscripts l and r refer to the left and right constant states of the discontinuity at $x_D = 0$, can be found easily using the method of characteristics [132, 82]. Depending on the shape of the fractional flow curve, f_w, the solution can contain rarefaction waves and shocks, which are found using the velocity constraint and the entropy condition [66]. A rarefaction wave is composed of saturations having characteristic velocities given by

$$\frac{dx_D}{dt_D} = \frac{df_w}{dS_w} \ , \tag{2.12}$$

whereas a shock travels with a characteristic velocity given by

$$\frac{dx_D}{dt_D} = \frac{f_w^U - f_w^D}{S_w^U - S_w^D} \ . \tag{2.13}$$

The superscripts U and D stand for upstream and downstream respectively. An example solution for a two–phase problem with and end–point mobility ratio of 10 is shown in Fig. 2.7.

Validation of the Riemann Approach

The Riemann approach was tested by the following numerical experiment. Using a standard finite difference simulator (Eclipse), the velocity fields were stored for regular increments of dimensionless time. From each velocity field, the corresponding streamtubes were then constructed and used to find the saturation profiles by mapping a Riemann solution along the streamtubes for that particular time. The saturation profiles obtained by this method were then compared to the saturation profiles obtained by the direct Riemann approach.

The one–dimensional solution used to test the Riemann approach is shown in Fig. 2.7. Although the end-point mobility ratio is 10, the shock–front mobility ratio is, in fact, only 1.36,

[5] Eq. 2.10 assumes that the one–dimensional porous medium is homogeneous.

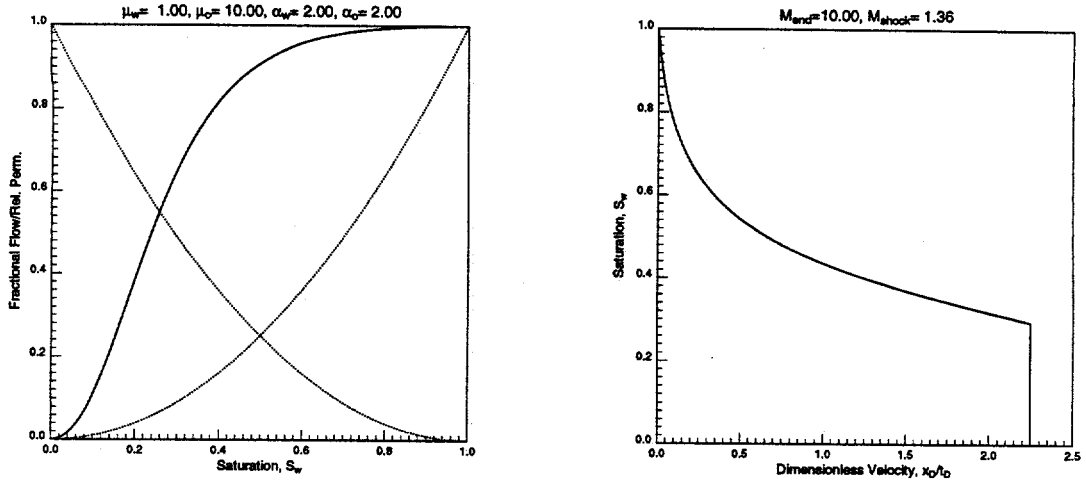

Figure 2.7: Relative permeability curves ($k_{rw} = S_w^2$, $k_{ro} = S_o^2$), corresponding fractional flow function for a viscosity ratio of 10 ($\mu_o = 10$, $\mu_w = 1$), and Buckley–Leverett analytical solution used for testing the Riemann approach. The mobility ratio at the shock front is $M_{\text{shock}} = 1.36$.

resulting in a more stable displacement than suggested by the end-point value alone. This is generally true for many waterfloods with 'reasonable' relative permeability curves: the frontal mobility ratio is of order 1 even though the end-point can be of order 10 or 100 leading to a weak nonlinearity in the total velocity.

As demonstrated in Fig. 2.8, the Riemann approach agrees well with the mixed method (Eclipse velocity field + Riemann approach), and both solutions have no numerical diffusion because an analytical one-dimensional solution is used along the streamtubes. Figure 2.8 displays example solutions at $t_D = 0.2$ and $t_D = 0.4$. The upper row shows saturations maps obtained directly from Eclipse; the middle row shows maps obtained using the velocity from Eclipse but mapping the solution using the Riemann approach; and the last row shows profiles obtained by using the Riemann approach only.

A direct comparison of saturation maps (Fig. 2.8) as well as the integrated response (Fig. 2.9) demonstrate that the difference between the two methods (Eclipse velocity field + Riemann approach and direct Riemann approach) is indeed small, and the nonlinearity of the velocity field is captured correctly by the direct Riemann approach. In fact, it is interesting to note that numerical diffusion causes a larger difference in recovery between the two methods than the approximation involved by using the Riemann approach. This conclusion can be drawn from the fact that the velocity fields for the two recovery curves are identical and therefore the difference must be attributed to numerical diffusion. That numerical diffusion has the upper hand in the Eclipse solution is also suggested by the comparison of the saturation histories shown in Fig. 2.10. This numerical experiment suggests that the error in the velocity field caused by the Riemann approach is indeed small compared to traditional finite difference solutions. In particular, numerical diffusion is shown to cause larger errors than the assumption used in the Riemann approach.

Convergence of the Riemann Approach

In the streamtube approach the conservation equation is not discretized and therefore there is no Courant–Friedrichs–Lewy (CFL) condition to worry about. The question of how many times

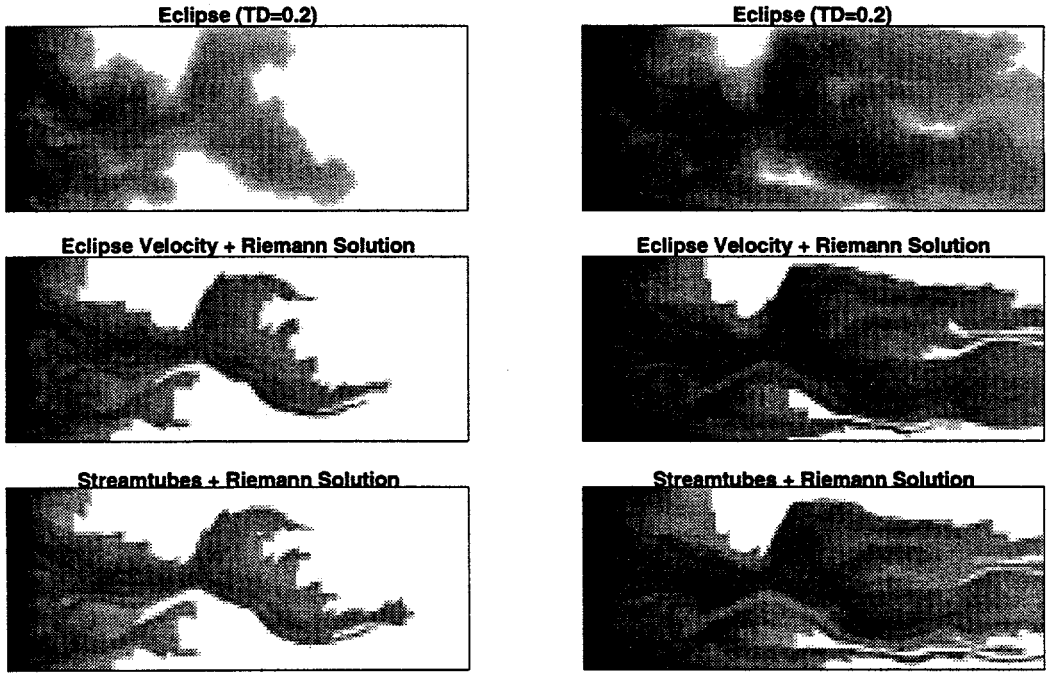

Figure 2.8: Saturation maps at times $t_D = 0.2$ and $t_D = 0.4$. From top to bottom: profiles obtained directly from Eclipse; profiles obtained by using the velocity field from Eclipse but mapping a Riemann solution along streamtubes; profiles obtained by the method proposed in this work.

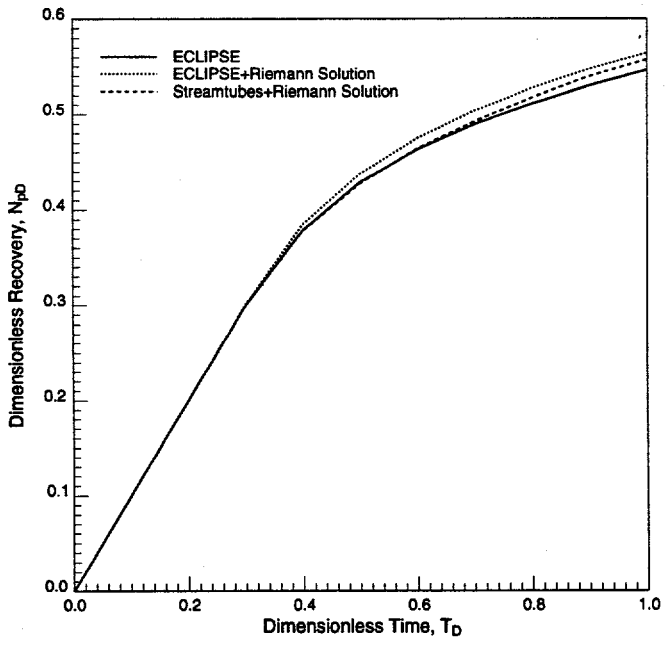

Figure 2.9: Recovery curves for the three different solution methods used to generate the profiles in Fig. 2.8.

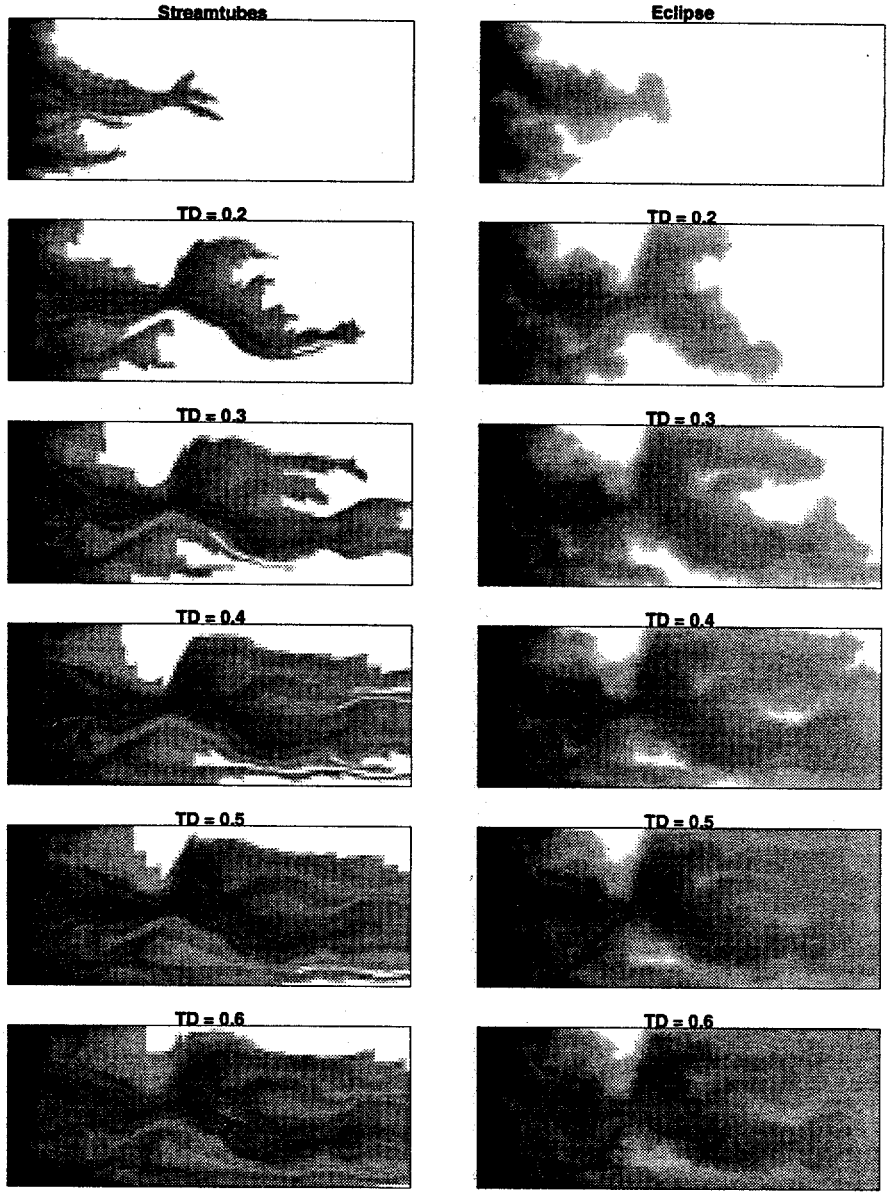

Figure 2.10: Displacement history at $\Delta t_D = 0.1$ intervals for a Buckley–Leverett problem with a fractional flow given by Fig. 2.7.

the streamtubes must be updated to consider the solution converged arises naturally and is addressed by solving the previous problem repeatedly with an increasing number of streamtube updates. Recovery curves for 1, 10, 20, 40, and 100 streamtube updates are shown in Fig. 2.11. It is rather surprising to find that 20 solves are sufficient to consider the problem converged over a range of two pore volumes injected ($t_D = 0.2$). With only 20 solves, the new approach represents a reduction in computation time by two orders of magnitude compared to the thousands of solves needed by a traditional finite difference simulator like Eclipse. For this particular problem ($M_{\text{end}} = 10$), Eclipse required 1600 solves which translates into a speed-up of 8000% .

2.5 First Contact Miscible Displacements

Unstable first contact miscible (FCM) displacements in heterogeneous system have been studied by many authors [5, 20, 49, 114, 128]. An extensive treatment of the subject was recently

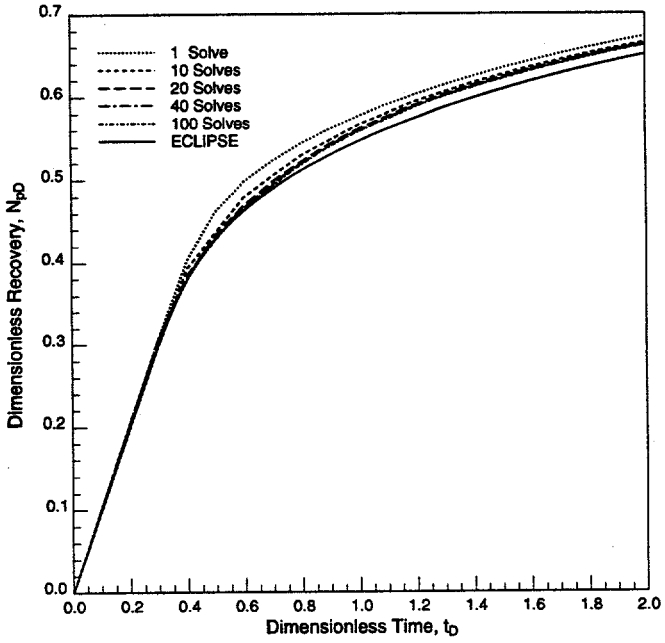

Figure 2.11: Recovery curves for for 1, 10, 20, 40, and 100 streamtube updates over two pore volumes injected ($t_D = 2$) showing that the problem can be considered converged if more than 20 updates are used.

given by Tchelepi [121]. The strong interest in unstable FCM displacements is motivated principally by the possibility of learning more about displacements which are near-miscible, such as gas and carbon-dioxide flooding. The assumptions used in FCM flow isolate the convective part of the displacement problem from any phase behavior considerations and allow to study the interaction of reservoir heterogeneity and the nonlinearity of the total velocity field in determining sweep efficiency. The absence of any phase behavior and multiphase flow aspects, on the other hand, enhances the nonlinearity of the problem. Diffusive mechanisms, such as molecular diffusion and pore scale mixing, are the only physical mechanisms available to mitigate the original mobility contrast. As a result, FCM displacements are very challenging to simulate numerically and are far more difficult than two-phase immiscible problems. High mobility contrasts lead to extreme velocity variations and sufficient grid blocks must be used to ensure that numerical diffusion is as close as possible to representing true physical diffusion at the grid block scale. Thus, physically meaningful simulations of FCM displacements require substantial computer resources [121].

1D Viscous Fingering Solution

Unlike the two-phase immiscible problem, the ideal miscible case has a subtle one-dimensional solution. The solution to the governing PDE (with no-diffusion)

$$\frac{\partial C_D}{\partial t_D} + \frac{\partial C_D}{\partial x_D} = 0 \ . \tag{2.14}$$

with initial data of the type

$$C_D(x_D,0)\begin{cases} 1 & \text{for } x_D \leq 0 \\ 0 & \text{for } x_D \geq 0 \end{cases} , \tag{2.15}$$

gives rise to an indifferent wave solution traveling at unit velocity (as for the tracer case). For favorable mobility ratios ($M < 1$), the 'physical' solution is indeed a wave traveling at unit velocity,

although the wave is no longer indifferent but self-sharpening. For unfavorable mobility ratios, on the other hand, the solution to Eq. 2.14 is misleading because it still gives a piston-like displacement, when the system is in fact unstable. The problem, of course, is that the displacement model given by Eq. 2.14 is unable to distinguish between stable and unstable displacements since it is linear —by not having concentration dependent coefficients, the solution can not account for any viscosity induced mobility contrast as a function of x_D and t_D. Furthermore, Eq. 2.14 has no characteristic length scale, resulting in a sharp, but unstable front at all length scales and for all times. A physically meaningful solution, on the other hand, would require some cut-off length scale across which the frontal instability is mitigated.

Although adding a cut-off length scale can be done mathematically by retaining a second order diffusion term, implying that the cut-off length scale is given by the diffusive length scale associated with N_{Pe}, it is unlikely that at the field scale molecular diffusion and pore level mixing are first-order type physical processes that mitigate instabilities. Convective mixing at the macroscale, such as viscous fingering and channeling are probably more important. To account for such phenomena in an averaged, one-dimensional sense an analogy to two-phase flow was first proposed by Koval [75]. In the Koval model, straight line relative permeabilities and a quarter-power mixing rule are combined to define a flux function $f(C_D)$ that models convective mixing of the fluids. The governing PDE for Koval's model is[6]

$$\frac{\partial C_D}{\partial t_D} + \frac{\partial f(C_D)}{\partial x_D} = 0 \ , \tag{2.16}$$

where $f(C_D)$ is given by

$$f(C_D) = \frac{1}{1 + \frac{1-C_D}{C_D}\frac{1}{M_{\text{eff}}}} \ . \tag{2.17}$$

M_{eff} is the effective mobility ratio defined as

$$M_{\text{eff}} = \left(0.78 + 0.22 M^{1/4}\right)^4 \ , \tag{2.18}$$

and $M = \mu_o/\mu_s$ is the usual definition of the mobility ratio. For combining with streamtubes though, a better one-dimensional model to use is the Todd–Longstaff formulation [75]. The Todd–Longstaff model includes Koval's model as a special case and is a single parameter function given by

$$f(C_D) = \frac{1}{1 + \frac{1-C_D}{C_D}\left(\frac{1}{M}\right)^{1-\omega}} \ . \tag{2.19}$$

If ω is chosen as

$$\omega = 1 - 4\frac{\ln\left(0.78 + 0.22 M^{1/4}\right)}{\ln M} \ , \tag{2.20}$$

the Todd–Longstaff model is equivalent to Koval's model. Setting $\omega = 1$ gives the piston-like, no-diffusion solution, while $\omega = 0$ returns the 'equivalent' two-phase problem using straight line relative permeabilities. Varying ω therefore allows investigation of an entire range of possible solutions for the unstable case. Example fractional flow functions and concentration profiles for an end-point mobility ratio of ten are shown in Fig. 2.12.

The discussion on tracer displacements considered the diffusive length scale introduced by the convection-diffusion model. Choosing a Peclet number introduces a representative length scale, L_{rep}, beyond which the systems is said to be diffusive at the sub-streamtube level. On the other

[6] Koval's original model also includes a heterogeneity factor H. This factor is set to $H = 1$ (homogeneous), since the model is used only to capture viscous fingering in an averaged one-dimensional sense along streamtubes.

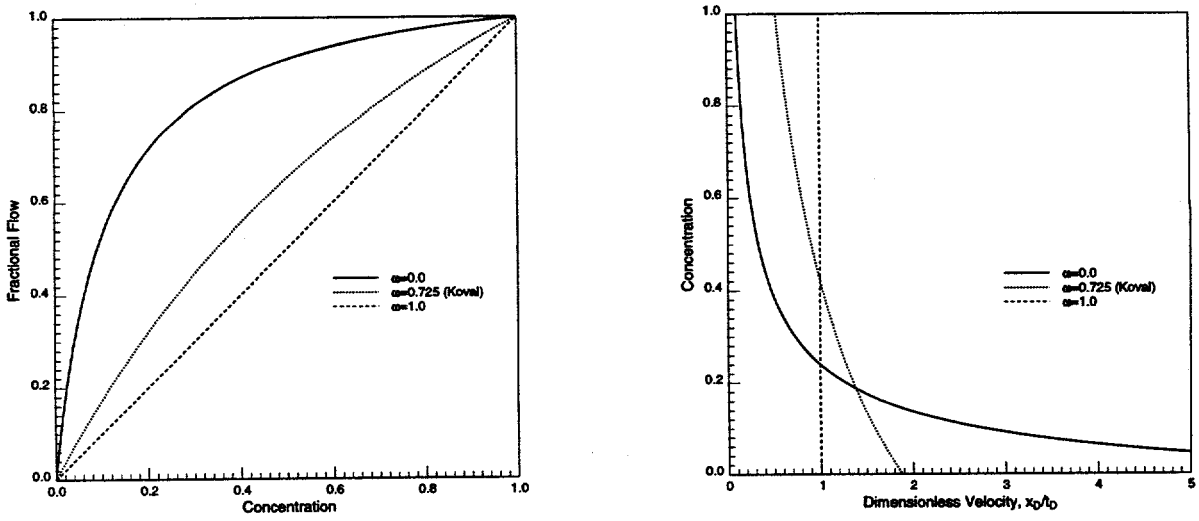

Figure 2.12: Fractional flow curves and corresponding velocity profiles for $M = 10$ and different values of ω in the Todd–Longstaff model.

hand, if a viscous fingering model is used along streamtubes, such as the Todd–Longstaff model, then the scaling argument no longer rest on a diffusive length scale[7]. The most convincing physical argument for attaching a length scale to the two-dimensional streamtube solution is to consider each streamtube as a 'homogeneous' medium that will attain a Fickian limit in the unit mobility ratio case, but will generate viscous fingers for $M > 1$.

Two-Dimensional Solutions

Fig. 2.13 shows example $M = 10$ solutions through 250x100 block cross sections with varying degree of heterogeneity at $t_D = 0.4$. A value of $\omega = 0.725$ was used in each case (equivalent to Koval's model) to capture the viscous fingering induced mixing along each streamtube. The comparison with the Mistress solution in each case raises the interesting question whether the streamtube solutions and the Mistress solutions are indeed on the same scale. All Mistress solutions have some viscous fingering features, whereas all the fingering in the streamtube solutions is assumed to take place within the streamtubes and captured in an averaged one-dimensional sense. As a result, it could be argued that the streamtube solution is probably representing a larger scale than the Mistress solution.

Total recoveries for the six different permeability distributions are summarized in Fig. 2.14. The recovery for the very short correlation length system (PERM 5) is expected to be good, since it amounts to the recovery predicted by the one-dimensional Koval solution. For the other cases, the recovery curves tell an interesting story, particularly for the permeability fields with a heterogeneity index (HI) of $HI = 0.0625$ (PERM 2) and $HI = 0.64$ (PERM 3). The heterogeneity index originated from the work of Gelhar and Axness [45] and has been used by other authors since [86, 5, 114]. HI is defined as

$$HI = \sigma^2_{\ln k} \lambda_c \ , \tag{2.21}$$

where $\sigma^2_{\ln k}$ is the variance of the $\ln k$–field and λ_c is the correlation length in the x–direction. The higher HI, the 'more' heterogeneous the system is said to be. The heterogeneity index is an attractive parameter because it combines information about the variability of the permeability field ($\sigma^2_{\ln k}$) with information about the correlation structure of the heterogeneity (λ_c). The traditional

[7] Although it is possible to argue that the size of viscous fingers may be scaled by L_{rep}.

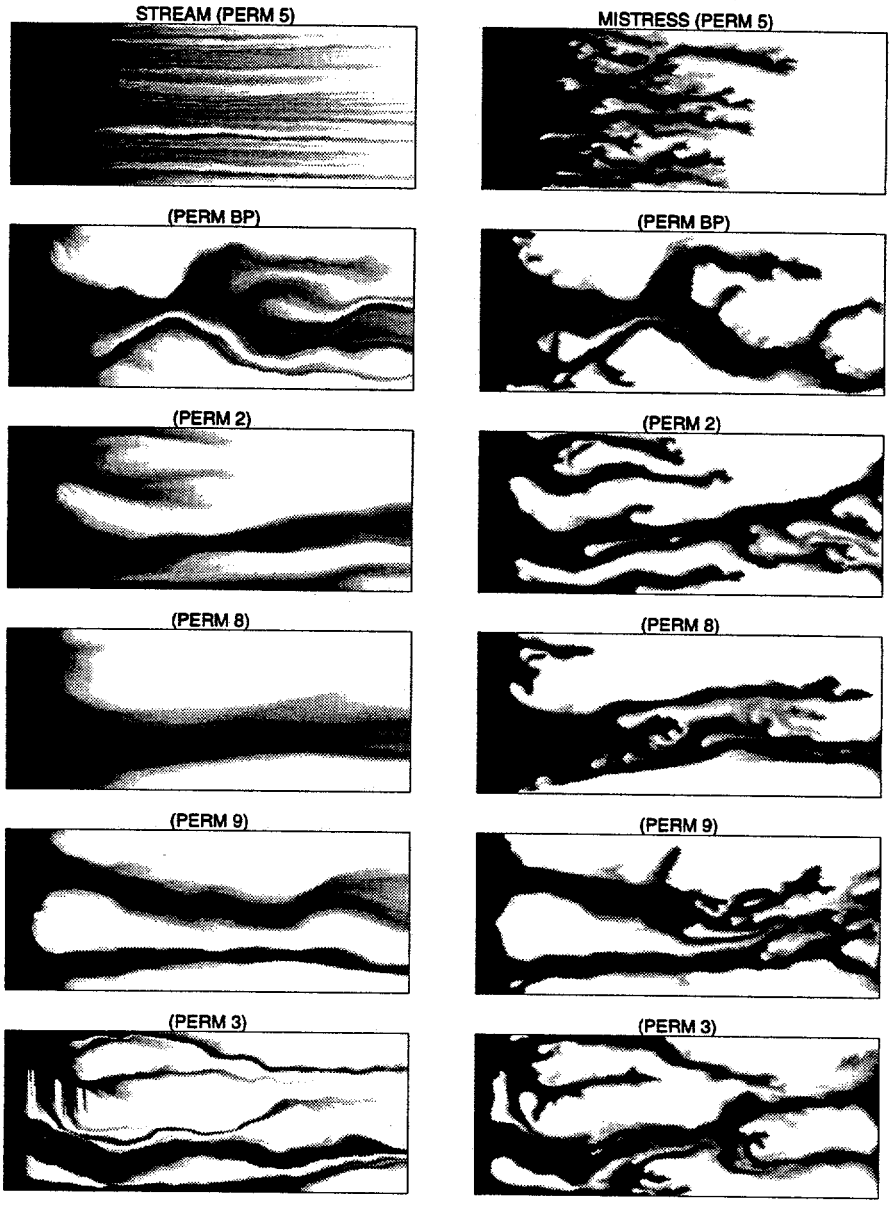

Figure 2.13: Concentration maps for $M = 10$ displacements in six different, 250x100 block heterogeneous reservoirs.

Dykstra–Parson coefficient (V_{DP}) can be recovered from HI by recalling that

$$\sigma_{\ln k} = -\ln(1 - V_{DP}) \ . \tag{2.22}$$

The $HI = 0.0625$ (PERM 2) permeability field has a correlation length of $\lambda_c = 0.25$, but only a standard deviation of $\sigma_{\ln k} = 0.5$. In other words, the system is only mildly heterogeneous and although there are preferential flow channels, the streamtube solution sees a rather homogeneous reservoir, whereas the Mistress solution allows fingers to grow along these channels. The predicted recoveries are, accordingly, higher for the more homogeneous streamtube solution and lower for the viscous fingering dominated Mistress solution. The interesting point about this displacement is that it identifies a flow regime in which the streamtube fails to capture the dominant displacement mechanism: field scale fingering induced by mildly heterogeneous systems.

The much more heterogeneous $HI = 0.64$ (PERM 3) case, on the other hand, behaves quite differently. Heterogeneity is clearly the dominating factor in this displacement, which the streamtube method is able to capture. Mistress also resolves the heterogeneity, but the many fingers,

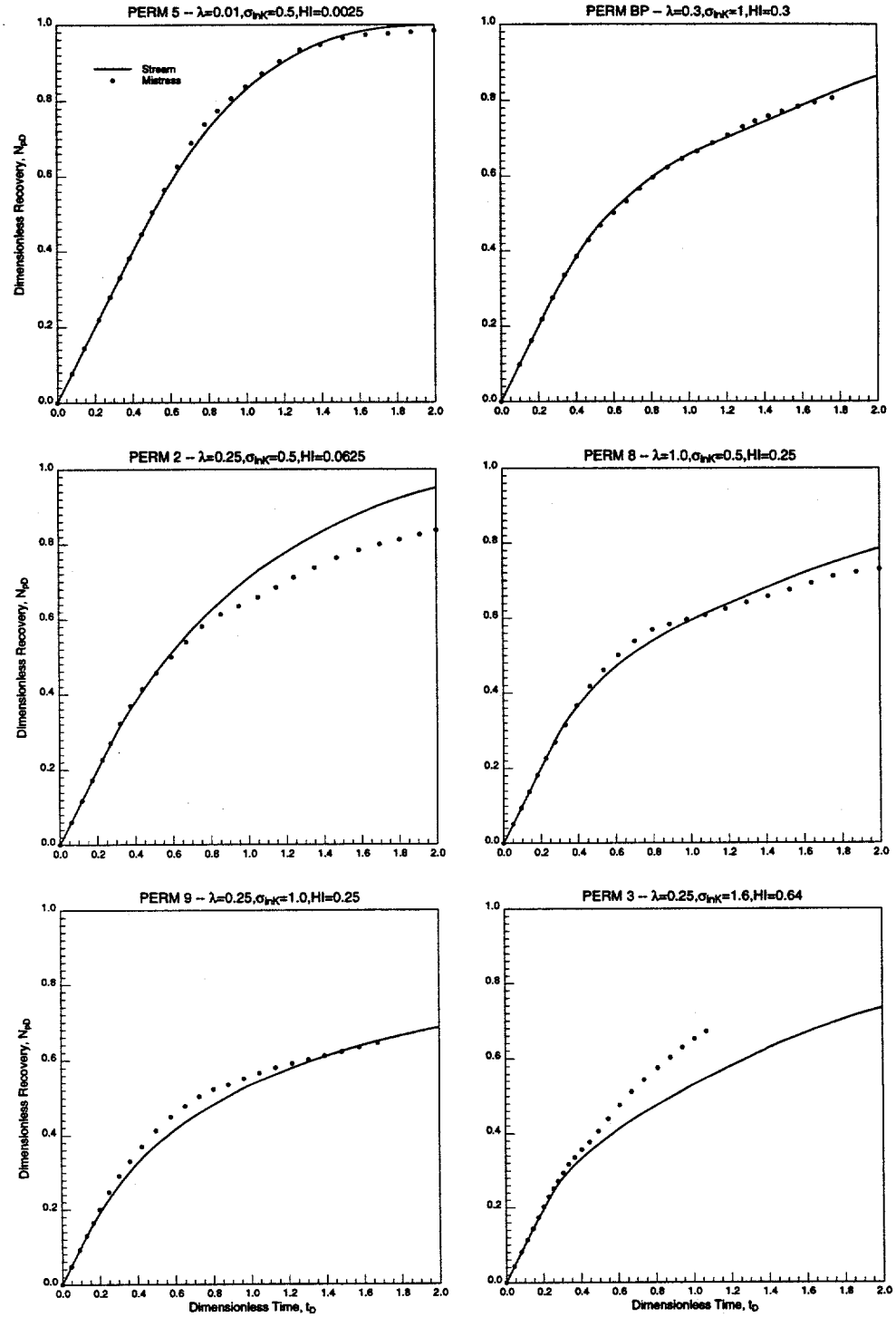

Figure 2.14: Recovery curves for the displacements shown in Fig. 1.12.

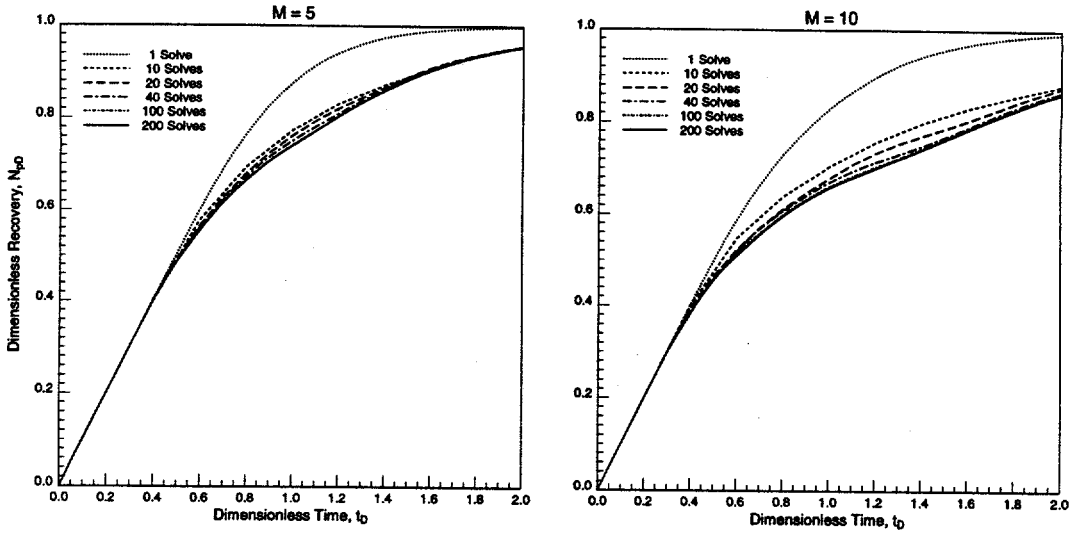

Figure 2.15: Example of the convergence of the 2D solution for the ideal miscible case for end-point mobility ratios of 5 and 10 over two pore volumes injected. The permeability field is 125x100 blocks.

channels, and numerical diffusion cause sufficient 'mixing' to lower the mobility contrast and lead to a substantially higher overall recovery. The flow channels in the Mistress solution are thicker than those present in the streamtube solution, and coalesce leading to higher recoveries. Mistress also had some numerical difficulties with this particular field due to the extreme permeability contrasts, causing the run time to exceed 14000 Cray seconds. Thus the truncated recovery curve. In the remaining cases, the streamtube and Mistress recoveries match, demonstrating the ability of the streamtube approach to capture overall recovery and the main displacement features.

Convergence

As was mentioned previously, the streamtube approach does not have the equivalent of a CFL condition: there is no numerical limitation to the size of the time step and the solution is always numerically stable. Instead, the question of whether the solution has converged must be addressed explicitly through the number of times the streamtubes are updated to capture the nonlinearity in the total velocity field. A solution is considered converged when the overall recovery does not change with increasing number of updates over a fixed total time t_D.

All the solutions presented in this chapter implicitly used 'sufficient' updates for a converged solution. Fig. 2.15 shows overall recoveries as a function of mobility ratio and number of streamtube updates for the one of permeability fields used in Fig. 2.13. In both cases, $M = 5$ and $M = 10$, the solution can be considered converged by using between 40 and 100 streamtube updates over two pore volumes injected. In fact, the big difference in recovery occurs by going from a single solve (tracer case) to 10 updates. Even by using only 20 updates an acceptable solution can be obtained, with breakthrough predicted correctly. Compared to the many thousands of pressure solves required by Mistress, the speed-up in finding the solution is by two orders of magnitude. Herein lies the great advantage of the streamtube approaches. Although it makes strong assumptions in generating the two-dimensional solutions and does not capture the subtleties of viscous fingering, it is nevertheless able to find solutions that contain all the main features imposed by the heterogeneity and return accurate overall recoveries, particularly breakthrough times, using orders of magnitude less CPU time than a traditional finite difference or finite element approach.

Applications

The real power of the streamtube approach lies in its ability to produce solutions that capture the main features imposed by the underlying permeability field while using orders of magnitude less CPU time than traditional simulation techniques. Its strength is not in resolving the details of the displacements, although the control on numerical diffusion may suggest it, but in being able to produce accurate recoveries very quickly. As such, it is ideally suited for a statistical approach to reservoir forecasting. A large number of statistically identical permeability realizations can be processed to generate a spread in recovery for a particular combination of reservoir geology and displacement mechanism. The streamtube approach may also be used as a filter: the permeability fields that returned the maximum and minimum recoveries can be singled out and used in a much more expensive finite-difference simulation to confirm the uncertainty.

The speed of the streamtube approach can be used in many ways, but becomes particularly appealing when a parameter space of interest includes reservoir heterogeneity, in which case many simulations are required to obtain a statistically meaningful answer. An example of a parameter space that has received considerable attention recently [121, 5, 128, 114] has been in the area of unstable displacements through heterogeneous systems. In its most simple representation, the parameter space is given by the end-point mobility ratio (instability) and heterogeneity index HI (heterogeneity), although HI is clearly not a completely satisfactory parameter for quantifying the complex geologic structure of a real reservoir. Nevertheless, HI can give some indication of the degree of heterogeneity of the reservoir, particularly if it is used in a statistical sense. A partial sweep of the parameter space is shown in Fig. 2.16. There are 30 recovery curves for each of the six M-HI pairs. Mobility ratio increases from left to right and heterogeneity increases from top to bottom. All underlying permeability fields have 125x50 grid blocks.

Fig. 2.16 is particularly interesting in that it quantifies how nonlinearity in the velocity field and heterogeneity interact, but does so statistically, rather than using a single recovery for each case. As a result, the weakness of HI as a parameter is traded for a more convincing spread in recovery given by the 30 curves for each case. Some interesting observations may be made from Fig. 2.16: (1) Nonlinearity and reservoir heterogeneity interact to create a spread in recovery that increases with increasing mobility ratio and increasing heterogeneity; (2) of the two parameters, heterogeneity is clearly the dominant factor in establishing recovery, although an increasing mobility ratio causes the spread between minimum and maximum recovery to increase slightly; (3) the most important conclusion to be drawn comes from realizing that the recovery areas partially overlap from one case to the next. A higher heterogeneity index or mobility ratio does not automatically lead to lower recoveries compared to a system with lower heterogeneity or mobility ratio, although on average this conclusion does hold. For example, an $M = 5$-$HI = 0.86$ pair exists that will return a higher recovery then an $M = 10$-$HI = 0.86$ pair.

The 180 recoveries of Fig. 2.17 would have taken a prohibitively long time using a traditional finite difference approach. Instead, if the streamtube approach is used as a filter for the 180 images, the number of solutions required to establish firmly the spread in recoveries is just six — two per case — as shown in Fig. 2.17.

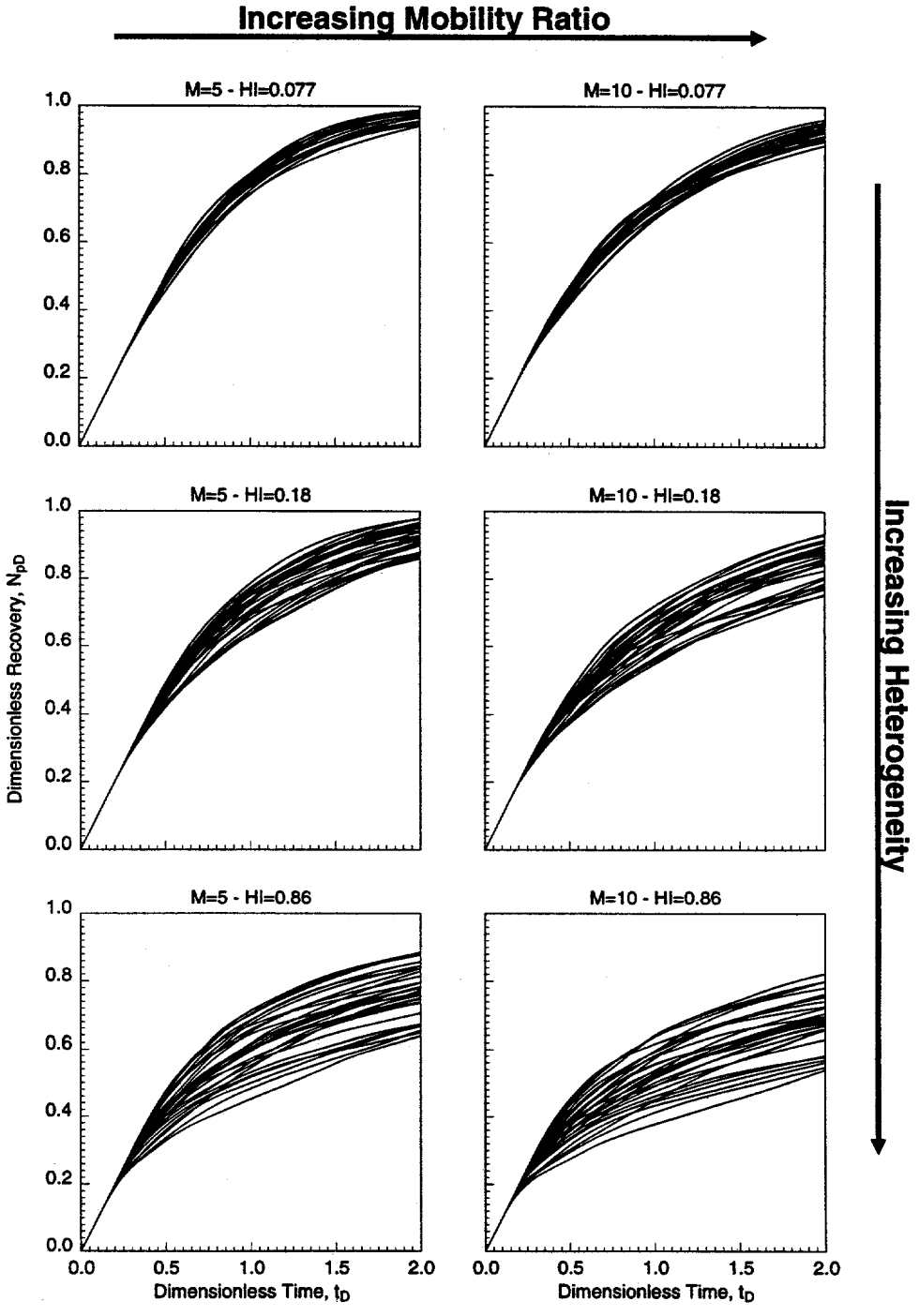

Figure 2.16: 180 recovery curves used in partially sweeping the M-HI parameter space to determine how nonlinearity and heterogeneity interact.

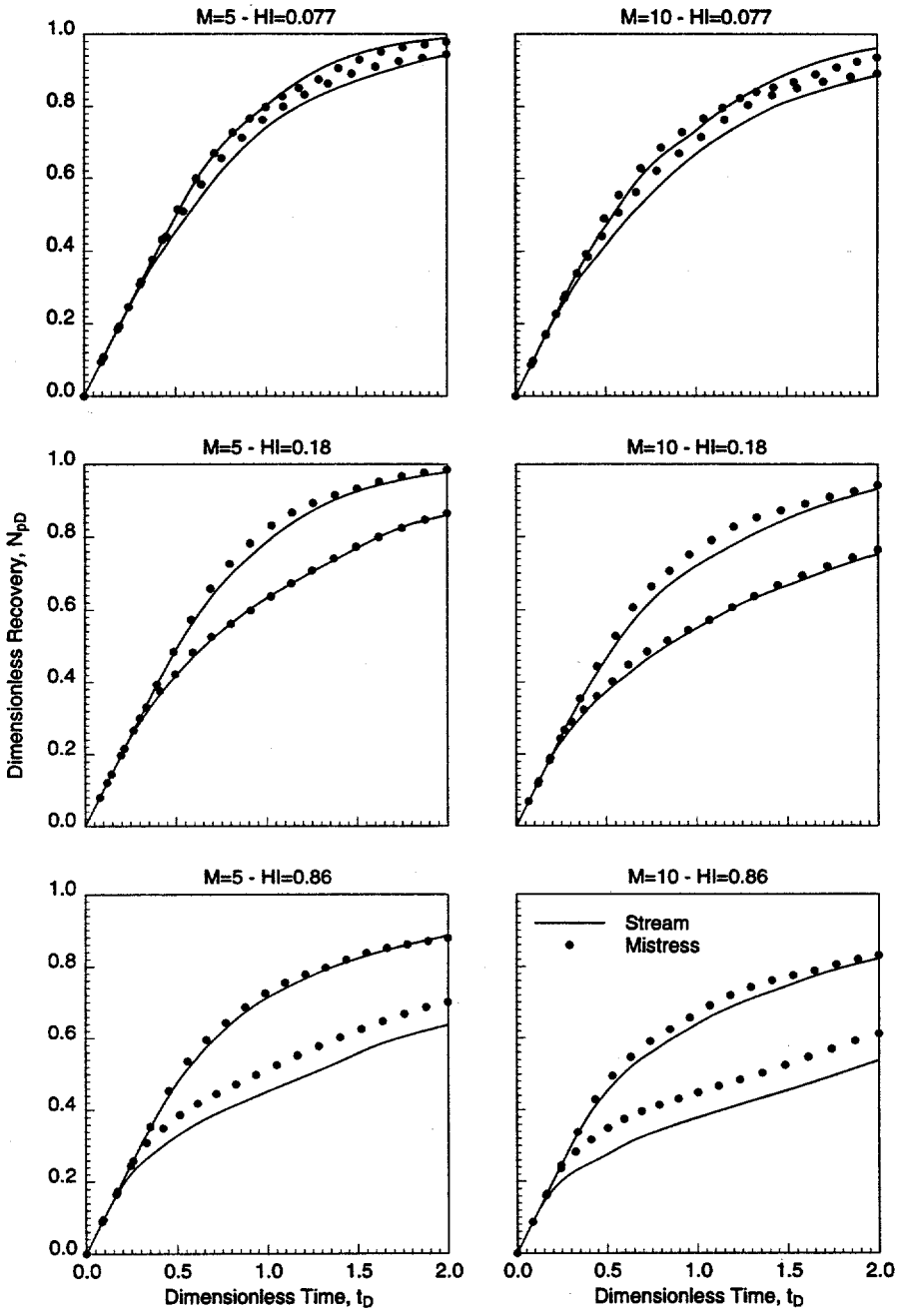

Figure 2.17: Confirming the spread in recoveries predicted by the streamtube approach by running Mistress on permeability fields associated with the maximum and minimum recoveries for each case predicted by the streamtube approach.

2.6 Compositional Displacements

Effects of phase equilibrium add a substantial degree of complexity to compositional displacements over those of two-phase immiscible and ideal miscible flow. The local equilibrium assumption requires a flash calculation for each grid block at every time step, while the traditional difficulties associated with numerical diffusion and frontal instabilities remain. Simulations become enormously expensive and yet may yield less than satisfactory solutions. Compared to the 'simple' physics described by two-phase relative permeabilities in immiscible displacements or the quarter power mixing rule in ideal miscible displacements, phase equilibrium and its coupling to multiphase flow poses daunting numerical difficulties. Because of the large computation times involved, compositional simulations are often run on coarse grids and have substantial amount of numerical diffusion, and can be very difficult to distinguish whether a particular feature is genuinely part of the solution and the physics of the problem or whether it is simply an artifact of the numerical scheme. The problem of numerical diffusion is particularly subtle in compositional simulation because it interacts with the phase behavior to alter displacement performance, sometimes substantially [68, 129, 101].

The streamtube approach is a powerful tool for investigating compositional displacements. With a one-dimensional solution known, the two-dimensional solution for a heterogeneous system can be constructed with the same ease as the tracer, immiscible, or ideal miscible case. Furthermore, because the one-dimensional solution may be calculated numerically using a large number of grid blocks, or analytically for some special cases [67, 30], numerical diffusion is minimized or even completely absent. Computation times are reduced dramatically, since beyond the savings resulting from the comparably small number of streamtube updates required to capture the nonlinear convective part of the displacement, all the phase behavior is contained within the one-dimensional solution that is mapped along the streamtubes. In other words, the phase behavior is completely decoupled from the underlying cartesian grid used to solve for the local flow velocity, and flash calculations are no longer necessary for each grid block. The streamtube also has the substantial advantage of being always numerically stable. Its simple formulation, particularly the decoupling of the phase behavior from the flow field, makes for very robust simulations. The only issue, as in in the displacements described previously, is the number of times the streamtubes must be updated to capture the change in the total mobility field. The simplicity of the streamtube approach is in stark contrast to traditional compositional simulation, which faces significant numerical difficulties, particularly in strongly heterogeneous systems, where extreme differences in local flow velocities impose very small time steps and convergence problems.

Three-Component Solution

As in the displacement mechanisms discussed previously, applying the streamtube technique to model compositional displacements in heterogeneous systems centers on the availability of a one-dimensional solution. Substantial progress on analytical solutions has been reported recently [67, 30, 100, 66, 29, 89, 88], and analytical solutions have been presented for multicomponent problems that have constant initial and injected conditions (Riemann conditions) with either no volume change on mixing [67, 66] or volume change on mixing [30, 29]. For an extensive treatments on the subject the reader is referred to the dissertations of Johns [66] and Dindoruk [29].

An example of a high volatility intermediate (HVI) ternary system is given by $CH_4/CO_2/C_{10}$ at 1600 *psia* and $160°F$. The name 'high volatility intermediate' refers to the strict ordering of the K-values, $K_{CH_4} > K_{CO_2} > K_{C_{10}}$, for all compositions and the fact that the intermediate component K-value is greater than one ($K_{CO_2} > 1$). This means that CO_2 will preferentially reside in the more mobile gas phase. A HVI-system can give rise to either a condensing or vaporizing

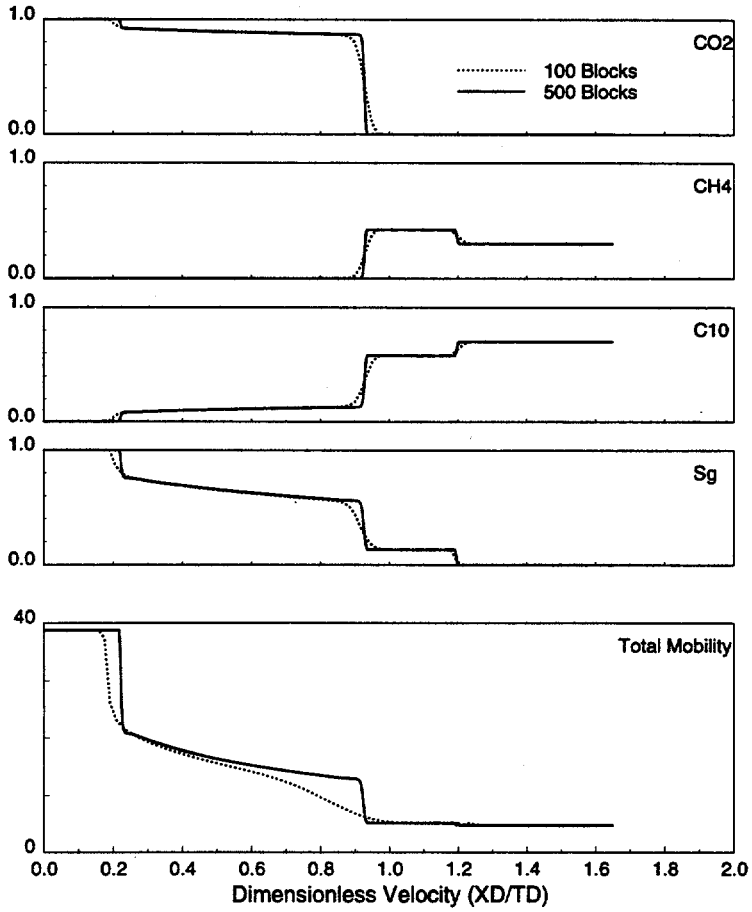

Figure 2.18: UTCOMP one-dimensional numerical solutions using 100 and 500 grid blocks and a third order TVD-scheme to control numerical diffusion, for the $CH_4/CO_2/C_{10}$-condensing gas drive.

drive depending on the initial and injected compositions. The displacement of a 30/70 CH_4/C_{10}-oil by pure CO_2, for example, is a condensing gas drive. Example numerical solutions for the $CH_4/CO_2/C_{10}$-system found using 100 and 500 grid blocks and the third order TVD-option are shown in Fig. 2.18. The reason for finding the one-dimensional solution to the $CH_4/CO_2/C_{10}$-system numerically was to guarantee consistency in the phase behavior representation between the one-dimensional solutions used along the streamtubes and the two-dimensional'reference' solutions found using the same compositional simulator in 2D. The numerical simulator used here was UTCOMP (Version 3.2, 1993) [125], an implicit pressure, explicit saturation (IMPES) type, isothermal, three-dimensional, compositional simulator developed at the University of Texas at Austin. The numerical solutions in Fig. 2.18 capture all the the essential shocks in this condensing gas drive, and particularly the 500-block solution has an acceptable level of numerical diffusion. For streamtube modeling purposes, the total mobility profile is the most important piece of information, because it indicates the strength of the nonlinearity of the total flow velocity and directly ties into the solution of the streamtubes. For this particular case, although the end-point mobility ratio is approximately 8, the mobility ratios across the two fronts, which are separated by a long rarefaction wave, are approximately 2 and 3. In other words, the mobility contrast is reduced considerably by the phase behavior alone. To what extent numerical diffusion may affect total mobility is already anticipated by the disappearance of the leading mobility front due to numerical diffusion in the 100 grid block solution.

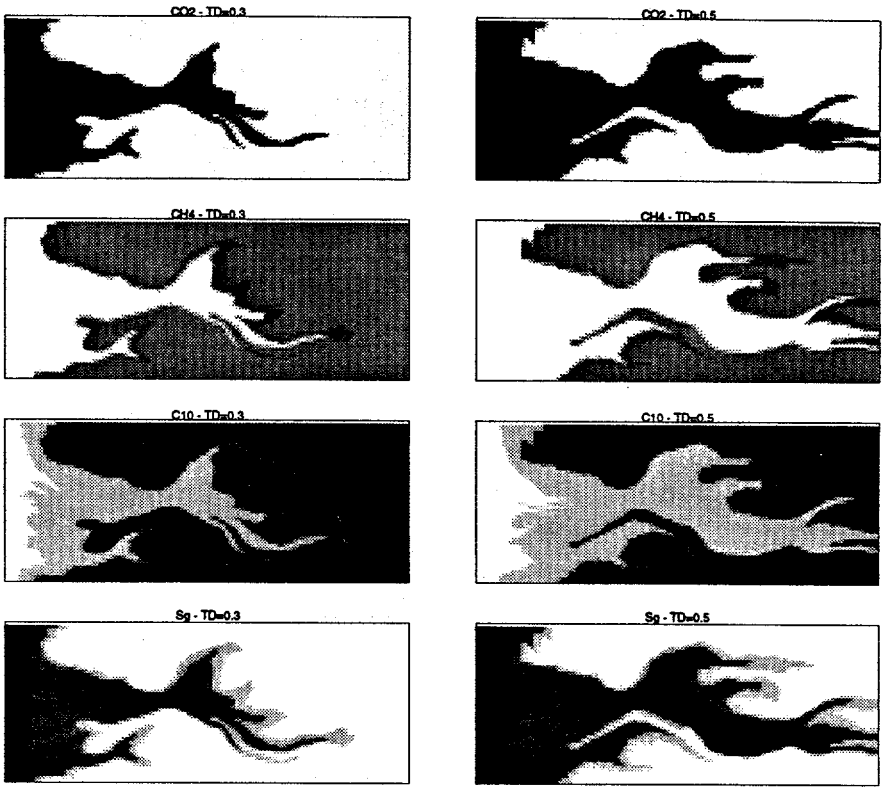

Figure 2.19: Two-dimensional, 3 component condensing gas drive in a 125x50 heterogeneous block reservoir at $t_D = 0.3$ and $t_D = 0.5$. The one-dimensional solution is shown in Fig. 1.17.

2D Solution - 500 Blocks, TVD

An almost diffusion-free compositional solution through a heterogeneous domain can now be found by mapping the 500 grid block, third order, total variation diminishing (TVD) solution along streamtubes. Composition and saturation maps for a 125x50 block heterogeneous reservoir at $t_D = 0.3$ and $t_D = 0.5$ are shown in Fig. 2.19. As expected, the fronts are clearly visible and, although the end-point mobility ratio is $M \approx 8$, the displacement does not suffer from 'instabilities'. The reason for the stability, of course, is that the phase behavior mitigates the initial mobility ratio contrast by creating two weaker fronts which are separated by a long rarefaction wave.

Figs. 2.20 and 2.21 compare the two-dimensional UTCOMP solution found using a third-order TVD scheme to the streamtube solution; Fig. 2.20 compares composition and saturation profiles at $t_D = 0.4$, whereas Fig. 2.21 compares only the gas saturation profiles from $t_D = 0.1$ to $t_D = 0.6$. The agreement is very good, particularly considering that UTCOMP required approximately 5000 Cray seconds per 0.1PV injected, whereas the streamtube solution required approximately 2-3 Cray seconds, a speed-up factor by three orders of magnitude. Both solutions clearly capture the same overall flow characteristics imposed by the underlying heterogeneity field. Fig. 2.20 and Fig. 2.21 are encouraging, because they suggest that the streamtubes can be combined successfully with a one-dimensional compositional solution to model a two-dimensional displacement at a significantly reduced cost, with the error introduced by the Riemann approach remaining sufficiently 'small', and thereby not significantly altering the displacement mechanism.

Although the comparison is good and the streamtube solution looks like a 'sharper' UTCOMP solution, a noticeable difference is the more stable behavior of the UTCOMP solution. This

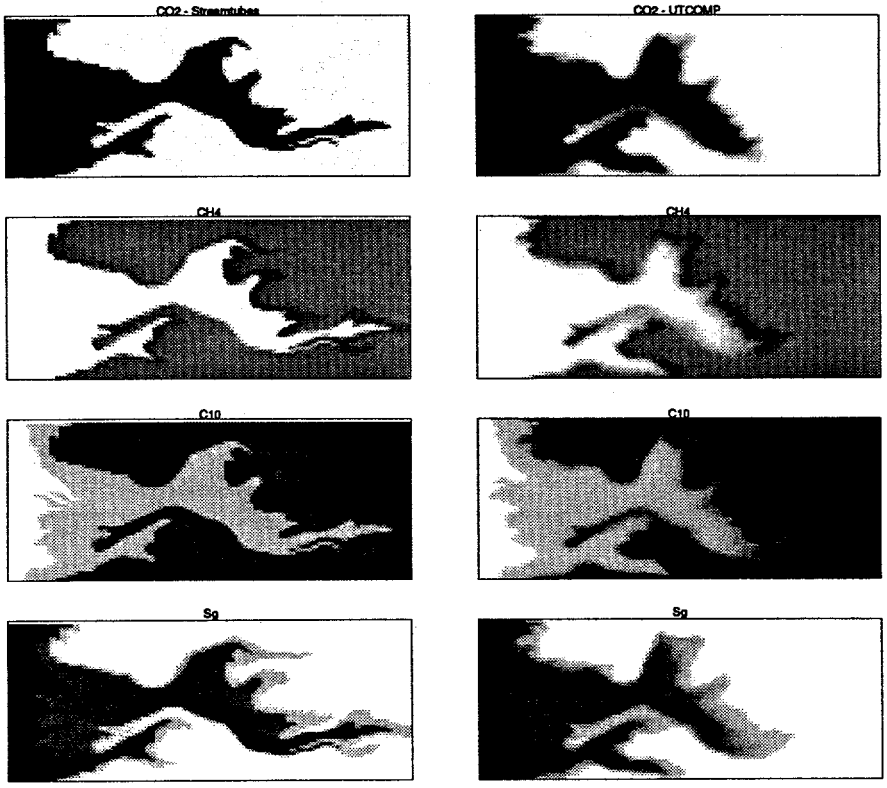

Figure 2.20: Comparison of the streamtube solution with the UTCOMP solution at $t_D = 0.4$. The UTCOMP solution was found using a third-order TVD scheme.

difference raises an important question: is the more stable finite difference solution an artifact due to numerical diffusion, or a genuine physical phenomenon, possibly resulting from mixing due to viscous crossflow? Considering that the number of blocks in the main direction of flow is only 125, and that a TVD-scheme in 2D does not result in them same numerical diffusion control as in 1D, it is possible that numerical diffusion is the main reason for the more stable looking UTCOMP solution. Two additional simulations were performed in an attempt to answer this question: (1) a UTCOMP solution was found for the same 125x50 grid but using a one-point upstream scheme to show the effects of numerical diffusion more clearly, and (2) a diffused one-dimensional compositional solution was mapped along the streamtubes in an attempt to include numerical diffusion in the streamtube solution[8].

(1) - 125x50 1Pt Upstream Solution

Fig. 2.22 compares the UTCOMP one-point upstream weighting solution, to the streamtube solution. The degradation in the UTCOMP solution is considerable compared to the TVD solution, and most importantly, the solution now looks even more stable. The fronts are much more diffused and breakthrough occurs later still than in the TVD solution. Fig. 2.22 is strong evidence that the mitigation of the original mobility contrast in UTCOMP solutions is due to numerical diffusion rather than to crossflow.

[8] A simulation with a refined 250x100 grid and a third-order TVD scheme, while maintaining the same heterogeneity structure, was attempted using UTCOMP as well. Unfortunately, computation costs approached 70,000 Cray seconds ($\approx 20hr$) per 0.1 PV injected, forcing the simulation to be terminated.

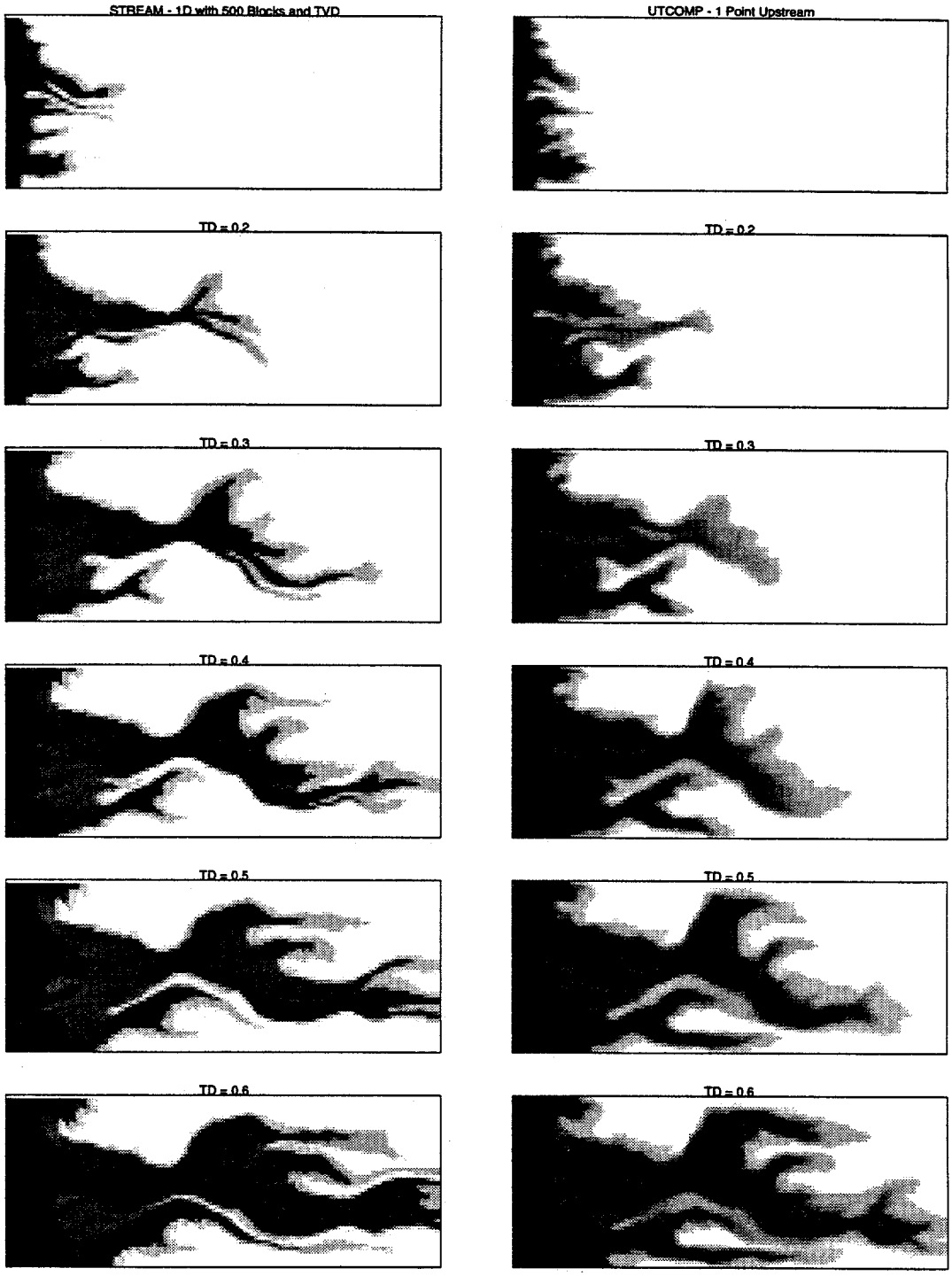

Figure 2.21: Comparison of the evolution in time of the gas saturation. The streamtube solution was found using a 500 grid block one-dimensional solution, while the UTCOMP solution was found using a third-order TVD scheme.

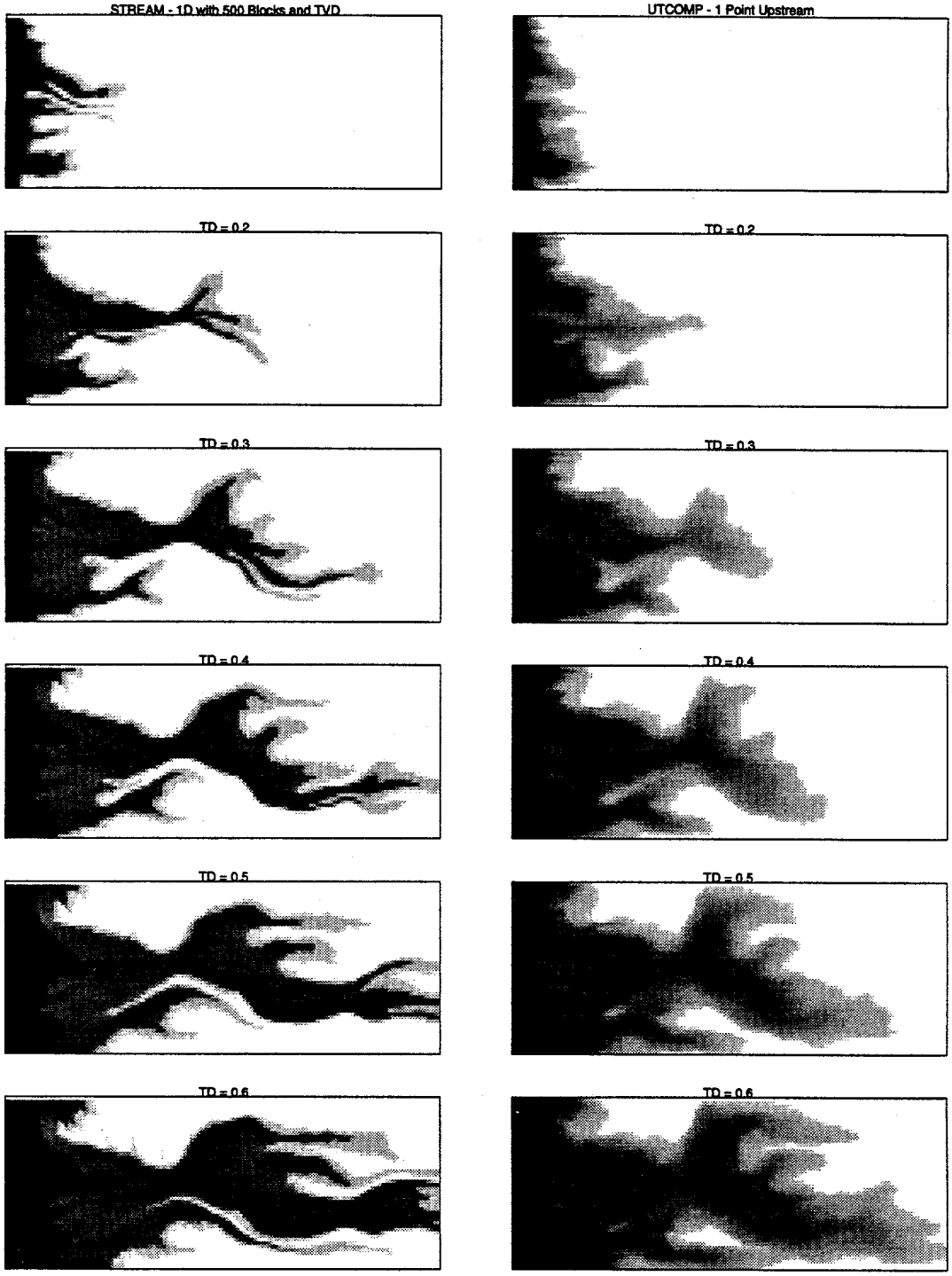

Figure 2.22: Comparison of the evolution in time of the gas saturation. The streamtube solution was found using a 500 grid block one-dimensional solution, while the UTCOMP solution was found using a single-point upstream weighting scheme.

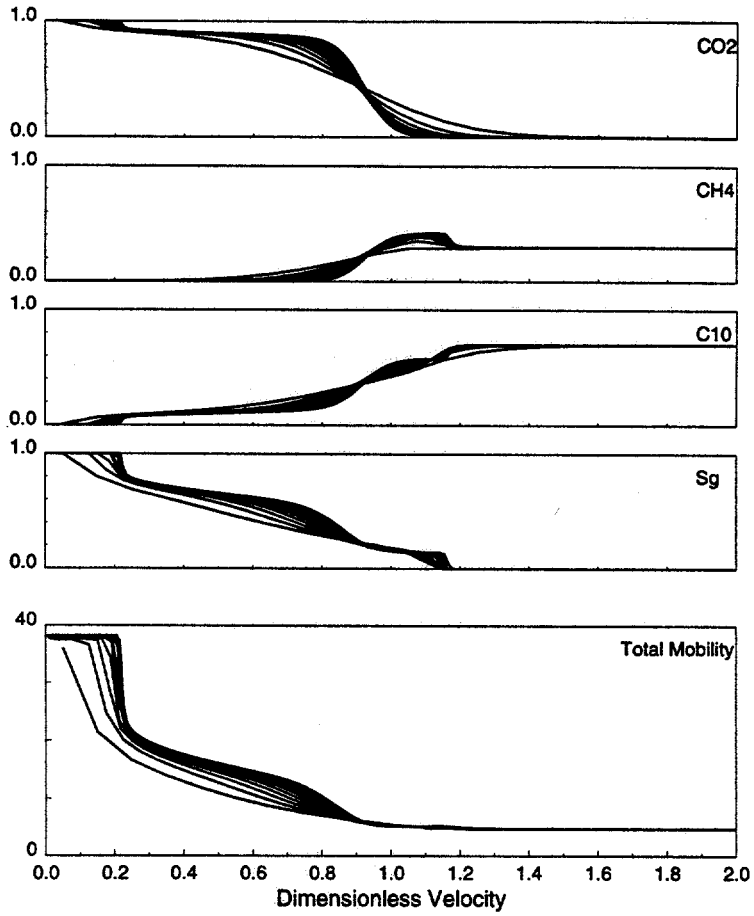

Figure 2.23: One-dimensional UTCOMP solution using 100 grid blocks and one point upstream weighting. Each solution represent an increment of $\Delta t_D = 0.1$.

(2) - Diffused Streamtube Solution

The UTCOMP solutions with TVD and single-point upstream weighting strongly suggest that the frontal instability is mitigated substantially by numerical diffusion. Thus, it should be possible to find a 'diffused' one-dimensional solution along the streamtubes that would lead to a solution similar to the one obtained using finite differences. The one-dimensional solution used in the streamtube solution so far was obtained using 500 grid blocks and a third-order TVD scheme, which produced a solution with relatively sharp fronts. But given the fact that only 125 blocks are present in the main direction of flow and that a TVD scheme in two-dimensions does not necessarily have the same numerical diffusion control as it does in one dimension[9], a one-dimensional solution using only 100 grid blocks and single point upstream weighting was mapped along the streamtubes. A difficulty associated with mapping a 'diffused' one-dimensional solution is that the solution is no longer scalable by x_D/t_D, as is shown in Fig. 2.23. There are 10 curves in Fig. 2.23, each representing a solution at time increments of $\Delta t_D = 0.1$ starting from $t_D = 0.1$. The solution clearly tends to 'sharpen-up' with time, although even at $t_D = 1.0$, the solution is still suffering from numerical diffusion. To capture the time dependence of the diffused, one-dimensional solution in Fig. 2.23, the solution was mapped along the streamtube for the corresponding time interval. Thus, the first curve was used in the streamtube simulator to find solutions in the range of $t_D = 0.0$ and $t_D = 0.1$,

[9]In general, any method that is TVD in two dimensions will be at most first-order accurate, although the accuracy can be increased to second-order if Strang splitting is used [82].

the second curve for solutions between $t_D = 0.1$ and $t_D = 0.2$, etc. Although this approach is only a rough attempt to include longitudinal 'numerical'-type diffusion into the streamtube solution, it does mitigate the mobility contrast.

Fig. 2.24 shows a comparison of the UTCOMP saturation maps to the saturation maps obtained from the streamtubes using the more diffused 100 grid block one-dimensional solutions with single-point upstream weighting. The streamtube displacement is indeed more stable (compare with Fig. 2.21), and it is apparent from this comparison that by adding 'numerical diffusion' to the streamtube solution, the finite difference solution can be approximated. It is important to mention at this point that the diffused one-dimensional solution mapped along the streamtubes can, at best, approximate only longitudinal numerical diffusion. Clearly, the UTCOMP solution will also have transverse diffusion, which cannot approximated by the one-dimensional solution. The remaining difference between the streamtube solution and the UTCOMP solution then, could be attributed to transverse diffusion. A supporting argument to this effect is that the streamtube solution still sees a higher mobility and corresponding higher frontal velocities. Transverse numerical diffusion would effectively slow the leading shock velocities. Finally, it is important to remember that for compositional displacements numerical diffusion interacts with phase behavior to alter composition paths in a way that changes phase saturations and therefore phase mobilities.

Fig. 2.25 shows a summary of the gas saturation maps for the various cases discussed previously. Two key issues are summarized in Fig. 2.25: (1) numerical diffusion, both longitudinal and transverse, and resulting phase behavior effects substantially mitigate the original instability of the displacement and (2) the streamtube solution with the sharp, 500 grid block solution may in fact be considered as the limiting no-diffusion solution to the three component problem. The large difference in computation times, 3000-10000 Cray seconds per 0.1 PV injected depending on numerical scheme and grid size for UTCOMP versus the 2-3 Cray seconds for the streamtube solution, clearly makes the streamtube solution very attractive, despite the underlying Riemann assumption used in mapping the one-dimensional solutions along the streamtubes. Fig. 2.25 is interesting in that it shows how numerical diffusion is able to mitigate the instability of the displacement, and it is likely that both UTCOMP solutions in Fig. 2.25 are not converged solutions. Increasing refinement and time-step reduction would probably reveal extensive viscous fingering.

Fig. 2.26 shows the same three component, two-phase displacement through a less heterogeneous system ($\lambda = 1.00$, $\sigma_{\ln k} = 0.5$,$HI = 0.25$). The interesting feature of Fig. 2.26 is that while the single-point upstream solution shows no viscous fingering whatsoever, the same solution using a third-order TVD scheme is able to retain sufficient mobility contrast to show some fingering in the channel. The streamtube solution, of course, is not able to reproduce any viscous fingering, but it captures the main flow path and the primary features of the displacement at a much lower computational cost.

2.7 Concluding Remarks

The underlying assumption in applying the streamtube method to describe multiphase, multicomponent flow in heterogeneous porous media is that field scale displacements are dominated by reservoir heterogeneity and convective forces. Flow paths are captured by streamtubes, the geometry of which reflects the distribution of high and low flow regions in the reservoir. Each streamtube is treated as a one-dimensional system along which solutions to mass conservation equations for different displacement mechanisms can be mapped. The streamtube approach effectively decouples the 'channeling' imposed by the reservoir heterogeneity from the actual displacement mechanism taking place. In other words, regardless of the displacement type, the assumption is that there are predefined flow paths that will dominate the two-dimensional solution. The fluid velocity along these flow paths is reflected by the geometry of the streamtubes, and the inherent nonlinearity in

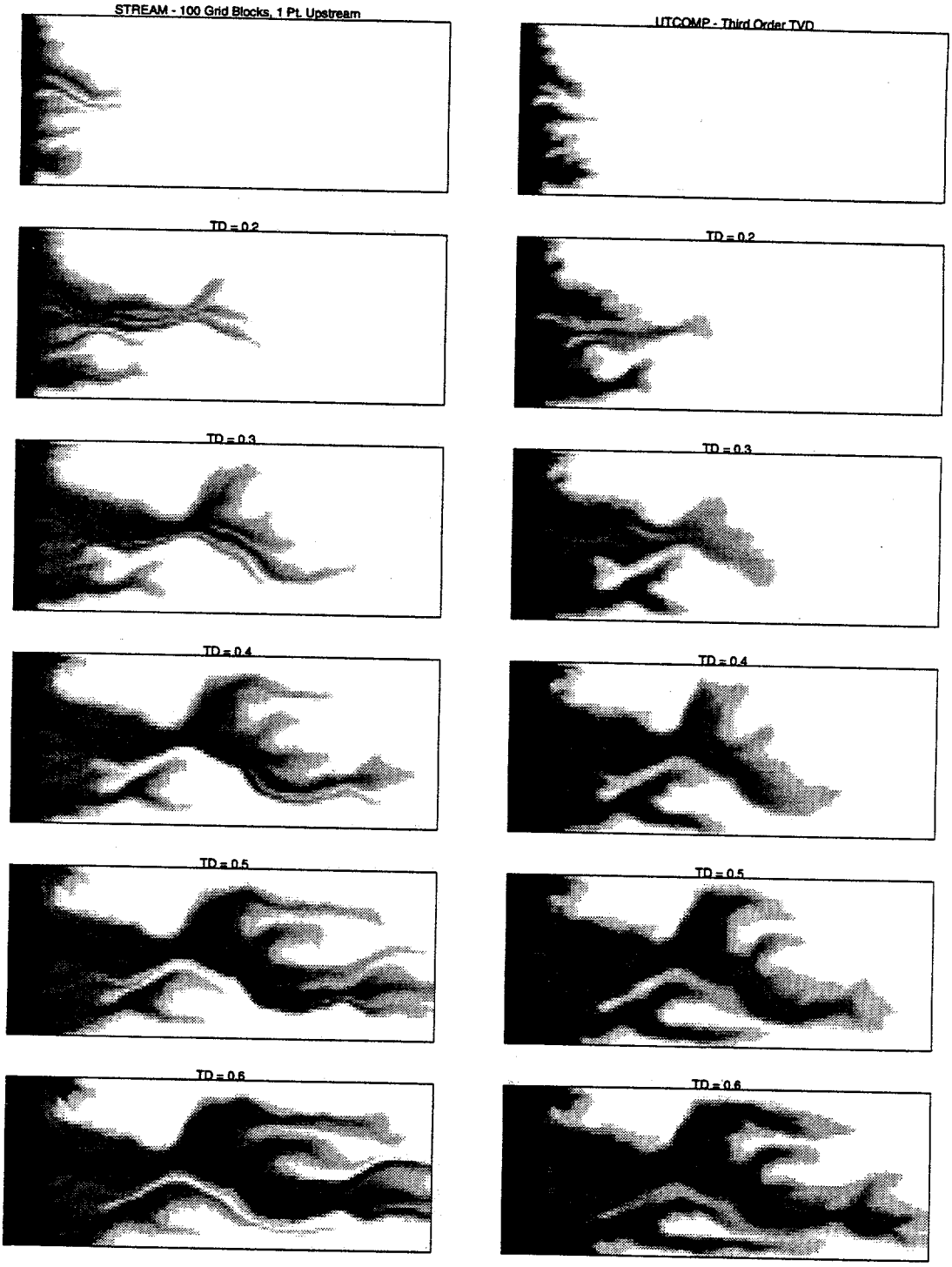

Figure 2.24: Comparison of the evolution in time of the gas saturation. The streamtube solution was found using a single point upstream, 100 grid block 1D solution while the UTCOMP solution was found using a third-order TVD scheme on a 125x50 grid.

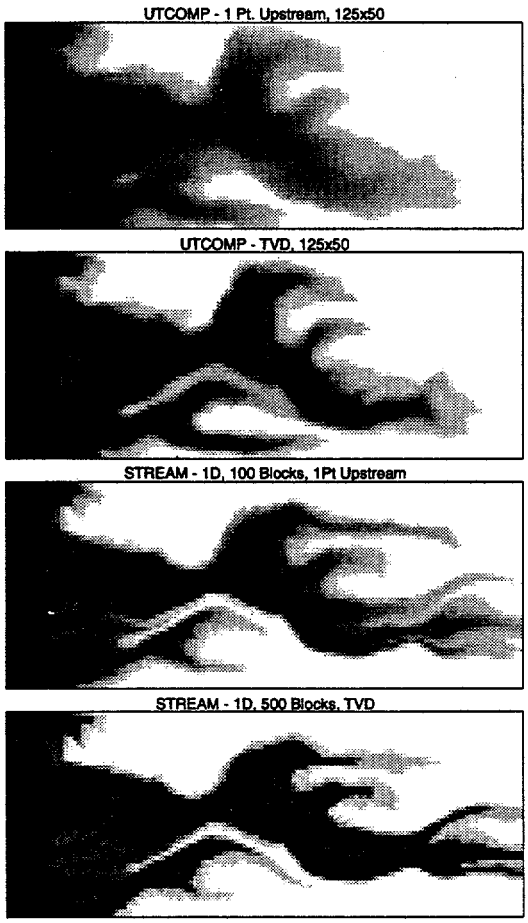

Figure 2.25: Summary of gas saturation maps at $t_D = 0.5$. From top to bottom: UTCOMP solutions with single-point upstream weighting, UTCOMP solutions third order TVD schme, streamtube solution using a 1D, 100 blocks, single-point upstream solution, and streamtube solution using a 1D, 500 grid block-TVD solution.

the underlying velocity field is captured by periodically updating the streamtubes.

One-dimensional solutions are mapped along the streamtubes using a 'Riemann approach' — each streamtube is treated as true one-dimensional system with constant initial and injected conditions, allowing to time-step by integrating from $t_D = 0$ to $t_D = t_D + \Delta t_D$. This approach allows analytical and numerical solutions to hyperbolic conservation equations (found using Riemann boundary conditions) to be mapped along periodically updated streamtubes. The reason for using the Riemann approach is to avoid difficulties associated with general-type initial conditions along streamtubes, in which case solutions could be found only numerically for each time step, either using a finite-difference approach or a front-tracking type approach. General-type initial conditions along streamtubes arise by updating the streamtubes while keeping the spatial saturation/concentration/composition distribution fixed. Initializing each new streamtube using the old saturation/concentration/composition distribution clearly produces initial conditions that are problem specific and of general-type.

Solutions for (1) tracer flow, (2) two-phase immiscible flow, (3) first contact miscible flow, and (4) two-phase, multicomponent flow are presented. For tracer flow the streamtubes are fixed in time and the Riemann approach is equivalent to time stepping from t_D to $t_D + \Delta t_D$. The only assumption in finding two-dimensional solutions involves neglecting transverse diffusion/dispersion mechanisms, and in the limit of a piston-like front a diffusion-free two-dimensional solution is

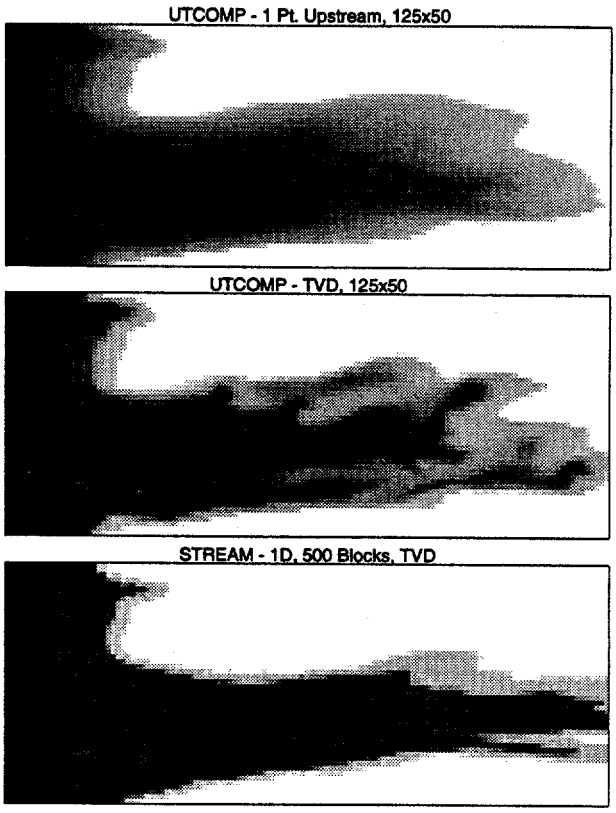

Figure 2.26: $CH_4/CO_2/C_{10}$ displacement in a mildly heterogeneous system showing the suppression of viscous fingers due to numerical diffusion.

found that can be used to quantify the error introduced by numerical diffusion in traditional simulation methods. Longitudinal physical diffusion can be added explicitly by mapping a CD-solution for a given Peclet number along streamtubes. Using the CD-solution is also an example of representing two different scales of reservoir heterogeneity: the large-scale heterogeneity captured by the geometry of the streamtubes and a smaller scale heterogeneity within each streamtube quantified indirectly by the Peclet number.

In the two-phase immiscible case the velocity field becomes a function of saturation and the streamtubes are updated periodically as the flood progresses. The Riemann approach is used to map the Buckley-Leverett solution along streamtubes, where the error due to the Riemann approach is argued to be less than the error introduced by numerical diffusion in a traditional finite difference solution. The key result though, is the convergence of the streamtube approach in orders of magnitude less matrix inversions (velocity field updates) than traditional solutions. By capturing the overall heterogeneity structure only a few streamtube updates (less than 20 over 2 pore volumes injected) are necessary to predict overall recovery correctly.

Applying the streamtube approach to first-contact miscible flow raises the challenging question of the 'correct' one-dimensional solution to be used. Scaling arguments are used to suggest that streamtubes that gave rise to a Fickian limit for $M = 1$ displacements (tracer flow) should now see a viscous fingering flow regime for unstable $M > 1$ first contact displacements. Thus, a Todd–Longstaff model is used to capture the sub-streamtube viscous fingering regime. The streamtube method is again able to predict recoveries using orders (2-3) of magnitude less computation time than traditional simulation approaches. 180 recoveries are found to show how nonlinearity and reservoir heterogeneity interact to define the uncertainty in overall recovery, and the usefulness of the streamtube approach as a fast filter is pointed out. Only permeability fields returning maximum and minimum overall recoveries in the streamtube approach need to be used to confirm

the spread in recovery using an expensive finite difference/finite element simulation.

For compositional displacements the streamtube approach is shown to be particularly powerful due to its simplicity, robustness, and speed. The speed-up compared to traditional finite difference approaches can range from 3 to 5 order of magnitude. The streamtube method is used to asses how good traditional numerical solutions to compositional displacements really are, particularly in view of numerical diffusion interacting with phase behavior calculations. The key result is the demonstration that numerical diffusion can substantially reduce the mobility contrast in traditional finite difference solutions.

2.8 Conclusions

Fast, accurate, and robust solutions. The streamtube approach produces fast, accurate, and robust solutions to displacements that are dominated by reservoir heterogeneity. Streamtube geometries capture the impact of heterogeneity on the flow field, while the one-dimensional solutions mapped along them retain the essential physics of the displacement mechanism. Speed-up is by two to three orders of magnitude for two-phase immiscible and first contact miscible displacements and four to five orders in two-phase compositional displacements. The absence of any convergence criteria as well as capturing all the essential physics of the displacement (like phase behavior) in the already present one-dimensional solution leads to particularly robust solutions.

Statistical reservoir forecasting. The speed of the streamtube approach makes it an ideal tool for statistical reservoir forecasting: hundreds of geostatistical images can be processed in a fraction of the time required by traditional reservoir simulators. Application to first contact miscible displacement show a substantial uncertainty in overall recovery due to the combined effects of reservoir heterogeneity and the inherent nonlinearity of the displacements. As reservoir heterogeneity and nonlinearity increase so does the uncertainty in overall recovery. The streamtube approach allows to quantify this uncertainty, which can then be confirmed by a more expensive traditional approach by using only the two geostatistical images that produces maximum and minimum recoveries. Although the streamtube method makes strong assumptions in generating the two-dimensional solutions, the uncertainty in recovery due to heterogeneity is shown to be substantially larger than the error introduced by the Riemann approach.

Weak nonlinearity of Ψ. For all displacements, the necessary updates of the streamtubes to converge onto a solution are shown to be many orders of magnitude less than the equivalent number of pressure solves in traditional numerical simulation approaches. As a result, updating the streamtubes only periodically (20-40 times per 2 pore volumes injected) and using a one-dimensional solutions that captures the essential physics of the displacement is sufficient to give accurate overall recoveries.

Decoupling of phase behavior from 2D grid. The streamtube approach becomes particularly powerful for multiphase compositional displacement. All the phase behavior is now contained in the one-dimensional solution that is mapped along the streamtubes, completely decoupling the underlying cartesian grid used to specify reservoir heterogeneity from phase behavior considerations. This is different from traditional approaches to reservoir simulation, which perform a flash calculation for each grid block at each time step. As a result, the streamtube approach makes for very robust solutions in the case of compositional displacements.

Impact of numerical diffusion on compositional displacements. Numerical diffusion is argued to have a significant role in reducing the mobility contrast in traditional finite difference

solutions of compositional displacements. By comparing streamtube solutions to finite difference solutions it is shown that the original mobility contrast is substantially reduced by the presence of numerical diffusion. Reservoir heterogeneity, phase behavior, and numerical diffusion may be so dominant in compositional displacements as to force only slow convergence due to progressive grid refinement. Two to four times the refinement used in FCM displacement may be necessary in compositional displacements, particularly if a single-point upstream weighting scheme is being used, to see the equivalent improvement in the solution. As a result, compositional displacements on coarse grids obtained using a single-point upstream weighting scheme are not likely to result in converged solutions.

3. Interaction of Phase Behavior and Flow in Porous Media

In this chapter, we describe our continuing effort to analyze the interaction of phase behavior with multiphase flow in porous media. In Section 3.1, we present a new approach for fast calculations of critical tie lines directly from the criticality conditions. This technique is then applied to the determination of the minimum miscibility pressure (MMP), at which one of the key tie lines to the displacement becomes critical. In Section 3.2, we show that a "global triangular structure" arises for four-component flow systems whose tie lines meet at the edge of a quaternary phase diagram, or lie in planes. We also demonstrate that the solutions can be easily extended to multicomponent systems under the same assumptions. The analysis reported here represents significant progress toward the goal of an unambiguous definition of MMP for multicomponent displacements.

3.1 MMP Calculation from Critical Tie Lines

Bruno Aleonard

It has been shown that calculating minimum miscibility pressures from flash calculations has limitations due to inherent convergence problems of flash routines near critical points [4]. In particular, it can be difficult to obtain converged solutions for tie lines in the neighborhood of these points. Yet, a precise knowledge of these tie lines is essential in describing the development of multicontact miscibility. In this subsection, we demonstrate a different approach to the problem by determining directly critical tie lines. In order to determine critical tie lines, we need to define the criteria for determination of critical point. We make use of the method of Heidemann and Khalil [51], which we review in the section that follows.

3.1.1 The Method of Heidemann and Khalil

The objective in Heidemann and Khalil's paper [51] is to determine the critical temperature and pressure of a system of fixed composition. As expressed by Gibbs [47], a mixture is stable in a single phase state if for every transition from a system $S_0\ (T_0, V_0, n_{10}, \cdots, n_{N0})$ to a neighboring system $S\ (T, V, n_1, \cdots, n_N)$:

$$\left[A - A_0 + P_0(V - V_0) - \sum_{i=1}^{N} \mu_{i0}(n_i - n_{i0})\right]_{T_0} > 0, \tag{3.1}$$

for an isothermal variation and:

$$[A - A_0 + S_0(T - T_0)]_{V_0, n_{j0}} > 0. \tag{3.2}$$

This last condition is satisfied if the heat capacity at constant volume is positive which will be assumed for our systems. Similar conditions could be written with the Gibbs, instead of Helmholtz, free energy function. It is preferable though to use temperature and volume as independent variables, along with mole fractions, for pressure-explicit equations of state such as the Peng-Robinson equation. Helmholtz' free energy is then the most convenient thermodynamic function to consider. Eq. 3.1 is automatically satisfied for pure dilations of S_0. Increasing volume and the number of moles of each component correspondingly by multiplying them by the same constant does not affect

the nature of the system but merely its size. This would not constitute a new fluid state and will not provide new critical points. We can therefore impose on Eq. 3.1 the following condition,

$$\Delta V = 0, \tag{3.3}$$

with which Eq. 3.1 simplifies to

$$\left[A - A_0 - \sum_{i=1}^{N} \mu_{i0} \Delta n_i\right]_{T_0,V_0} > 0. \tag{3.4}$$

Now, the chemical potential may be defined as

$$\mu_{i0} = \left(\frac{\partial A}{\partial n_i}\right)_{V_0,T_0,n_{j\neq i}}. \tag{3.5}$$

The Helmholtz free energy can then be expanded in a Taylor series

$$\begin{aligned}\left[A - A_0 - \sum_{i=1}^{N} \mu_{i0} \Delta n_i\right]_{T_0,V_0} &= \frac{1}{2!} \sum_i \sum_j \left(\frac{\partial^2 A}{\partial n_i \partial n_j}\right) \Delta n_i \Delta n_j \\ &+ \frac{1}{3!} \sum_i \sum_j \sum_k \left(\frac{\partial^3 A}{\partial n_i \partial n_j \partial n_k}\right) \Delta n_i \Delta n_j \Delta n_k \\ &+ o(\Delta n^4). \end{aligned} \tag{3.6}$$

The single phase stability criterion, Eq. 3.4, requires that this quantity be positive for all Δn. In other terms, the quadratic form defined by the matrix

$$Q = (q_{ij})_{\substack{1 \leq i \leq N \\ 1 \leq j \leq N}} = \left(\frac{\partial^2 A}{\partial n_j \partial n_i}\right)_{T_0,V_0}, \tag{3.7}$$

must be positive definite. But at the *limit of stability*, where critical points lie, the second-order term disappears and the quadratic form must be rank deficient. The form thus is merely positive semi-definite, and we must have

$$\det(Q) = 0. \tag{3.8}$$

Therefore, there must exist a nonzero vector Δn such that

$$Q \Delta n = 0. \tag{3.9}$$

Except for a few pathological cases, the rank of Q will be N-1 at critical points, so that the set of Δn vectors solutions to Eq. 3.8 is of dimension 1.

Critical points should also fulfill a *stability condition*. For the positivity criterion to be satisfied, the dominant term in Eq. 3.6 must be of even order. Therefore, the second criticality condition can be written as:

$$C = \sum_i \sum_j \sum_k \left(\frac{\partial^3 A}{\partial n_i \partial n_j \partial n_k}\right) \Delta n_i \Delta n_j \Delta n_k = 0, \tag{3.10}$$

for the vectors Δn that satisfy Eq. 3.9.

The calculation of the partial derivatives of the Helmholtz free energy is dependent on the equation of state chosen. Originally, Heidemann and Khalil preferred the Soave-Redlich-Kwong equation. In this report, we opt for the Peng-Robinson equation of state, which is widely used for

representation of multicontact miscible gas/oil systems. In any case, since both equations are cubic and pressure-explicit, the method remains very much the same.

The terms of the quadratic form Q and the cubic form C can be derived from the following relations

$$\left(\frac{\partial^2 A}{\partial n_i \partial n_j}\right) = RT\left(\frac{\partial \ln f_j}{\partial n_i}\right), \tag{3.11}$$

and

$$\left(\frac{\partial^3 A}{\partial n_i \partial n_j \partial n_k}\right) = RT\left(\frac{\partial^2 \ln f_k}{\partial n_i \partial n_j}\right), \tag{3.12}$$

where fugacities are known functions for the Peng-Robinson and SRK equations.

In their paper, Heidemann and Khalil considered a mixture of known composition. Starting from an initial guess in volume, Eq. 3.8 determines an equation for temperature, which can be solved numerically by iterative methods. Once a temperature has been found, the null space of the quadratic form Q can readily be obtained: a set of non-zero vectors which verify Eq. 3.9 is thus computed. Leaving out those pathological cases where Q would degenerate to a rank less than N-1, by further imposing the condition $\Delta n_N = 1$ on the last component, a unique solution is obtained. Eq. 3.10 is then checked and another guess on volume is made if the condition is not satisfied. Two one-dimensional searches, one outer loop on volume and one inner loop on temperature were thus applied. It was then easy, having reached convergence, to calculate the critical pressure from pressure-explicit equations of state.

3.1.2 Critical Tie Lines

A stable system represents a minimum of the Helmholtz free energy A. If there exists another state for which A can take a lower value, the system will evolve to that new state. For example, a one-phase system may switch to two-phases. The schematic in Fig. 3.1 shows what happens when a two-phase mixture approaches a critical point.

The one-phase Helmholtz energy is plotted against a single variable for simplicity's sake, here a mole fraction. It can be shown that a two-phase state has to lie on a straight line, since A is then a linear combination of the chemical potentials of the two pure species, and that the straight line has to be tangent at both ends at (x_1 and x_2) mole fractions to the original one-phase curve. In the interval where the two-phase value of A is less than it would be in single-phase state, the two-phase solution is more stable. Also, the straight line on the diagram is exactly a tie line, joining the liquid and vapor compositions x_1 and x_2.

Let us now examine what happens at a critical point. The mole fractions x_1 and x_2 coalesce, and the straight line is in fact *twice* tangent to the single-phase curve. In more mathematical terms, $A'(x_1)$ being kept equal to $A'(x_2)$ as the critical point is approached:

$$\begin{aligned} A''(x_1) &= \lim_{\substack{x_2 \to x_1 \\ A'(x_1)=A'(x_2)}} \frac{A'(x_1) - A'(x_2)}{x_2 - x_1} \\ &= 0. \end{aligned} \tag{3.13}$$

As x_2 approaches x_1, the tie line (x_1, x_2) tends towards a critical tie line and its approximation to the single-phase curve will be at least of order 3, as seen from Eq. 3.13. Moreover, since a local behavior of odd order around the critical point would violate the positivity criterion (Eq. 3.4), the approximation of A by its tangent must be of order 4 at least.

A similar argument can be given for multicomponent systems and applied to the determination of critical tie lines. Δn, as found from Eqs. 3.9 and 3.10, is a direction in composition space along which the Helmholtz free energy A at a critical point is closest to the tangent hyperplane:

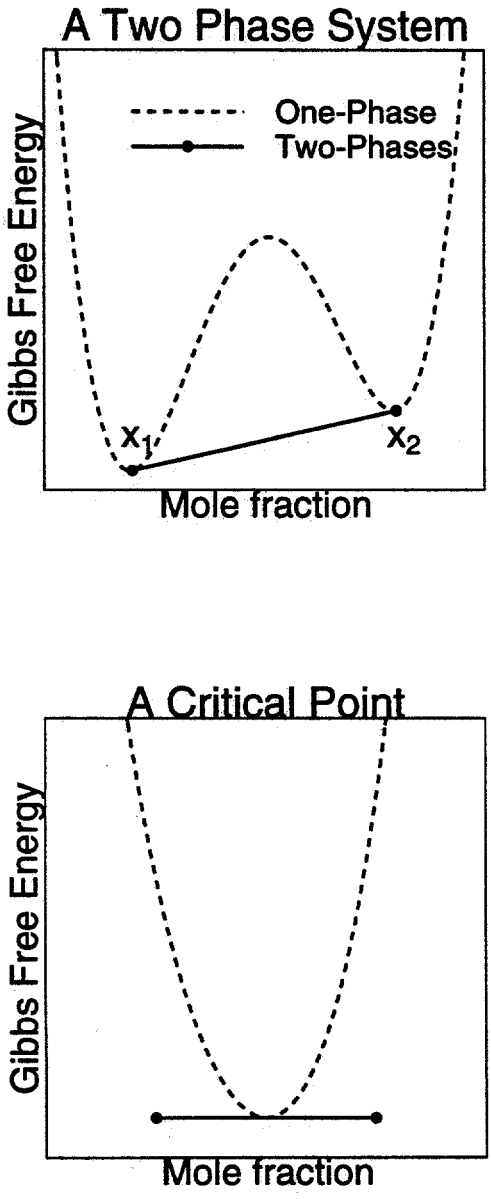

Figure 3.1: Helmholtz free energy plots with phase splitting and critical behavior.

the approximation is at least of order 4. If, as is most often the case, the quadratic form Q is of rank $N-1$, such a direction is unique, and it defines therefore the critical tie line, by the same argument as above. Having already obtained Δn, it was thus straightforward to determine the critical tie line around a critical point.

A verification of the approach was performed for a ternary system. Additional details of the technique and tests of its performance are given by Aleonard [4]. In particular a system containing methane (C_1), and pseudo-components C_{2+} and C_5+. Properties of the components are also given by Aleonard. Fig. 3.2 shows the ternary phase diagram of the system at 3650 psia and 200°F.

The binodal curve is calculated with CMGPROP. The method for calculating the critical point set out by Aleonard [4] was only slightly adapted for ternary mixtures by eliminating the guess on z_0. Once again, the critical point is shown to coincide graphically with its position obtained from the flash calculations of CMGPROP. The critical tie line is also tangent to the binodal curve, as it should be, which illustrates well the accuracy of the method.

3.1.3 Determination of the MMP: a New Method for Four-Component Systems

If critical tie lines at different critical points can be calculated , then it is possible to determine at which pressure one of the key tie lines that control displacement behavior (injection, initial or crossover) becomes critical. For purely condensing or vaporizing gas drives with four components, where miscibility is controlled by either the injection or initial tie lines, the following procedure can be applied:

1. Make a guess on pressure.
2. Initiate a loop on the location of the critical point. This would be a one-dimensional search along the critical curve for a four-component system (z_0 in the cases studied here).
3. At the chosen pressure and critical point, determine the critical tie line.
4. Depending on whether the process is controlled by the injection or initial tie line, compute the distance from the reservoir oil or injection gas composition to the critical tie line determined above.
5. Minimize that distance on the location of the critical point by closing the inner loop and going back to 2.
6. If the distance is not small enough, return to step 1.

Obviously, the distance will tend to decrease first with pressure, reach zero at the MMP and then increase as the critical locus recedes behind the controlling tie line. Moreover, the same method can be applied to ternary systems.

For condensing/vaporizing gas drives, in which miscibility is controlled by the crossover tie line, the method is slightly modified. In this example, we consider self-sharpening systems, in which the crossover tie line must intersects both the initial and injection tie lines [66]. For such a four-component displacement, at any given pressure, the set of critical tie lines form a ruled surface that will be intersected, except in a few cases, by the injection tie line. The intersection corresponds to a particular critical tie line whose distance to the initial tie line can then be calculated. Because the crossover tie line must meet both the injection and initial tie lines, that distance should be zero for the pressure (MMP) at which the critical tie line determined becomes the crossover tie line. Thus, the following steps were taken:

1. Same as above.

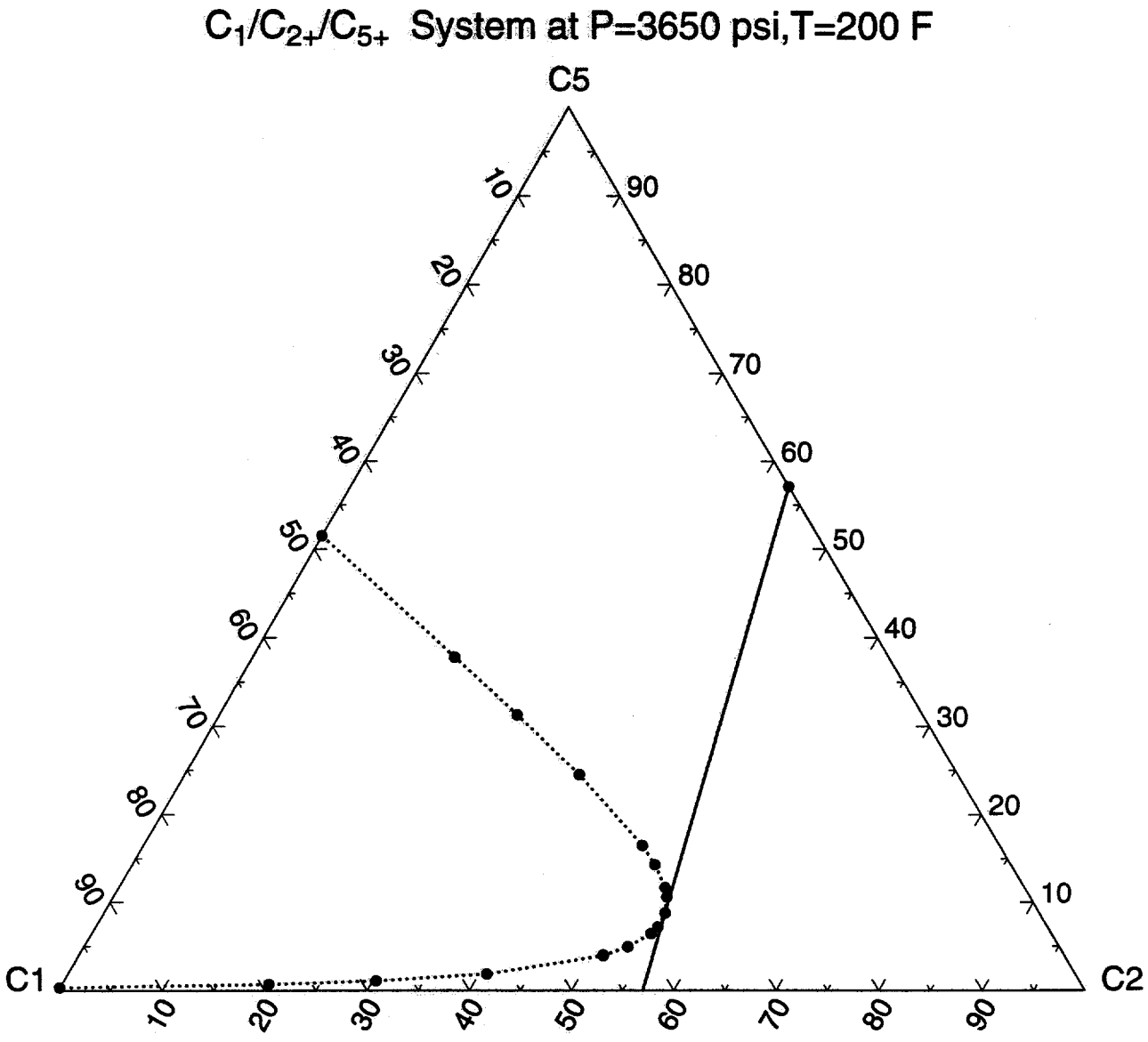

Figure 3.2: Critical tie line for a ternary system.

Table 3.1: Component Properties of Four-Component Model (System 1).

Component	M_w	P_c (psia)	T_c (°F)	ω
CH_4N_2	16.0	671.17	-117.07	0.0130
C_{2+}	41.0	769.81	142.79	0.1592
C_{5+}	189.0	322.89	775.00	0.6736
C_{30+}	451.0	171.07	1136.59	1.0259

Component	Interaction Parameters			
	CH_4N_2	C_{2+}	C_{5+}	C_{30+}
CH_4N_2	0.0000	0.0286	0.0258	0.2000
C_{2+}	0.0286	0.0000	0.0607	0.1268
C_{5+}	0.0258	0.0607	0.0000	0.0000
C_{30+}	0.2000	0.1268	0.0000	0.0000

2. Same as above.
3. At the chosen pressure and critical point, determine the critical tie line.
4. Compute the distance between the critical tie line and the injection tie line.
5. Minimize that distance on the location of the critical point by closing the inner loop and returning to step 2. In most cases, the minimum distance should be zero since the injection tie line is very likely to meet the ruled surface of critical lines.
6. Iterate on pressure if the distance between the critical line found and the initial tie line is too large.
7. A critical tie line that intersects both the initial and the injection lines is thus found. It is then the crossover tie line, and the prevailing pressure is the MMP.

3.1.4 Determination of the MMP: Example 1

The proposed algorithm was tested for a four-component system studied by Johns et al. [66]. In that study, the enrichment required for development of miscibility was determined (approximately) by obtaining a sequence of solutions in which the crossover tie lines approached the critical locus. That procedure was time consuming because flash calculations for tie-lies near a critical point often converged slowly (or not at all). The critical properties of the components are given in Table 3.1. That displacement is controlled by the crossover tie line, which is an unique tie line that intersects the initial and injection tie lines. Fig. 3.3 represents the distance computed in step 6 in the last algorithm, between the critical tie line that intersects the injection tie line, and the initial tie line. The unit of length is the side of the tetrahedron in the phase diagram.

As could be anticipated, the distance first decreases with pressure until it reaches a minimum close to zero at the minimum miscibility pressure and then increases. It is also remarkable that the behavior is almost linear, with large slopes so that evaluation of the MMP is easy. Also, at fixed pressure, computations were much faster than for the flash method.

The MMP thus estimated is close to the value found by extrapolation of the flash calculation [4] at 4025 psia. The phase diagram is drawn at 4025 psia and 200°F in Fig. 3.4. The critical tie

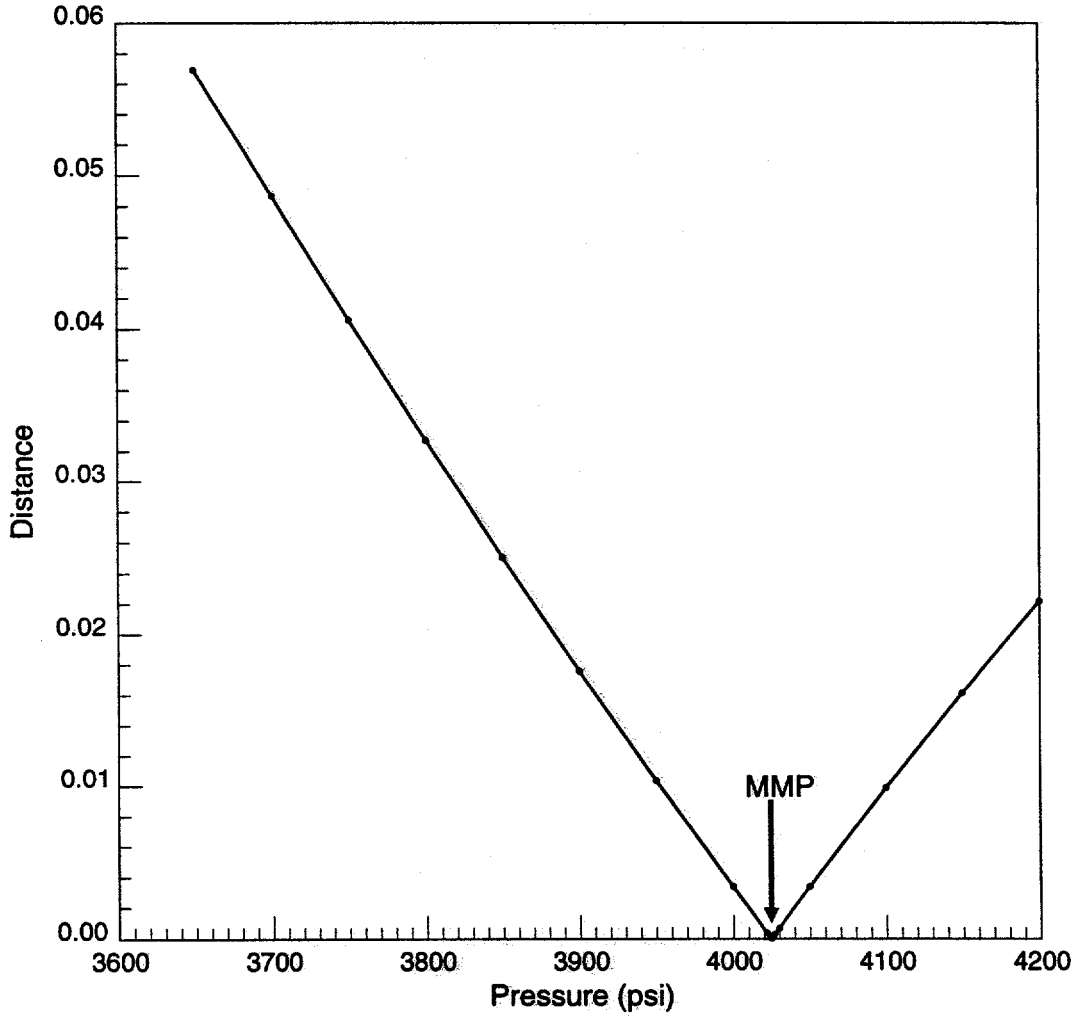

Figure 3.3: Distance between the initial tie line and the critical tie line that intersects the injection tie line.

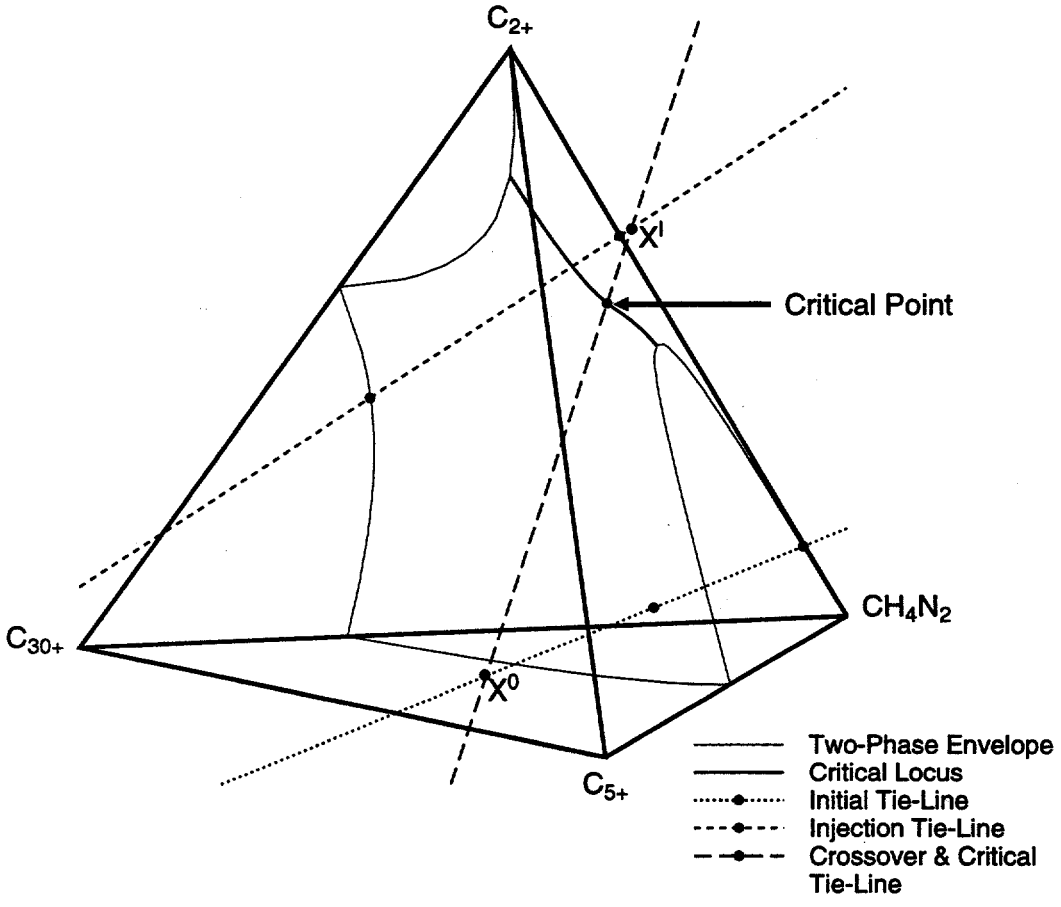

Figure 3.4: Phase diagram at 4025 psia (MMP) and 200°F (system 1).

Table 3.2: Component Properties of Four-Component System

Component	M_w	P_c (psia)	T_c (°F)	ω
CH_4	16.04	667.8	-116.63	0.0104
C_2	30.07	707.8	90.09	0.0990
C_6	86.18	430.6	453.63	0.2990
C_{16}	226.448	205.7	830.91	0.7420

Component	Interaction Parameters			
	CH_4	C_2	C_6	C_{16}
CH_4	0.0000	0.0000	0.0250	0.0350
C_2	0.0000	0.0000	0.0100	0.0100
C_6	0.0250	0.0100	0.0000	0.0000
C_{16}	0.0350	0.0100	0.0000	0.0000

Component	Compositions			
	CH_4	C_2	C_6	C_{16}
Injection	0.3500	0.6500	0.0000	0.0000
Initial	0.2000	0.0000	0.4000	0.4000

line that intersects both the injection and initial tie lines is shown.

3.1.5 Determination of the MMP: Example 2

Johns [66] gives another example of a four-component system ($C_1/C_{2+}/C_{5+}/C_{30+}$) with injection and reservoir compositions, whose miscibility is controlled by the crossover tie line. Table 3.2 summarizes the compositions and the critical properties of the system. In this system again, the solution pathway shocks from and to the crossover tie line, which means again that the latter intersects both the injection and initial tie lines.

A plot similar to Fig. 3.4 enabled accurate determination of the MMP (see Fig. 3.5), here 2244 psia at 200°F. The phase diagram is also given at the MMP in Fig. 3.6. The intersection of the crossover tie line with the initial tie line is not shown because the tie line extensions are too long. Here again, the proposed method allows direct determination of the MMP with the calculations that do not suffer from the slow convergence often observed in flash calculations near a critical point.

3.1.6 Summary

A rigorous method to determine critical tie lines was given, based on the analysis of criticality conditions already presented. Essentially, the vector Δn as defined by Heidemann and Khalil gives the direction of critical tie lines. This knowledge, independent of any flash computations, allows an accurate determination of minimum miscibility pressures for at least ternary and quaternary systems.

The method provided here is simple, yields results similar to the flash method, but is much faster and more accurate. Problems of multiple solutions were not encountered. The method was

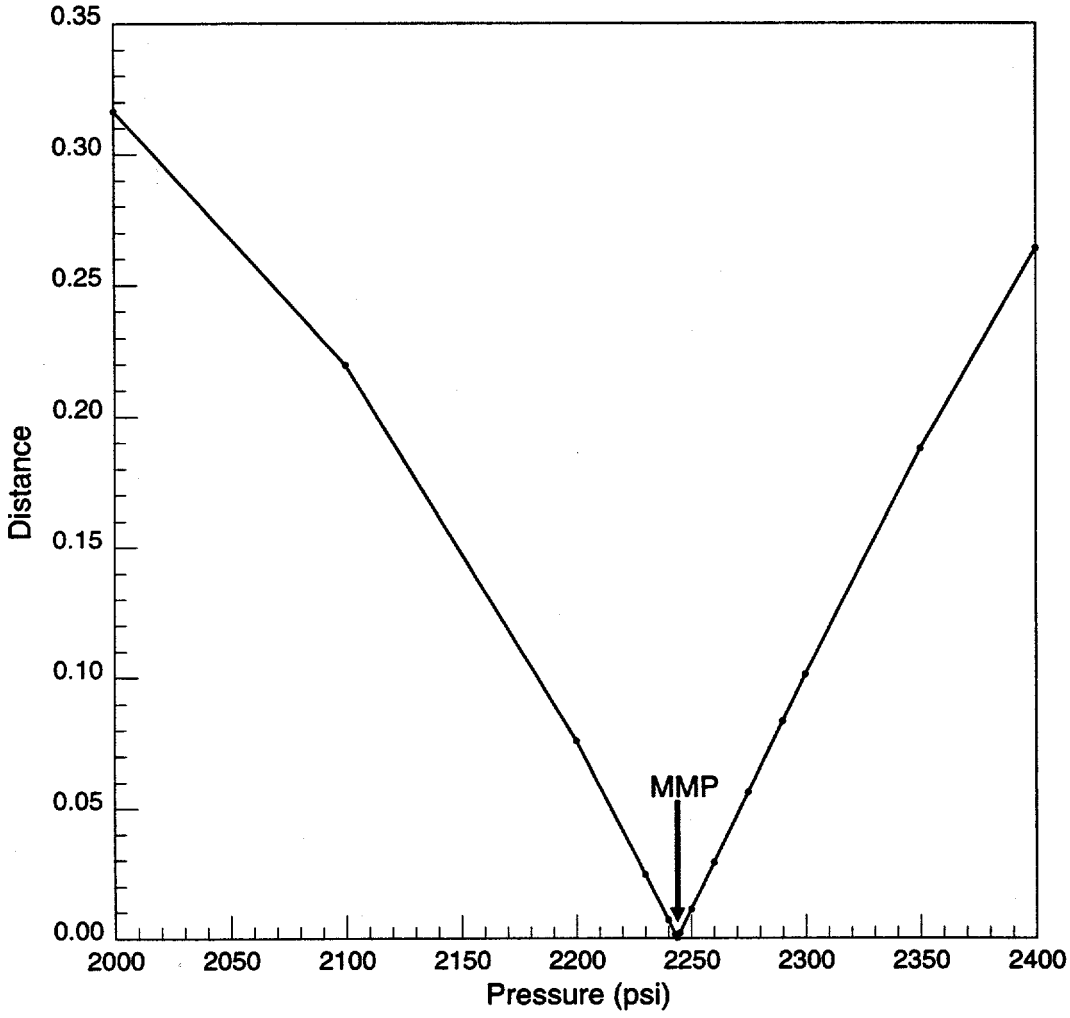

Figure 3.5: Distance between the initial tie line and the critical tie line that intersects the injection tie line.

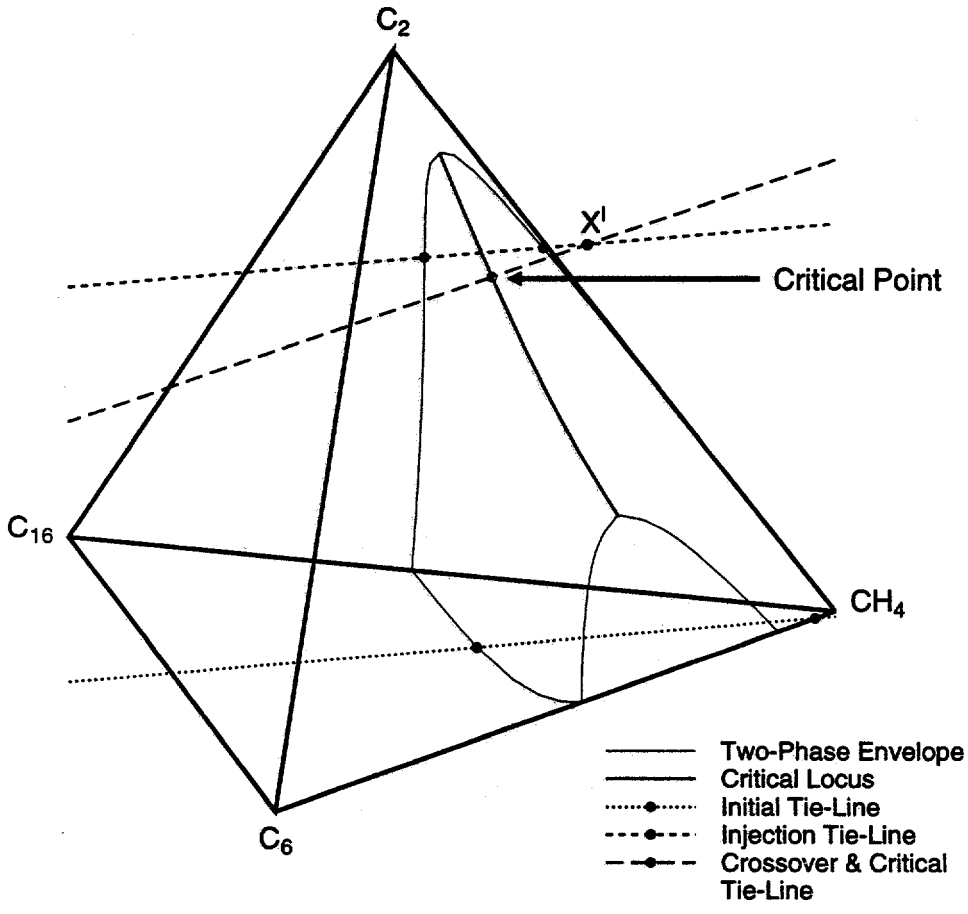

Figure 3.6: Phase diagram at 2244 psia (MMP) and 200°F (system 4).

demonstrated for systems in which the crossover tie line intersects the initial and injection tie lines. Similar techniques could be used in systems where the crossover tie line is determined by rarefaction surfaces. The technique demonstrated in this section can be applied to systems with an arbitrary number of components, if the relevant crossover tie lines can be identified. In the next section, we present results that suggest how that problem can be solved for systems with more than four components.

3.2 Global Triangular Structure in Four-Component Conservation Laws

T. Johansen [1], B. Dindoruk and F. M. Orr, Jr.

3.2.1 Introduction

Interactions of equilibrium phase behavior with multiphase flow lie at the heart of displacement processes in which oil is displaced from a porous medium by a gas mixture, by a surfactant mixture, or by water containing dissolved polymer. So-called multicontact miscible gas/oil displacements, for example, rely on chromatographic separations, which result when phases with differing equilibrium compositions flow at different velocities, to achieve high displacement efficiency. Similar compositional effects play key roles in chemical flooding processes. In any oil recovery process, hundreds of chemical components are present, but for the purposes of analysis, the phase behavior is always represented in terms of a small number of pseudocomponents, often only three. Recent research has indicated, however, that three-component descriptions of many processes do not reveal all the important aspects of the physical mechanisms, and hence it is desirable to increase the number of components included in the representation of the flow behavior. In this paper, we analyze the mathematical structure of Riemann problems for enhanced oil recovery processes when four components are present, and we show that under certain assumptions, the problems reduce to a series of simple geometric constructions that involve planar surfaces of tie lines. The displacement behavior on those surfaces is closely related to that obtained for ternary systems. For such systems, therefore, solutions to multicomponent flow problems can be found easily.

For one-dimensional, dispersion-free flow in which components do not change volume as they transfer between phases, the conservation equations are

$$\frac{\partial C_i}{\partial t} + \frac{\partial F_i}{\partial x} = 0, \qquad i = 1, n_c, \tag{3.14}$$

where t is a dimensionless time, and x is a dimensionless distance. C_i is the overall volume fraction of component i given by

$$C_i = \sum_{j=1}^{n_p} c_{ij} S_j, \qquad i = 1, n_c, \tag{3.15}$$

and F_i is the overall fractional flux of component i,

$$F_i = \sum_{j=1}^{n_p} c_{ij} f_j, \qquad i = 1, n_c. \tag{3.16}$$

In Eqs. 3.15 and 3.16, c_{ij} is the volume fraction of component i in phase j, and S_j is the saturation of phase j. The overall volume fractions satisfy

$$\sum_{i=1}^{n_c} C_i = 1, \tag{3.17}$$

[1] Norsk-Hydro, A.S., Oslo.

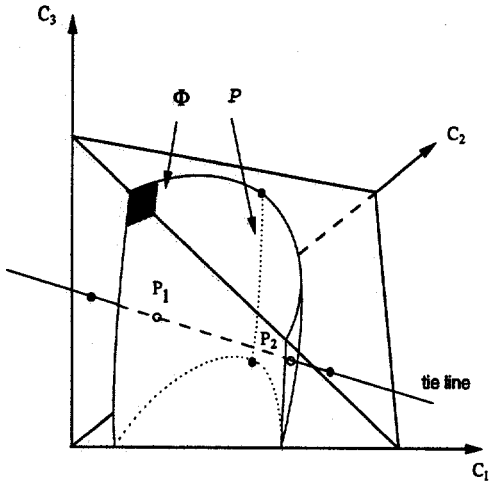

Figure 3.7: Composition space and two-phase region.

so only $n_c - 1$ of the conservation equations are independent. In addition, the phase saturations satisfy

$$\sum_{j=1}^{n_p} S_j = 1. \tag{3.18}$$

While we restrict the analysis in this paper to systems without volume change, we note the the principal results concerning tie line geometry also apply when components change volume as they transfer between phases [29].

Eq. 3.14 is derived on the assumption that any phases present are in chemical equilibrium. To complete specification of the problem, therefore, phase equilibrium information must be given. In the discussion that follows, it will be convenient to supply such information in two ways. One way is to specify equilibrium ratios, or K-values, defined as

$$K_i = \frac{c_{i1}}{c_{i2}}, \qquad i = 1, n_c. \tag{3.19}$$

In general, the K-values are functions of composition. They may be obtained from an equation of state, for example.

A second way to provide information about phase equilibrium is to specify the geometry of tie lines and then also describe the location in composition space of the surface of phase compositions. Equilibrium compositions are then given by the intersections of tie lines with the equilibrium surface.

In the analysis that follows, we consider flow of four components that form up to two phases in some region, Φ, of the space, Γ, of physically allowable compositions in which $C_i \geq 0$ and $C_1 + C_2 + C_3 \leq 1$. A central assumption is that the phases present at any spatial location are in chemical equilibrium. We also assume that the flow is isothermal and that the equilibrium phase behavior is independent of the pressure change that occurs due to the pressure gradient associated with flow. Fig. 3.7 shows a sketch of the composition space and a typical two-phase region.

Much of the behavior of the flow problems considered here is governed by the properties of tie lines, which in four-component systems are straight lines in the three-dimensional space that connect pairs of points on the boundary of Φ. Those points represent the compositions of the equilibrium phases. Through each composition point in Φ passes one and only one tie line, so that the interior of Φ is densely packed with tie lines. We assume that tie lines do not intersect inside Γ ($C_i > 0$ and $C_1 + C_2 + C_3 < 1$), though the extensions of tie lines can and do intersect on the

boundaries ($C_i = 0$ and $C_1 + C_2 + C_3 = 1$). (For a discussion of problems that arise when tie lines intersect in the interior of the composition space, see [65].) Eqs. 3.15 are the equations of the tie lines. For two-phase flow, Eqs. 3.15 can be written as functions of S_1 only, where S_1 can be viewed as a parameter that specifies location along the tie line. When $0 \leq S_1 \leq 1$ the overall composition lies within Φ, and when $S_1 > 1$ or $S_1 < 0$ only a single phase forms. In the analysis that follows, extensions of tie lines to compositions outside Γ will also prove useful.

We assume that Φ is sufficiently regular that each tie line intersects the boundary of Φ exactly twice. Therefore the surface of Φ must be divided into two parts (hence its designation as the *binodal* surface), one associated with the liquid phase (oil) and the other associated with the second phase. The second phase may be vapor in the case of gas/oil displacements or another liquid phase for surfactant flooding processes. At some temperatures and pressures, the liquid and vapor portions of the binodal surface of Φ meet at a locus of critical points at which the compositions and all the properties of the two phases are identical. In Fig. 3.7 that critical locus is labeled P. When a critical locus is absent, as is the case in gas/oil displacements when the pressure is low, the surfaces of Φ may intersect any or all of the surfaces of the composition space.

Riemann problems for Eq. 3.14 have been studied by many investigators from both engineering and mathematical points of view. On the engineering side, the focus has been on understanding the chromatographic separations that then can be used to design efficient oil recovery processes. In the context of describing the mechanisms of those processes, Eqs. 3.14 (or the equivalent molar conservation equations when volume change is included [36]) have been solved repeatedly for ternary systems by investigators of alcohol flooding, surfactant flooding and gas displacement processes, and the theory of three-component flows is largely complete. An extensive set of references to that literature is given by Johansen [61]. Investigations of four component problems have been limited to gas/oil displacements. Four-component solutions were first reported by Monroe *et al.* [89], and the properties of those solutions and many others were subsequently explored in detail by Dindoruk [29] and Johns [66] (see also [67, 30, 100]). Four-component solutions were also reported by Bedrikovetsky [8] for displacement processes with constant K-values. All those investigations showed that a solution to a Riemann problem, which can be represented as a sequence of shocks and rarefactions that generate a path through the state space, Γ, must lie on surfaces of tie lines illustrated in Fig. 3.8. One surface is associated with the left state (injection composition) and the other with the the right state (initial composition). This paper provides additional evidence that it is the geometry of tie lines in those surfaces that controls the structure of solutions.

On the mathematical side, much work has been devoted to questions of existence and uniqueness and to describing the wave structure of solutions. Investigations that have much in common with the problems considered here have been reported by Johansen and Winther [63, 64, 65].

In the analysis of polymer flooding [63, 64] and three-component, two-phase flow problems [65, 66], it has proved useful to rewrite the problem in terms of dependent variables that yield an eigenvalue problem for a triangular matrix. In that form, the analysis of wave structure is much more straightforward than it is for the eigenvalue problems associated with Eqs. 3.14. In this paper we employ the same strategy: we ask under what circumstances can a problem with triangular structure be obtained by a suitable model representation. We then consider what types of phase behavior produce triangular structure and show that only a small set of phase behavior types is allowed. However, we show that the types that do produce triangular structure are consistent with simplifying assumptions commonly used to describe the behavior of surfactant and gas/oil systems. It is also important to note, however, that the models considered here are always hyperbolic, even if the structure is not triangular [124].

For triangular models, the solution path in Γ lies on a sequence of easily defined surfaces of tie lines, and the solution wave structure can be described in a straightforward manner. While the

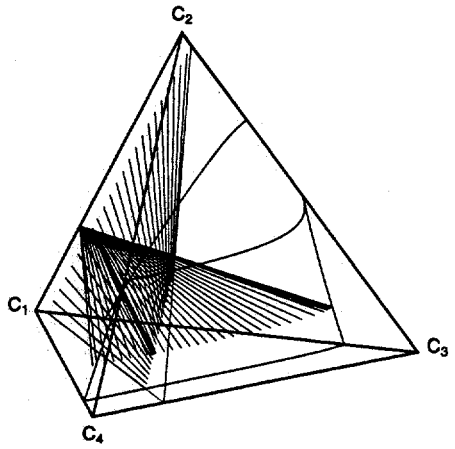

Figure 3.8: A quaternary phase diagram with ruled surfaces of tie lines.

assumptions required to make the problem triangular are fairly restrictive, the properties of the resulting solutions provide considerable guidance about solutions to more general problems, and hence the structures described here are a useful step toward understanding of truly multicomponent flows by extending the techniques employed in the analysis of multicomponent polymer flows [64].

In the sections that follow, we state and prove a theorem about tie line geometry. We then show that expressions for eigenvalues and eigenvectors can be obtained easily for four-component conservation equations with global triangular structure, and we examine the wave structure of solutions. We show that triangular structures result when equilibrium K-values are independent of composition. We conclude with a discussion of other approximate phase behavior models that would also yield triangular structure.

3.2.2 Global Triangular Structure

It is convenient for analysis to write the conservation equations in terms of the properties of tie lines, which control solution structure and behavior. To do so, we represent the equation of a general tie line as

$$C_2 = \alpha(\xi,\eta)C_1 + \phi(\xi,\eta), \tag{3.20}$$

$$C_3 = \beta(\xi,\eta)C_1 + \theta(\xi,\eta), \tag{3.21}$$

where α and β are slopes of the tie line, and ϕ and θ are intercepts with the $C_1 = 0$ face. ξ and η are new dependent variables that determine the location of some point in Γ. Substitution of Eqs. 3.20 and 3.21 into Eqs. 3.14 yields the model formulation,

$$\frac{\partial u}{\partial t} + A(u)\frac{\partial u}{\partial x} = 0, \tag{3.22}$$

where $u = (C_1, \xi, \eta)^T$ and

$$A(u) = \begin{pmatrix} \frac{\partial F_1}{\partial C_1} & \frac{\partial F_1}{\partial \xi} & \frac{\partial F_1}{\partial \eta} \\ 0 & \frac{G}{D} & \frac{(C_1 - F_1)}{D} L \\ 0 & \frac{(C_1 - F_1)}{D} M & \frac{H}{D} \end{pmatrix}. \tag{3.23}$$

The entries in $A(u)$ are given by

$$G = \left(C_1 \frac{\partial \beta}{\partial \eta} + \frac{\partial \theta}{\partial \eta}\right)\left(F_1 \frac{\partial \alpha}{\partial \xi} + \frac{\partial \phi}{\partial \xi}\right) -$$

$$\left(C_1\frac{\partial\alpha}{\partial\eta}+\frac{\partial\phi}{\partial\eta}\right)\left(F_1\frac{\partial\beta}{\partial\xi}+\frac{\partial\theta}{\partial\xi}\right), \tag{3.24}$$

$$H=\left(C_1\frac{\partial\alpha}{\partial\xi}+\frac{\partial\phi}{\partial\xi}\right)\left(F_1\frac{\partial\beta}{\partial\eta}+\frac{\partial\theta}{\partial\eta}\right)-$$
$$\left(C_1\frac{\partial\beta}{\partial\xi}+\frac{\partial\theta}{\partial\xi}\right)\left(F_1\frac{\partial\alpha}{\partial\eta}+\frac{\partial\phi}{\partial\eta}\right), \tag{3.25}$$

$$D=\left(C_1\frac{\partial\alpha}{\partial\xi}+\frac{\partial\phi}{\partial\xi}\right)\left(C_1\frac{\partial\beta}{\partial\eta}+\frac{\partial\theta}{\partial\eta}\right)-$$
$$\left(C_1\frac{\partial\beta}{\partial\xi}+\frac{\partial\theta}{\partial\xi}\right)\left(C_1\frac{\partial\alpha}{\partial\eta}+\frac{\partial\phi}{\partial\eta}\right), \tag{3.26}$$

$$L=\left(\frac{\partial\beta}{\partial\eta}\frac{\partial\phi}{\partial\eta}-\frac{\partial\alpha}{\partial\eta}\frac{\partial\theta}{\partial\eta}\right), \tag{3.27}$$

$$M=\left(\frac{\partial\alpha}{\partial\xi}\frac{\partial\theta}{\partial\xi}-\frac{\partial\beta}{\partial\xi}\frac{\partial\phi}{\partial\xi}\right). \tag{3.28}$$

We assume that the mapping $(C_1,\xi,\eta)\rightarrow(C_1,C_2,C_3)$ is 1-1, and therefore, that $D\neq 0$.

We now ask what conditions are required for the matrix $A(u)$ to have triangular structure for all composition points within the two-phase region. It is apparent that Eq. 3.22 has global triangular structure if and only if either

$$L=0 \tag{3.29}$$

or

$$M=0 \tag{3.30}$$

We now examine tie-line geometries for which either of the conditions for triangular structure (Eqs. 3.29 or 3.30) holds. To do so we define the functions α, β, ϕ, and θ in terms of ξ and η. The geometry of the parameterization is illustrated in Fig. 3.9. We choose η to be the slope of a tie line in the $C_3=0$ face. For simplicity of description only, we assume that $\eta\geq 0$. Let $\gamma(\eta)$ be the intercept of the tie line with the C_2 axis. Let $C_2=g(C_3,\eta)$ be any smooth function such that its graph in the $C_1=0$ face passes through the point $(0,\gamma(\eta),0)$. We choose the second parameter ξ to be the value of C_3 where a tie line in the interior of Γ intersects the $C_1=0$ face. A point on the g curve then determines a single tie line in the interior that intersects the $C_1=0$ surface at the point $C_1=0$, $C_2=g(\xi,\eta)$, $C_3=\xi$.

Tie lines that intersect this curve also intersect the $C_3=0$ face at points $P(\xi,\eta)=(a(\xi,\eta),\ b(\xi,\eta),\ 0)$, where a and b are smooth functions of ξ and η. Fig. 3.9 shows the geometry of the tie-line representation. A general tie-line PQ (Fig. 3.9) is given, therefore, by

$$C_1 = -sa, \tag{3.31}$$
$$C_2 = g+s(g-b), \tag{3.32}$$
$$C_3 = \xi+s\xi, \tag{3.33}$$

where s is a parameter that determines position along the tie line. Elimination of s gives

$$C_2 = \frac{b-g}{a}C_1+g, \tag{3.34}$$
$$C_3 = -\frac{\xi}{a}C_1+\xi. \tag{3.35}$$

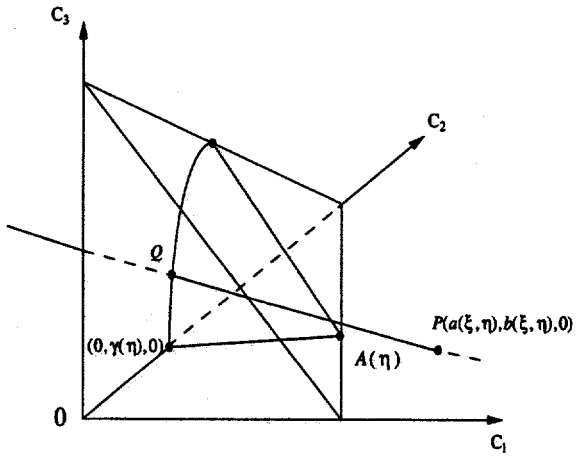

Figure 3.9: Representation of tie lines.

Comparison of Eqs. 3.34 and 3.35 with Eqs. 3.20 and 3.21 gives definitions for α, β, ϕ, and θ,

$$\alpha(\xi,\eta) = \frac{b(\xi,\eta)-g(\xi,\eta)}{a(\xi,\eta)}, \tag{3.36}$$

$$\phi(\xi,\eta) = g(\xi,\eta), \tag{3.37}$$

$$\beta(\xi,\eta) = -\frac{\xi}{a(\xi,\eta)}, \tag{3.38}$$

$$\theta(\xi,\eta) = \xi. \tag{3.39}$$

We now state and prove a key result of this paper:

Theorem 1. *A problem has global triangular structure if and only if either*

(i) All tie-line extensions intersect the C_1/C_2 edge of the quaternary diagram,

or

(ii) All tie-line extensions lie in planes spanned by two intersecting tie lines that lie in the $C_3 = 0$ and $C_4 = 0$ faces of the quaternary diagram.

The geometries of tie lines that result in triangular structure are illustrated in Fig. 3.10.

Substitution of Eqs. 3.36–3.39 into Eq. 3.27 indicates that Eq. 3.29 is satisfied if and only if

$$\frac{\partial a}{\partial \eta} = 0 \ \ or \ \ \frac{\partial g}{\partial \eta} = 0. \tag{3.40}$$

The condition on $\partial a/\partial\eta$ would require that the tie lines lie in a plane that intersects the $C_3 = 0$ face in a straight line at constant a. It would be physically impossible for tie lines in the $C_4 = 0$ face to do so, however, so we exclude this case on physical grounds.

The condition that $\partial g/\partial\eta = 0$ would require that all the tie lines at constant ξ intersect the $C_1 = 0$ face at constant $g = C_2$. If $g \neq 0$ the resulting tie line geometry would produce tie lines that would intersect in the two-phase region, a physically unacceptable situation that we exclude because it violates our fundamental assumptions. If $g = 0$, all tie lines would intersect at the C_3 axis. That situation is already included in part (i) of the theorem. Hence we focus our attention on Eq. 3.30.

Substitution of Eqs. 3.36–3.39 into Eq. 3.28 indicates that Eq. 3.30 is satisfied if and only if

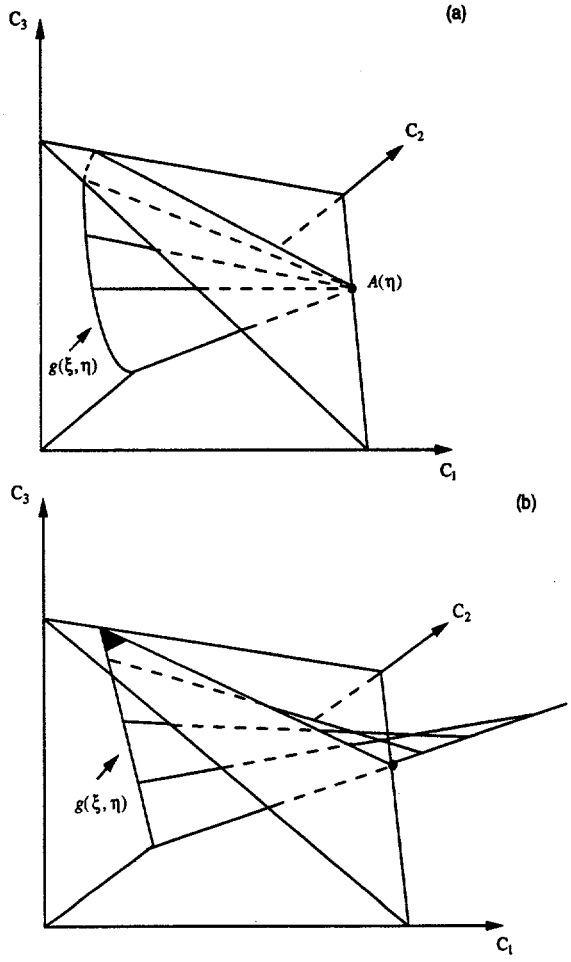

Figure 3.10: Triangular tie-line geometries.

$$\frac{\partial a}{\partial \xi}\left(\xi\frac{\partial g}{\partial \xi}+b-g\right)=a\frac{\partial b}{\partial \xi} \tag{3.41}$$

Proof: We assume first that the model has global triangular structure (Eq. 3.30 is satisfied).

If $\partial a/\partial \xi = 0$ then $\partial b/\partial \xi$ must also be zero according to Eq. 3.41. That can happen only if all tie lines corresponding to a given η pass through a single point which must lie on the C_1/C_2 axis, because tie lines that lie in both the $C_3 = 0$ and $C_4 = 0$ faces must pass through it. Hence, that point must be $A(\eta)$ in Fig. 3.10, and (1.i) follows from triangularity.

If $\partial a/\partial \xi \neq 0$, (except possibly at isolated points), Eq. 3.41 can be written for fixed η (and for $\xi \neq 0$) as

$$\frac{dg}{d\xi}-\frac{g(\xi)}{\xi}=\frac{a\frac{db}{d\xi}-b\frac{da}{d\xi}}{\xi\frac{da}{d\xi}} \tag{3.42}$$

Let the right side of Eq. 3.42 be $\xi R(\xi)$. It follows that

$$g(\xi)=\xi\left[K+\int R(\xi)d\xi\right], \tag{3.43}$$

where K is a constant. Differentiation of Eq. 3.43 gives an expression for $dg/d\xi$, which can be differentiated again to obtain an expression for $d^2g/d\xi^2$. Substitution for $R(\xi)$ and $dR/d\xi$ in that expression gives

$$\frac{d^2g}{d\xi^2}=\frac{a}{\xi}\frac{d}{d\xi}\left(\frac{db}{da}\right). \tag{3.44}$$

According to Eq. 3.44, if $d^2g/d\xi^2 = 0$ then db/da is a constant, which can only be true if a and b lie on a straight line. That line must be the tie line in the $C_3 = 0$ face with slope η, as Fig. 3.10 shows.

The final part of the proof is to show that if (1.i) or (1.ii) is satisfied, then the model has triangular structure. If (1.i) is true, then $\partial a/\partial \xi = \partial b/\partial \xi = 0$, and Eq. 3.41 is trivially satisfied. Hence, Part (i) is proved.

If (1.ii) is true, then

$$b(\xi,\eta)=\eta a(\xi,\eta)+\gamma(\eta), \tag{3.45}$$

and

$$g(\xi,\eta)=\kappa(\eta)\xi+\gamma(\eta), \tag{3.46}$$

where $\kappa(\eta)$ is some smooth function. Differentiation of Eqs. 3.45 and 3.46 followed by substitution into the left side of Eq. 3.41 gives $\eta a\ da/d\xi$, which is also the value of the right side of Eq. 3.41. Hence, the condition for triangular structure is satisfied, and Part (ii) is also proved.

3.2.3 Wave Analysis for Triangular Models

In this section, we derive the basic wave properties for the planar tie lines of part (ii) of the theorem. The analysis is essentially the same for part (i) (tie lines that meet at an edge). The details of some of the expressions differ, but the key results are the same. A detailed analysis for the tie line situation of part (i) is given by Johansen [62]. We note only in passing that ternary models of surfactant phase behavior make use of "Hand's rule" [77], in which tie lines extend through one corner of the diagram, exactly the situation included in part (i). Thus, the results obtained in this section could be applied to obtain analytical solutions to a four-component model of surfactant

flooding in which salinity or cosolvent concentration is represented as a component separate from the traditional oil, water, and surfactant components.

Substitution of Eqs. 3.45 and 3.46 into the expressions for α, β, ϕ and θ (Eqs. 3.36–3.39) allows evaluation of the entries in $A(u)$ (Eqs. 3.24–3.26),

$$D = E(C_1 + p)(C_1 + h), \tag{3.47}$$
$$G = E(F_1 + p)(C_1 + h), \tag{3.48}$$
$$H = E(F_1 + h)(C_1 + p), \tag{3.49}$$

where

$$p = \frac{a^2}{\xi \frac{\partial a}{\partial \xi} - a}, \tag{3.50}$$

$$h = \frac{a\left(\xi \frac{d\kappa}{d\eta} + \frac{d\gamma}{d\eta}\right)}{\xi \frac{d\kappa}{d\eta} - a}, \tag{3.51}$$

$$E = \frac{\left(\xi \frac{\partial a}{\partial \xi} - a\right)\left(\xi \frac{d\kappa}{d\eta} - a\right)}{a^3}. \tag{3.52}$$

The matrix, $A(u)$, now becomes

$$A(u) = \begin{pmatrix} \frac{\partial F_1}{\partial C_1} & \frac{\partial F_1}{\partial \xi} & \frac{\partial F_1}{\partial \eta} \\ 0 & \frac{F_1+p}{C_1+p} & U \\ 0 & 0 & \frac{F_1+h}{C_1+h} \end{pmatrix}. \tag{3.53}$$

where

$$U = \frac{\xi(C_1 - F_1)}{Da^2} \frac{\partial a}{\partial \eta} \frac{\partial g}{\partial \eta}. \tag{3.54}$$

We now consider the rarefaction waves associated with the eigenvalues of $A(u)$,

$$\lambda_1 = \frac{\partial F_1}{\partial C_1}; \quad \lambda_2 = \frac{F_1 + p}{C_1 + p}; \quad \lambda_3 = \frac{F_1 + h}{C_1 + h}. \tag{3.55}$$

Rarefaction waves corresponding to λ_1 take place at constant values of ξ and η, and hence they represent variations along fixed tie lines. These waves correspond, therefore, to rarefaction waves of the scalar conservation equation,

$$\frac{\partial C_1}{\partial t} + \frac{\partial F_1(C_1, \xi_0, \eta_0)}{\partial x} = 0, \tag{3.56}$$

for constant ξ_0 and η_0. Eq. 3.56 is an analog of the familiar Buckley-Leverett equation.

The rarefaction waves for λ_2 are determined by

$$(\lambda_1 - \lambda_2)\frac{dC_1}{d\tau} + \frac{\partial F_1}{\partial \xi}\frac{d\xi}{d\tau} + \frac{\partial F_1}{\partial \eta}\frac{d\eta}{d\tau} = 0, \tag{3.57}$$

$$U\frac{d\eta}{d\tau} = 0, \tag{3.58}$$

$$(\lambda_3 - \lambda_2)\frac{d\eta}{d\tau} = 0, \tag{3.59}$$

where $\tau = x/t$. It follows that the λ_2 waves take place at constant values of η. For $\eta = \eta_0$, these waves are determined by

$$(\lambda_1 - \lambda_2)\frac{dC_1(\xi)}{d\xi} + \frac{dF(C_1, \xi, \eta_0)}{d\xi} = 0. \tag{3.60}$$

Next we consider shock waves for a planar surface of tie lines (1.ii). The classical Rankine-Hugoniot shock balances are

$$\Lambda(C_1^L - C_1^R) = F_1^L - F_1^R, \tag{3.61}$$

$$\Lambda(\alpha^L C_1^L + \phi^L - \alpha^R C_1^R + \phi^R) = \alpha^L F_1^L + \phi^L - \alpha^R F_1^R + \phi^R, \tag{3.62}$$

$$\Lambda(\beta^L C_1^L + \theta^L - \beta^R C_1^R + \theta^R) = \beta^L F_1^L + \theta^L - \beta^R F_1^R + \theta^R, \tag{3.63}$$

where L and R refer to the upstream and downstream sides of the shock, and Λ is the shock velocity.

It is clear that Eqs. 3.61–3.63 can be satisfied with $\xi^L = \xi^R$ and $\eta^L = \eta^R$. These are the tie-line shocks that correspond to the scalar conservation equation, Eq. 3.56. Rearrangement of Eq. 3.61 shows that when a shock connects a composition in the single-phase region with a composition in the two-phase region, the single-phase composition must lie on the extension of a tie line, as several investigators have shown [79, 52, 36].

When $\xi^L \neq \xi^R$, we define

$$k^{LR} = \frac{\phi^L - \phi^R}{\alpha^L - \alpha^R}; \quad h^{LR} = \frac{\theta^L - \theta^R}{\beta^L - \beta^R}. \tag{3.64}$$

Elimination of F^L or F^R from Eqs. 3.62 and 3.63 gives expressions for the shock velocity,

$$\Lambda = \frac{F^L + k^{LR}}{C^L + k^{LR}} = \frac{F^R + k^{LR}}{C^R + k^{LR}} = \frac{F^L + h^{LR}}{C^L + h^{LR}} = \frac{F^R + h^{LR}}{C^R + h^{LR}}. \tag{3.65}$$

Substitution of the definitions of α, β, and θ (Eqs. 3.36, 3.38, 3.39) along with the expressions for b and g that define planar tie lines (Eqs. 3.45 and 3.46) into Eq. 3.64 shows that $h^{LR} = k^{LR}$ if $\xi^L \neq \xi^R$ and $\eta^L = \eta^R$, which is therefore a sufficient condition for Eqs. 3.61–3.63 to be satisfied. Thus, shocks satisfying Eq. 3.65 are contained in the tie-line surfaces. That result is consistent with the observation that a shock that connects any two compositions in the two-phase region (which therefore lie on two different tie lines) can only occur if the extensions of the two tie lines intersect [66, 67]. As Fig. 3.10b shows, all the tie lines that lie in the plane at constant η intersect. The statement that tie lines connected by a shock must intersect is also true for systems with any number of components, whether or not components change volume as they change phase [29, 30].

We summarize these results in the following

Theorem 2. *Rarefaction and shock waves corresponding to λ_1 take place along fixed tie lines, whether or not the model has triangular structure. The rarefaction and shock waves corresponding to λ_2 are contained in the tie-line planes at constant values of η.*

A similar result holds when the global triangular structure results from tie lines that extend through an edge of the quaternary diagram [62]. Thus, we have shown that when a model is triangular, the shock and rarefaction surfaces coincide.

In the analysis so far, only tie-line waves and waves with constant η and varying ξ have been considered. As Fig. 3.8 illustrates, however, solutions to four-component Riemann problems lie on

two surfaces of tie lines, one associated with the initial tie line (left state), and another associated with the injection tie line (right state). The behavior of the second surface is determined by waves associated with the λ_3 eigenvalue,

$$(\lambda_1 - \lambda_3)\frac{dC_1}{d\tau} + \frac{\partial F_1}{\partial \xi}\frac{d\xi}{d\tau} + \frac{\partial F_1}{\partial \eta}\frac{d\eta}{d\tau} = 0, \tag{3.66}$$

$$(\lambda_2 - \lambda_3)\frac{d\xi}{d\tau} + U\frac{d\eta}{d\tau} = 0. \tag{3.67}$$

When a λ_3 shock exists, it is defined by

$$h^{LR} = k^{LR},\ \xi^L \neq \xi^R,\ \eta^L \neq \eta^R. \tag{3.68}$$

For such waves, both ξ and η will change across the shock [62], and again, the tie lines connected by the shock must intersect [66, 29]. If the surface of tie lines associated with those waves is also planar or consists of tie lines that extend through an edge of the four-component diagram, then the model system will be triangular for the second surface as well. In that case, Theorems 1 and 2 still apply if we choose another of the faces of the quaternary diagram in which to parameterize the tie lines. Hence, triangular structure in that representation is also equivalent to tie-line surfaces that are planes, though the new set of planes is "orthogonal" to the planes already discussed. The solution to a Riemann problem is constructed, therefore, by finding the two surfaces of tie lines, which intersect in a unique tie line known as the crossover tie line [89]. If the system is doubly triangular, the crossover tie line can be found easily as the intersection of two planes [29]. If, however, the problem structure is not triangular, shock and rarefaction surfaces, in general, will not coincide.

3.2.4 Constant K-Values

In this section we examine a phase equilibrium model, equilibrium K-values that are independent of composition, that shows triangular structure. K-values are approximately independent of composition for gas/oil systems when the pressure is low enough (at a given temperature) that no critical points appear in Γ.

If K-values are constant, then the surface of liquid compositions is given by

$$\sum_{i=1}^{4} K_i C_i = \sum_{i=1}^{4} K_i c_{i1} = 1, \tag{3.69}$$

and the vapor surface is given by

$$\sum_{i=1}^{4} \frac{C_i}{K_i} = \sum_{i=1}^{4} \frac{c_{i2}}{K_i} = 1. \tag{3.70}$$

Elimination of C_4 from Eqs. 3.69 and 3.70 with Eq. 3.17 shows that both surfaces are planes.

To show that Theorems 1 and 2 apply, we need only show that tie lines for constant values lie in planes like that shown in Fig. 3.10b. To do so, we consider three vectors: $\vec{e}_b$, the direction of a tie line in the $C_3 = 0$ face, $\vec{e}_f$, the direction of a tie line in the $C_4 = 0$ face that intersects the first tie line, and $\vec{e}_i$, that of a tie line in the interior of Γ that also intersects the first tie line. Those vectors are

$$\vec{e}_b = (K_1 - 1)c_{11}^b \vec{e}_1 + (K_2 - 1)c_{21}^b \vec{e}_2, \tag{3.71}$$

$$\vec{e}_f = (K_1 - 1)c_{11}^f \vec{e}_1 + (K_2 - 1)c_{21}^f \vec{e}_2 + (K_3 - 1)c_{31}^f \vec{e}_3, \tag{3.72}$$

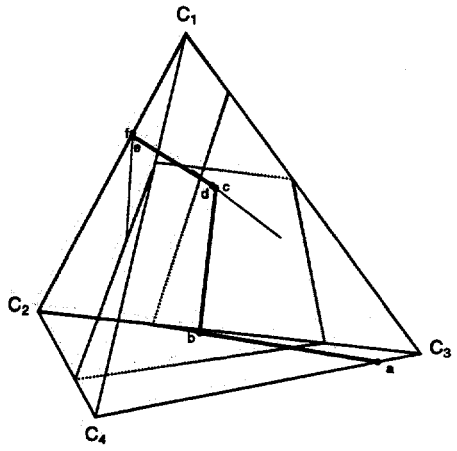

Figure 3.11: Composition route for displacement of a C_3/C_4 mixture by a C_1/C_2 mixture with $K_1 = 1.5$, $K_2 = 2.8$, $K_3 = 0.4$, and $K_4 = 0.01$.

$$\vec{e}_i = (K_1 - 1)c_{11}^i \vec{e}_1 + (K_2 - 1)c_{21}^i \vec{e}_2 + (K_3 - 1)c_{31}^i \vec{e}_3. \tag{3.73}$$

The tie line can be chosen by selecting c_{11}^b. The remaining compositions are determined by selecting an intersection point on the tie line in the $C_3 = 0$ face and solving the equations of the three tie lines simultaneously. The three vectors lie in the same plane if $\vec{e}_i \cdot (\vec{e}_b \times \vec{e}_f) = 0$. Direct evaluation of the algebraically complex expressions verifies that the tie lines that intersect the tie line in the $C_3 = 0$ face do form a plane. In fact, the constant K-value system is doubly triangular. Hence, the solution composition path lies entirely on planar surfaces in such systems.

Fig. 3.11 shows the composition path for a constant K-value system with $K_1 = 1.5$, $K_2 = 2.8$, $K_3 = 0.4$, and $K_4 = 0.01$ [29]. The injection composition is a mixture of components 1 and 2 and the initial mixture contains all components except component 1. According to Theorems 1 and 2, the solution composition path must lie entirely on two planes of tie lines that contain the initial and injection tie lines, and the crossover tie line is the intersection of those planes. Dindoruk showed that such systems can be characterized conveniently in terms of the properties of the envelope curve of the tie lines that lie in each of the planes [29]. In this example, the λ_2 and λ_3 waves are both self-sharpening, and hence, rarefactions can occur only on the three tie lines. In the example shown, however, a rarefaction appears only on the crossover tie line; the other two are missing because rarefactions there would violate wave compatibility requirements. Details of the analysis that leads to the set of compatible waves and shocks that make up the solution are given by Dindoruk [29]. Compositions, gas saturations, and wave velocities of the points labeled in Fig. 3.11 are given in Table 3.2.4.

Composition profiles for the solution are shown in Fig. 3.12. Those profiles illustrate the idea that the displacement consists of a series of composition waves that are sorted in K-value order [29, 66]. Component 2, which has the highest K-value, appears in a fast-moving, leading bank. Components 3 and 4 present in the initial mixture disappear in a sequence of trailing evaporation shocks.

Because the entire solution consists only of shocks and one rarefaction along the crossover tie line, the solution is quite easy to construct once the crossover tie line is identified. The shocks from the initial and injection tie lines to the crossover tie line are intermediate discontinuities that satisfy conditions equivalent to the familiar Welge tangent construction for a Buckley-Leverett problem. Thus, solutions can be found easily for displacements in which tie-line surfaces are planar.

Table 3.3: Method of characteristics solution for a quaternary displacement with $K_1 = 1.5$, $K_2 = 2.8$, $K_3 = 0.4$ and $K_4 = 0.01$.

Composition Label	Composition (Volume Fraction)				Gas Saturation (Vol. Fraction)	Wave Velocity (λ)
	C_1	C_2	C_3	C_4		
a	0.0000	0.0000	0.8690	0.1310	0.0000	1.0795
b	0.0000	0.5483	0.4173	0.0344	0.5994	1.0795-1.0548
c	0.4911	0.2200	0.2729	0.0160	0.7334	1.0548
d	0.4982	0.2267	0.2614	0.0137	0.7727	0.8348
e	0.6342	0.3527	0.0000	0.0131	0.9804	0.8348-0.3642
f	0.6406	0.3594	0.0000	0.0000	1.0000	0.3642

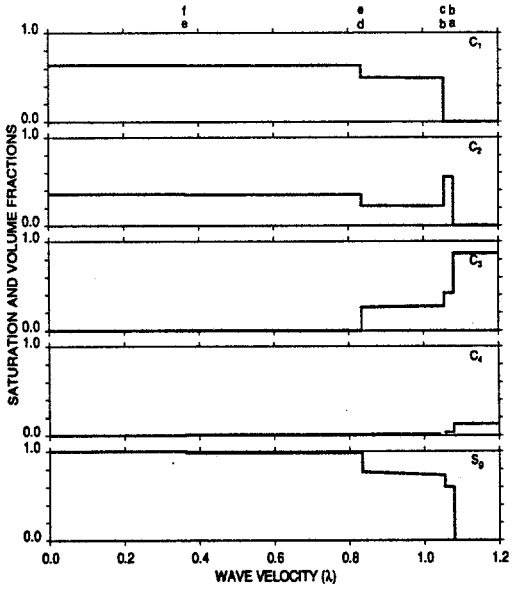

Figure 3.12: Composition and saturation profiles for a four-component displacement with constant K-values.

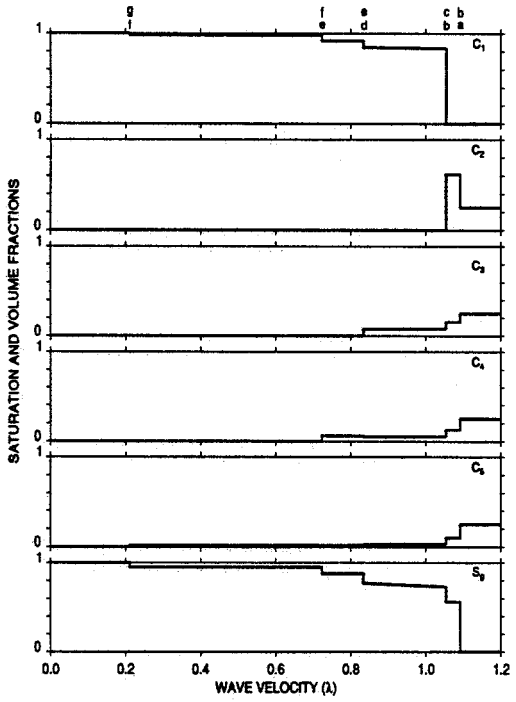

Figure 3.13: Composition and saturation profiles for a five-component displacement with constant K-values.

The idea that constant K-values create planar tie-line surfaces can be applied to systems with more than four components. For example, Fig. 3.13 shows composition profiles for a system with five components. The system is the same as that described in Figs. 3.11 and 3.12 except that another component with $K_4 = 0.2$ has been added, and Component 4 has been renamed to be Component 5 with $K_5 = 0.01$. Also, the injection fluid is pure Component 1. Table 3.2.4 reports key values of composition, gas saturation, and wave velocity for the solution shown in Fig. 3.12. In this system, two crossover tie lines are present. The addition of another component with a relatively low K-value adds another slow-moving evaporation shock to the solution. Details of the construction of the solution shown in Fig. 3.13 are given by Dindoruk [29]. The solution shown in Fig. 3.13 demonstrates that the properties of systems with triangular structure can be exploited to advantage in the construction of solutions with more than four components.

3.2.5 Other Planar Systems

While systems with constant K-values provide very useful guidance about the structure of multicomponent flow problems, they cannot be used to investigate multicontact miscibility [100, 67] because no critical points are present. It is still possible, however, to take advantage of the properties of triangular structure to study multicontact miscibility. Specifying K-values, whether they are constant or they are determined from an equation of state, determines both the tie-line geometry and the location of the binodal surface. It is possible, however, to specify the binodal surface independently from tie-line geometry, an approximation that will be reasonable if tie lines in the actual system lie in surfaces that are nearly planar. Direct calculation with the Peng-Robinson equation of state for mixtures of CO_2 with normal alkanes, for instance, indicates that such surfaces are, in fact, nearly planar. Consider, for example, the phase diagram shown in Fig. 3.14. It shows a two-phase region that has critical points in the $C_2 = 0$ and $C_3 = 0$ faces. A locus of critical points in the interior of Γ connects the critical points in the faces. Suppose now that tie lines for

Table 3.4: Method of characteristics solution for a five component displacement with $K_1 = 1.5$, $K_2 = 2.8$, $K_3 = 0.4$, $K_4 = 0.2$ and $K_5 = 0.01$.

Composition Label	Composition (Volume Fraction)					Gas Saturation (Vol. Fraction)	Wave Velocity (λ)
	C_1	C_2	C_3	C_4	C_5		
a	0.0000	0.2500	0.2500	0.2500	0.2500	0.0000	1.0922
b	0.0000	0.6167	0.1559	0.1270	0.1004	0.5634	1.0922-1.0548
c	0.8345	0.0000	0.0800	0.0531	0.0324	0.7334	1.0548
d	0.8466	0.0000	0.0766	0.0490	0.0278	0.7727	0.8348
e	0.9184	0.0000	0.0000	0.0613	0.0203	0.8789	0.8348-0.7239
f	0.9798	0.0000	0.0000	0.0000	0.0202	0.9463	0.7239-0.2117
g	1.0000	0.0000	0.0000	0.0000	0.0000	1.0000	0.2117

this system lie in two sets of planes, each of which is tangent to an envelope curve. The envelope curve for one set (E_1 in Fig. 3.14) lies in a vertical plane normal to the C_1/C_2 axis. The second envelope curve (E_2 in Fig. 3.14) lies in the $C_3 = 0$ plane. The shapes of the envelope curves can be chosen to match tie-line slopes approximately to experimental data or to phase compositions calculated with an equation of state. K-values can be calculated by finding the intersections of tie lines in the various planar surfaces with the phase envelope.

Tie-line geometries like those of Fig. 3.14 allow straightforward construction of solutions. The crossover tie line can be identified easily as the only tie line common to the planes in which the initial and injection tie lines lie. Displacements in which one of the three key tie lines is a critical tie line will be multicontact miscible [100, 67].

3.2.6 Summary

The analysis given provides additional evidence that the geometry of tie lines controls the behavior of solutions to one-dimensional Riemann problems for multicomponent, two-phase flow. If and only if tie lines are arranged so that they meet at a point on one edge of a four-component phase diagram, or tie lines lie in planar surfaces, shock and rarefaction surfaces coincide. In such situations, analysis of wave structures is straightforward, and solutions for arbitrary left and right states can be constructed easily.

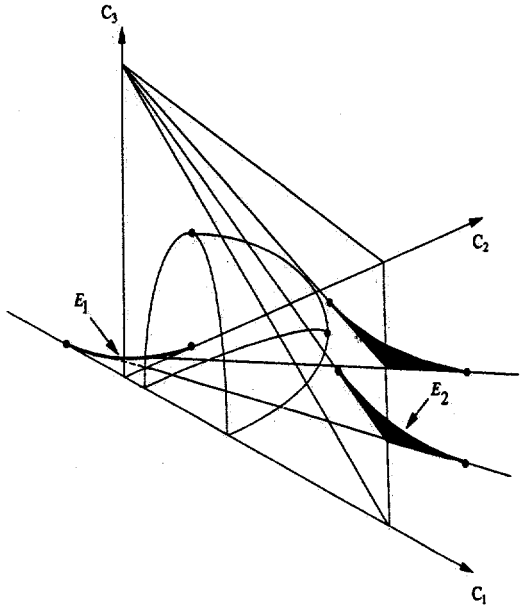

Figure 3.14: A doubly triangular system with variable K-values.

4. Interaction of Gravity, Capillary and Gravity Forces in Heterogeneous Systems

In this chapter, we examine the interplay of forces that control the distributions of the residual oil in the pore space. Consider, for example, a near-miscible gas injection process in a fractured reservoir. Because the process is not quite miscible, and there exists initial water, three-phase flow occurs. Capillary forces created by the interfacial tension (IFT) act to hold the oil in the reservoir rock, while the density differences between gas and oil drives oil to the bottom part of the reservoir. The relative magnitudes of the capillary, gravity and viscous forces govern the distribution of oil and gas phases in a reservoir, and consequently, the oil recovery mechanisms. Thus, understanding the interplay of capillary, gravity and viscous forces is of considerable importance to the description of near-miscible gas injection process performance.

In Section 4.1, we report a study of the influence of gravity and viscous forces on the residual oil saturation in a two-phase system. Our pore-level models suggest that the gravity and viscous forces are additive in determining the final residual oil saturation. Experimental observations from sandpacks support our models. In Section 4.2, we present results from a theoretical and experimental investigation of three-phase flow and gravity drainage. We discuss the roles of the spreading coefficient (C_s) and the Bond number ratio (α) in the process of three-phase gravity drainage. Our experiments and theory show that we can recover almost all oil from the top part of a reservoir if the system is water-wet and has a value of α greater than 1. Furthermore, we present an argument that near-miscible gas injection processes can be used to create situations with $\alpha > 1$. We also examine the contribution of crevices in the pores to oil drainage processes. In Section 4.3, we detail the prediction of the spreading and stability of thin hydrocarbon films based on the analysis of intermolecular forces. Lifshitz theory is used to evaluate the intermolecular interaction. That analysis is used to determine when oil films can be expected to permit gravity drainage to reduce remaining oil or condensate saturations to low values. Finally, in Section 4.4, we report experimental results for gravity drainage of crude oil in the presence of CO_2 at high pressure. These results demonstrate that gravity drainage can be an effective oil recovery mechanisms from fractured reservoirs.

4.1 The Effects of Gravity and Viscous Forces on Residual Oil Saturation

Dengen Zhou

4.1.1 Introduction

Tertiary oil recovery or aquifer remediation processes attempt to recover oil that is trapped by capillary forces. Displacement of a hydrocarbon phase by water alone is an immiscible displacement that cannot completely recover oil from reservoirs due to the interplay of capillary forces with heterogeneities of the media. Two types of heterogeneities are commonly dealt with: pore-level heterogeneity and macroscopic heterogeneity. Pore-level heterogeneity, such as pore size (grain size) and pore structure variations, controls the amount of oil left after the injected fluid has swept a zone, whereas macroscopic heterogeneity determines zones that the injected fluid sweeps. In numerical simulation of a displacement process, macroscopic heterogeneity can be represented directly by

assigning different rock properties (permeability and porosity) to certain grid blocks, given knowledge of the detailed structure of the medium. Because of the complex nature of pore entrapment mechanisms, however, the effects of pore level heterogeneity are represented by empirical correlations. One of the empirical correlations is the capillary desaturation curve (CDC), which defines the relationship of the residual oil saturation and the physical properties of a system. Accurate representation of the dependence of the CDC on fluid and rock properties is of great importance for simulations of enhanced oil recovery and spilled oil clean-up processes, because these processes must reduce the residual oil saturation to relatively low levels. This work describes theory and experiments that demonstrate the relative contributions of gravity, viscous and capillary forces in the correlation of residual oil saturation and the physical properties of water-wet systems.

The physical properties of a system are commonly represented by a capillary number, which is usually defined by one of the following equations

$$N_{c1} = \frac{\mu_w v}{\sigma}, \tag{4.1}$$

or

$$N_{c2} = \frac{k_w \nabla p}{\sigma} = \frac{\mu_w v_w}{\sigma k_{rw}}, \tag{4.2}$$

and a Bond number defined by

$$N_B = \frac{\Delta \rho g k}{\sigma}, \tag{4.3}$$

or

$$B = \frac{\Delta \rho g R^2}{\sigma}, \tag{4.4}$$

where μ_w is the viscosity of the displacing phase, v is Darcy velocity, ∇p is the pressure gradient, k is permeability, R is the radius of the grains composing the porous medium, $\Delta\rho$ is the density differences between the fluids, and σ is the interfacial tension (IFT) of the system. According to Darcy's law, the capillary numbers (N_{c1} and N_{c2}) are related by $N_{c2} = N_{c1}/k_{rw}$, where k_{rw} is the relative permeability of the displacing phase. The use of N_{c1} or N_{c2} in the literature depends on the application to specific situations. N_{c1}, for example, is likely to be used to correlate results of experiments with constant injection rates, whereas N_{c2} may be used to describe flows with constant pressure drop. In this work, however, we find that even for processes with constant injection rates, N_{c2} is a more appropriate form to represent the ratio of viscous forces to capillary forces. The Bond numbers B and N_B are related by the correlation of the permeability (k) and the grain sizes (R) of a medium.

There are two CDC's for a displacement system, depending on the continuity of the displaced fluid [77, 91, 134, 135]. A discontinuous nonwetting phase is more difficult to displace from a medium than a continuous nonwetting phase [77, 91]. In this work, we focus our attention on the displacement of continuous nonwetting phase from a porous medium, which is commonly involved in oil recovery processes with an oil bank. CDC's are generally obtained from laboratory measurements [43, 74, 91, 119], although attempts have been made to predict CDC's by statistical [78, 134] or deterministic theories [77, 115, 135]. Studies of CDC's have been largely focused on the balance of capillary and viscous forces [77, 109, 115, 134], which is measured by the capillary number. Consequently, gravity effects are neglected in CDCs used in most simulators of enhanced oil recovery processes, even though some studies [91, 130, 131] have shown that gravity effects can be significant. In this work, we examine the combined effects of gravity and viscous forces on oil entrapment in porous media, and we define conditions under which gravity forces can be neglected or must be included in the analysis.

4.1.2 Entrapment mechanisms

In order to identify the factors that influence oil entrapment during immiscible displacements, we first review entrapment mechanisms. Mohanty *et al.* [87] investigated the physics of oil entrapment in water-wet media, and identified two entirely different entrapment mechanisms, namely, a snap-off process that traps oil in a pore and a by-pass process caused by competition of flows between pores. Using detailed experimental observations, Chatzis *et al.* [17] determined that approximately 80 percent of oil is entrapped by snap-off processes and 20 percent by the by-passing processes for consolidated, water-wet media.

Snap-off occurs in pores with large aspect ratios, the ratio of pore body and pore throat diameters. The large aspect ratio creates a significant lower wetting-phase pressure at the pore throat than that in the pore body. Hence, the wetting phase flows towards the pore throat, and forms a collar that grows and eventually breaks the nonwetting phase. Roof [109] derived a static criterion for snap-off in noncircular capillary tubes, based on the capillary force balance at the pore throat and the pore body. A noncircular capillary tube was used as a model of the irregularities of pores and the roughness of solid surface of the medium. Ransohoff *et al.* [106] extended Roof's static analysis to include the effects of viscous flow resistance in the water filled corners of the capillary tube. For a system shown in Fig. 4.1a, they obtained the static criterion for snap-off,

$$R_b \geq \frac{C_m R_o R_t}{R_o - R_t}, \tag{4.5}$$

where C_m is a dimensionless interfacial curvature, which is a function of the cross-sectional geometries, R_o is the pore neck radius, and R_t and R_b are the hydraulic radii of the pore throat and pore body respectively, as shown in Fig. 4.1A.

To include the dynamic effects of viscous flow, Ransohoff *et al.* [106] and Gauglitz *et al.* [44] calculated and experimentally measured the time required to transport enough fluid into the pore throat to have snap-off, and compared it to the time for the nonwetting phase to flow through the pore throat. If the time of transporting enough fluid to form a collar is less than the time required for the nonwetting phase to flow through the pore throat, snap-off would occur.

The random nature of the sizes and locations of pores in porous media incorporating the interconnections among the pores generates flow competitions among pores. The displacing fluid in the fast flow pores can trap oil in pores in which flows are slow. This mechanism is referred to as by-passing. Pore doublet models (PDM) have been used both theoretically [17, 77] and experimentally [17] to demonstrate the by-pass mechanism. The PDM is based on the assumption that well-developed-Poiseuille flows compete in two parallel flow paths (pores) with different sizes (see Fig. 4.1B). The flow velocity in each flow path can be obtained by combining Poiseuille's law and the Young-Laplace equation [77]. The ratio of the velocities is an indication of the amount of fluid trapped in one pore. For an imbibition process, capillary forces draw the displacing phase into the smaller pore, while viscous forces make the fluid flow more rapidly in the larger pore. The result of this competition is that at low injection rate, the oil in the large pore would be trapped, with the reverse being true at high rates. Chatzis and Dullien's experiments [17] on a model of neck-bulge-neck pores showed that oil was trapped by the by-passing process.

By-passing processes can also be represented by network models for studies of entrapment mechanisms in porous media [9, 39, 40, 41, 130, 135]. Network models represent porous media by networks of pores with different sizes and connectivities. Another approach, percolation theory, has also been used to represent the random nature of the porous media, in which the flow path is fully random. In its original form, percolation theory represented only two-phase displacements when capillary forces dominate the flow process, and it did not account for the continuity of the flow path. Invasion percolation theory was then introduced to include both the randomness of the medium and the continuity of the fluids. In the following subsection, we review briefly effects of

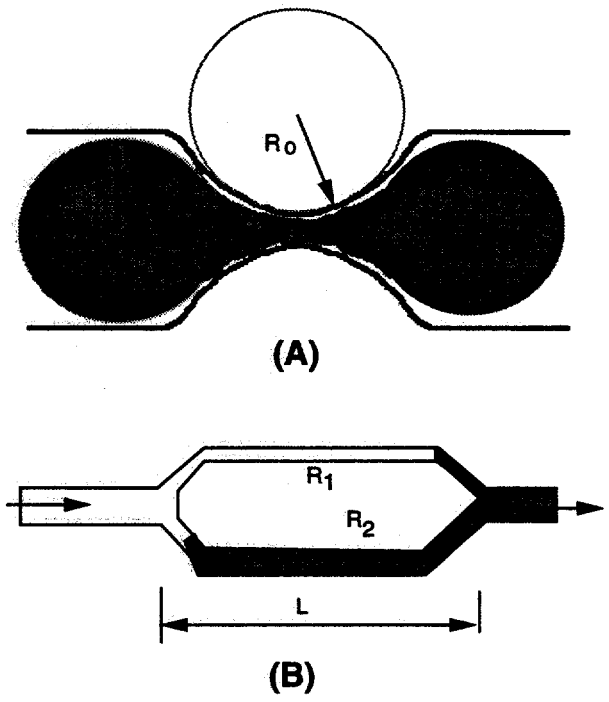

Figure 4.1: Commonly used snap-off model(A) and pore doublet model (B).

gravity in invasion percolation theory as well as the experimental results that demonstrate effects of gravity on residual nonwetting phase saturation.

Gravity Effects on Entrapment

The first theoretical investigation of gravity effects was reported by Wilkinson in an invasion percolation study [130]. Wilkinson neglected the snap-off process, and assumed that the nonwetting phase is only trapped by the by-passing process. Correlation lengths for both viscous and buoyancy forces were introduced to measure the relative magnitudes of viscous and buoyancy forces compared with capillary forces in the medium. A dimensionless viscous correlation length was defined as

$$\xi_V = \frac{L_{vm}}{R} \propto \left(\frac{N_{c1}}{k_w}\right)^{-\upsilon/(1+\upsilon)}, \tag{4.6}$$

where L_{vm} is the maximum length of oil clusters in the system during a viscous displacement, R is the grain size (radius) of the medium, $k_w = kk_{rw}/R^2$ and υ is a percolation exponent ($\upsilon = 0.88$ for three-dimensional percolation). They also defined a gravity correlation length (ξ_G),

$$\xi_G = \frac{L_{gm}}{R} \propto B^{-\upsilon/(1+\upsilon)}, \tag{4.7}$$

where B is the Bond number [91, 130], and L_{gm} is the maximum length of oil clusters in the system when gravity forces dominate. For gravity-dominated flow, the residual oil saturation S_{or} was related to the gravity correlation length by

$$S^*_{or} - S_{or} \propto \left(\frac{1}{\xi_G}\right)^{(1+\beta)/\upsilon} \propto B^{\lambda}, \tag{4.8}$$

where $\lambda = (1+\beta)/(1+\upsilon)$, which is a percolation constant ($\lambda = 0.77$ for three-dimensional percolation), β is also a percolation constant of 0.45 for three dimensional percolation, and S^*_{or} is the residual oil saturation at very low capillary number and Bond number. For viscous-dominated cases, the residual oil saturation was correlated as

$$S^*_{or} - S_{or} \propto \left(\frac{1}{\xi_V}\right)^{(1+\beta)/\upsilon} \propto \left(\frac{N_{c1}}{k_w}\right)^{\lambda}. \tag{4.9}$$

For situations in which both viscous and gravity forces act, Wilkinson [130] assumed that capillary and gravity forces were additive, and that the residual oil saturation depends on $(N_{c1}/k_w + B)^{\lambda}$.

Blunt *et al.*[9] developed a network model to calculate the percolation constant for invasion percolation processes. For both imbibition and drainage processes, Blunt *et al.* showed good agreement between network simulations and percolation theory when the processes were dominated by gravity forces. They also demonstrated numerically that gravity forces (represented by the Bond number B) behave the same as viscous forces (N_{c2}). For cases in which both gravity and viscous forces are involved, Blunt *et al.* proposed an effective correlation length to correlate the residual oil saturation. The effective correlation length is defined as

$$\frac{1}{\xi} = \frac{1}{L} + \frac{1}{\xi_V} + \frac{1}{\xi_G}, \tag{4.10}$$

where L is the length of the system. For a porous medium of relatively large size, $1/L \approx 0$, and hence

$$\frac{1}{\xi} \approx \frac{1}{\xi_V} + \frac{1}{\xi_G}. \tag{4.11}$$

In terms of capillary and Bond numbers, the residual nonwetting phase saturation is

$$S^*_{or} - S_{or} \propto \left((Bk_{rw})^{\upsilon/(1+\upsilon)} + N_c^{\upsilon/(1+\upsilon)}\right)^{(1+\upsilon)/\upsilon}. \tag{4.12}$$

Eq. 4.12 indicates that the effective correlation length theory does not give a linear combination. Thus, for cases in which both gravity and viscous forces act, there are two very different correlations for residual oil saturations. We shall note that these correlations are two extrapolations of the invasion percolation theory, not from rigorous derivations. The pore-level models described in the next section support the linear combination of gravity and viscous forces in determining residual oil saturations.

Experimental studies [91, 92] indicate substantial effects of gravity on residual nonwetting phase saturation in glass-bead packs. The experiments were performed with beads of different diameters to obtain a wide variation of Bond numbers. Morrow *et al.* [92] correlated their results against a linear combination of N_{c1} and B,

$$S_{or} = f(N_{c1} + 0.001413B). \tag{4.13}$$

This correlation agrees with Wilkinson's results, although Wilkinson's theory neglected the snap-off process. In the following section, we demonstrate theoretically that there is a linear combination of gravity and viscous forces for both snap-off and by-passing processes.

4.1.3 Extended REV-Scale Models

Previously available models of snap-off and by-passing neglect the influence of gravity. In this section we extend such models to include gravity. In the following derivation of equations, we assume that the interface between oil and water phases is always in equilibrium, so that we can use the Young-Laplace equation to represent the pressure difference across an interface. Flow of both phases is assumed to be well-developed Poiseuille flow, and therefore, Poiseuille's law or Darcy's law is used to represent viscous pressure drops.

Snap-off Model

In past studies of snap-off processes, oil blob sizes were assumed to be smaller than the pore size. That assumption is known to be violated in displacements in real porous media. For example, Chatzis [17] observed the blobs could be several pore sizes in extent. In our analysis, we consider an oil blob occupying two pores in the vertical direction (see Fig. 4.2a). However, the analysis is not limited to two-pore lengths and could be easily extended to multipore arrangements. Consider the situation shown in Fig. 4.2, in which water flows into the pore from the bottom. We assume that water phase wets the walls with a film whose thickness remains constant in the pore body but varies in the pore neck. The pressures in the phases at the pore throat (A) are

$$P_o = P_i + \frac{C_m \sigma}{R_b} - \Delta P_{ov} - \rho_o g L, \tag{4.14}$$

and

$$P_w = P_i - \Delta P_{wv} - \rho_w g L, \tag{4.15}$$

where P_i is the pressure of the wetting phase at location (B), R_b is the pore body radius, C_m is the dimensionless interfacial curvature in the pore body and ΔP_{ov} and ΔP_{wv} are the viscous pressure drops of the oil and the wetting phase. Because of the continuity of the wetting phase, the wetting phase can reach the pore throat through other neighboring pores. Therefore, we use Darcy's law to calculate the viscous pressure drops for both phases. ΔP_{ov} and ΔP_{wv} are then expressed as $\Delta P_{wv} = (\mu_w v_w L)/(k k_{rw})$, and $\Delta P_{ov} = (\mu_o v_o L)/(k k_{ro})$. Thus, the pressure difference between the two phases at the pore throat (A) is

$$\Delta P_1 = (P_o - P_w)_1 = \frac{C_m \sigma}{R_b} + (\rho_w - \rho_o) g L + \frac{\mu_w v_w L}{k k_{rw}} - \frac{\mu_o v_o L}{k k_{ro}}. \tag{4.16}$$

At the pore throat, we can also obtain the pressure difference between the two phases from the Young-Laplace equation,

$$\Delta P_2 = (P_o - P_w)_2 = \frac{\sigma}{R_t} - \frac{\sigma}{R_o}, \tag{4.17}$$

where R_t is the oil throat radius, and R_o is the radius of the oil neck (see Fig. 4.2b).

Now we consider the following situations: $\Delta P_2 > \Delta P_1$ and $\Delta P_2 < \Delta P_1$. When $\Delta P_2 > \Delta P_1$, the fluids would flow in such a way as to reduce ΔP_2 to keep the two forces in balance. In order to decrease ΔP_2, the system would either increase R_t or decrease R_o. It is impossible to increase R_t much further, because of the solid pore structure. Thus, the system would reduce R_o. To reduce the value of R_o, capillary forces pump the wetting phase into the pore throat. Consequently, a wetting phase collar ring would forms at the pore throat [106]. The formation of the collar ring reduces the value of R_t, and results in snap-off. However, when $\Delta P_2 < \Delta P_1$, the system becomes stable. In order to balance the pressure difference in this case, the system would either reduce R_t or increase R_o. Reducing R_t is impossible, because the viscous pressure difference ΔP_1 would push oil into the pore throat and the interface moves outward to increase R_t. Thus, increasing the effective value of R_o is the only solution. To increase the effective value of R_o, the capillary forces push the wetting phase away from the pore throat and there is a reduced wetting phase at the pore throat. Therefore, there would be no snap-off. In summary, we argue that snap-off would occur if $\Delta P_2 \geq \Delta P_1$. We then obtain the following condition for snap-off tp occur,

$$\frac{\sigma}{R_t} - \frac{\sigma}{R_o} \geq \frac{C_m \sigma}{R_b} + (\rho_w - \rho_o) g L + \frac{\mu_w v_w L}{k k_{rw}} - \frac{\mu_o v_o L}{k k_{ro}}. \tag{4.18}$$

Because v_o has positive values, the condition simplifies

$$\frac{\sigma}{R_t} - \frac{\sigma}{R_o} \geq \frac{C_m \sigma}{R_b} + (\rho_w - \rho_o) g L + \frac{\mu_w v_w L}{k k_{rw}}, \tag{4.19}$$

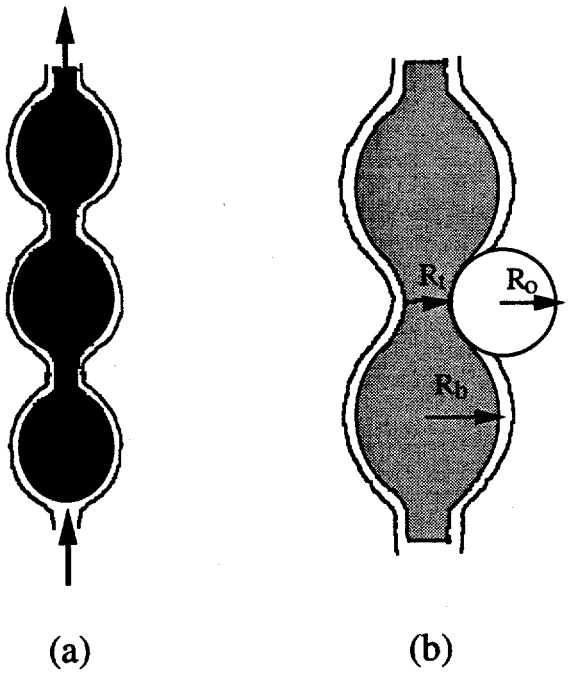

Figure 4.2: Vertically oriented snap-off model (a) and detailed pore structure (b).

or

$$N_{c1} + k_{rw}B \leq \frac{k}{R_t L} k_{rw} \left(1 - \frac{R_t}{R_o} - \frac{C_m R_t}{R_b}\right). \tag{4.20}$$

Eq. 4.20 suggests that mobility ratio would have minimal effect on the final residual nonwetting phase saturation, which agrees with experimental observations [2, 119].

If we set $N_{c1} = 0$ and $N_B = 0$, Eq. 4.20 simplifies to

$$R_b \geq \frac{C_m R_t R_o}{R_o - R_t}, \tag{4.21}$$

which is the same as Eq. 4.5.

Doublet Model

For vertically oriented doublet pores as Fig. 4.3 shows, we write down the pressure drops from point B to point A for each pore as following for a upflow (on the assumption that the tubes are cylindrical)

$$\Delta p_1 = \frac{8\mu_w v_1 L_1}{R_1^2} + \frac{8\mu_o v_1 (L - L_1)}{R_1^2} - \frac{2\sigma}{R_1} + L_1 \rho_w g + (L - L_1)\rho_o g, \tag{4.22}$$

and

$$\Delta p_2 = \frac{8\mu_w v_2 L_2}{R_2^2} + \frac{8\mu_o v_2 (L - L_2)}{R_2^2} - \frac{2\sigma}{R_2} + L_2 \rho_w g + (L - L_2)\rho_o g, \tag{4.23}$$

where R_i is the radius of tube i, and L_i is the distance the displacing fluid flows in tube i, L is the length of the tubes, and v_i is the flow velocity in tube i. Since the two pores have common junctions,

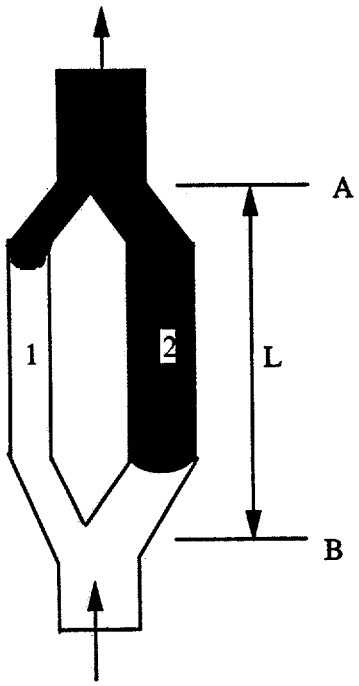

Figure 4.3: Vertically oriented pore doublet mode

the pressure drops Δp_1 and Δp_2 must be equal, $\Delta p_1 = \Delta p_2$. Therefore, we obtain the following expression in which the average velocity (v_a) of the doublet pores is $v_a = (R_1^2 v_1 + R_2^2 v_2)/(R_1^2 + R_2^2)$.

$$N_c m + (l_1 - l_2)\frac{f}{1+f} N_B = \frac{2k}{R_1 L}\frac{f}{1+f}(1 - \frac{R_1}{R_2}), \tag{4.24}$$

where $l_i = L_i/L$, $\mu_r = \mu_o/\mu_w$, $f = R_2^2/R_1^2$, and

$$m = (1-\mu_r)\left((1 + f - \frac{v_2}{v_a} f) l_1 f - \frac{v_2}{v_a} l_2\right) + \mu_r \left(f(1 + f - \frac{v_2}{v_a}) - \frac{v_2}{v_a}\right). \tag{4.25}$$

The permeability of the PDM is defined as $(R_1^2 + R_2^2)/8$ from Poiseuille's law.

To simplify the arguments, we assume the radius of pore 1 is smaller than that of pore 2, $R_1 < R_2$. Capillary forces draw the wetting phase into the smaller pore (pore 1), and viscous forces make fluid flow more easily in the larger pore (pore 2). At the same time, gravity forces reduce the velocity difference between pores. Reduction of viscous forces slows the flow in the larger pore, and results in more oil trapped in the larger pore. If the oil in pore 2 were completely trapped, we would have the following parameters: $v_2 = 0$, $l_1 = 1$ and $l_2 = 0$, and $m = f(1 + f)$. Because the value of m decreases with increasing value of v_2, the system must have a value of m smaller that $f(1 + f)$ to avoid entrapment of the nonwetting phase in pore 2 completely. Thus, the nonwetting phase would be trapped in pore 2 completely, if $m \geq f(1 + f)$. Rearrangement of Eq. 4.24 gives

$$N_{c1} + C N_B \leq C \frac{2k}{R_1 L}(1 - \frac{R_1}{R_2}), \tag{4.26}$$

where $C = 1/(1 + f)^2$.

For a given system, Eq. 4.26 indicates that the nonwetting phase in the larger pore would be trapped due to by-passing when the combined effects of gravity and capillary forces are less

than a certain value. The relative magnitude of gravity forces and viscous forces depends on the value of C, which represents the heterogeneity of the system. $C = R_1^4/(R_1^2 + R_2^2)^2$ is the relative permeability of the displacing phase (the wetting phase), and can be derived as following with an assumption that displacements in the tubes are piston-like,

$$C = \frac{R^4}{(R_1^2 + R_2^2)^2} = \frac{k_1 R_1^2}{k(R_1^2 + R_2^2)} = \frac{Q_1}{Q_t}, \tag{4.27}$$

where k_1 and k are the permeabilities of tube 1 and both tubes, Q_1 and Q_t are the flow rate in pore 1 and the total flow rate in both pores. According to Darcy's law, $Q_1 = Ak_{rw}k/(\mu\partial\Phi/\partial l)$, and $Q_t = Ak/(\mu\partial\Phi/\partial l)$ for a given flow area A and potential gradient $\partial\Phi/\partial l$. Therefore,

$$C = \frac{Q_1}{Q_t} = \frac{\frac{Akk_{rw}}{\mu}\frac{\partial\Phi}{\partial l}}{\frac{Ak}{\mu}\frac{\partial\Phi}{\partial l}} = k_{rw}, \tag{4.28}$$

and

$$N_{c1} + k_{rw}N_B \leq k_{rw}\frac{2k}{R_1 L}(1 - \frac{R_1}{R_2}). \tag{4.29}$$

Thus, Eq. 4.29 also suggests that a linear combination of the capillary and Bond numbers can be used to state a criterion for by-passing. Here again, the coefficient of the Bond number is the wetting-phase relative permeability.

Summary

In both snap-off and doublet models, we obtain criteria for entrapment of the nonwetting phase in porous media in terms of linear combinations of capillary and Bond numbers. Comparison of Eqs. 4.20 and 4.29 indicates that they have similar forms. In both cases, the relative contributions of capillary and Bond numbers are determined by the relative permeability of the displacing phase. Using the relationship between N_{c1} and N_{c2}, we obtain the following equations for snap-off and by-pass processes.

$$N_{c2} + N_B \leq \frac{k}{R_t L}(1 - \frac{R_t}{R_o} - \frac{2R_t}{R_b}), \tag{4.30}$$

and

$$N_{c2} + N_B \leq \frac{2k}{R_1 L}(1 - \frac{R_1}{R_2}). \tag{4.31}$$

The simplicity of Eqs. 4.30 and 4.31 suggests that N_{c2} is a more appropriate definition of capillary number than N_{c1} even for processes with constant injection rates.

4.1.4 Experiments

Experimental studies [91, 92] provide some evidence that a linear combination of capillary number and Bond number determines residual oil saturation. However, the Bond numbers were changed by varying the sizes of the beads used in packing their columns. We now investigate whether use of the linear combination is reasonable if we change Bond number by the variation of IFT and density differences of the fluids. In this section, we report results from experiments designed to examine these parameters.

All displacements were conducted in the same sand-pack column. The Bond number was varied by using different IFT's and density differences of the fluids. Fig. 4.4 is a schematic of the experimental apparatus. The HPLC pump provided constant injection rates ranging from 0.1 to 8.0 cc/min. The length of the sand-packed porous medium was 119.0 cm and the diameter 1.95 cm. The permeability was 48.5 Darcy and the porosity, 0.256. We used pre-equilibrated mixtures

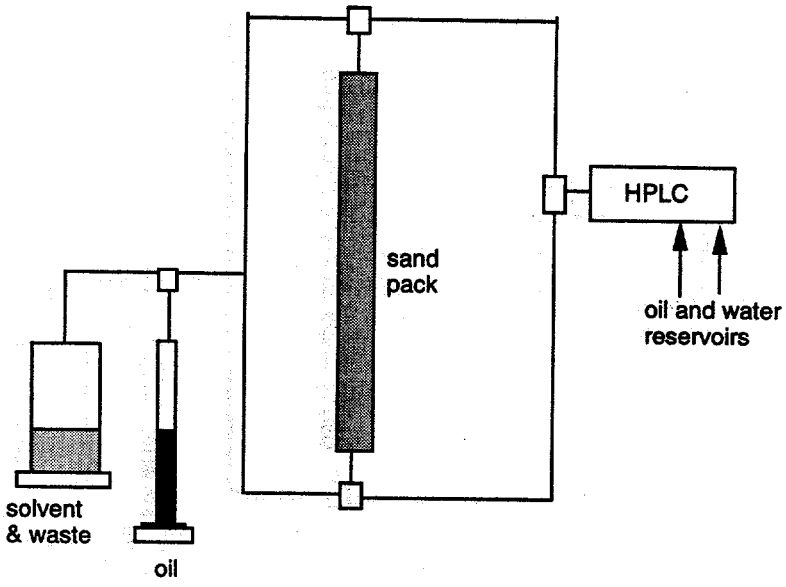

Figure 4.4: A schematic diagram of the experimental setup.

of brine, iso-octane (iC_8) and isopropanol (IPA) to generate fluid pairs of wide range of IFT and densities differences, This system has been well studied [92]. Four tie-lines were used to obtain IFTs varying from 0.1 to 38.1 mN/m and densities from 0.11 to 0.33 g/cc, which correspond to a range of capillary and Bond numbers from 10^{-6} to 10^{-3}. Table 4.1 lists the measured properties of the fluids used.

All the imbibition displacements were conducted with initial wetting phase saturations. These were established by first injecting the nonwetting phase into the top of the column that was fully saturated with the wetting phase. The initial wetting phase saturation varied from 0.19 to 0.26 of pore volume. The large variation of initial wetting phase saturations were results of large variations in mobility ratios in different runs. In this range of initial wetting phase saturation, repeated experiments showed that this variation of initial wetting phase saturation did not influence the residual nonwetting phase saturation. Therefore, the differences in the residual nonwetting phase saturation are the results of the capillary and Bond number variations. To study the directional effects of gravity forces, we conducted displacements by injecting the wetting phase from either bottom or top of the column. We refer to displacement from the bottom as gravity-favorable and that from the top as gravity-unfavorable, because the gravity forces stabilize the displacements

fluid system	IFT (mN/m)	$\Delta\rho$ kg/m^3	N_B	Viscosity (cp) (wetting)	Viscosity (cp) (nonwetting)
#1	38.1	330	4.2×10^{-6}	0.98	0.48
#2	4.41	305	3.3×10^{-5}	2.80	0.49
#3	1.07	220	1.0×10^{-4}	3.25	0.52
#4	0.10	110	5.2×10^{-4}	2.60	0.70

Table 4.1: Properties of the fluids used in this work

fluid system	flow rate (cc/min.)	S_{iw} favorable	S_{or} favorable	S_{iw} unfavorable	S_{or} unfavorable	N_{c1}
#1	0.5	0.19	0.181			6.6×10^{-7}
#1	1.0			0.22	0.257	1.4×10^{-7}
#1	2.0	0.23	0.181	0.19	0.248	2.7×10^{-6}
#1	4.0	0.23	0.181	0.19	0.248	5.4×10^{-6}
#1	8.0	0.20	0.171	0.24	0.19	1.1×10^{-5}
#2	0.1	0.24	0.16			3.4×10^{-5}
#2	0.5	0.25	0.152			1.6×10^{-5}
#2	1.0			0.26	0.19	3.3×10^{-5}
#2	2.0	0.26	0.138	0.27	0.15	6.7×10^{-5}
#2	4.0	0.24	0.124	0.22	0.123	1.3×10^{-4}
#2	8.0	0.25	0.10	0.27	0.11	2.7×10^{-4}
#3	0.1	0.25	0.12			1.6×10^{-5}
#3	0.5	0.25	0.11	0.24	0.178	8.5×10^{-5}
#3	1.0			0.25	0.14	1.7×10^{-4}
#3	2.0	0.24	0.10	0.22	0.11	3.2×10^{-4}
#3	4.0	0.20	0.086	0.14	0.09	6.2×10^{-4}
#3	8.0	0.22	0.067	0.23	0.07	1.3×10^{-3}
#4	0.1	0.23	0.096			1.4×10^{-4}
#4	0.5	0.25	0.08			6.9×10^{-4}
#4	1.0	0.25	0.067			1.4×10^{-3}
#4	2.0	0.23	0.048			2.8×10^{-3}
#4	4.0	0.23	0.038			5.5×10^{-3}
#4	8.0	0.25	0.02			1.0×10^{-2}

Table 4.2: Summary of the displacement results

when injected phase enters the column from the bottom. Table 4.2 summarizes the experimental results from both gravity-favorable and unfavorable displacements.

In all the displacements, we observed little additional recovery shortly after breakthrough, an observation that is consistent with the idea that the sand-pack was strongly-water wet. Following the common practice, we plot the final residual oil saturation against the capillary number alone for all displacements in Fig. 4.5. Apparently, the experimental data cannot be reasonably correlated by the capillary number alone. The experimental results also indicate, therefore, that gravity forces and the flow directions affect the residual nonwetting phase saturations.

Discussion

In the definitions of capillary number (N_{c1}) and Bond number N_B, five variables are involved: the injection rates (v), the IFT (σ), the density difference ($\Delta\rho$), the viscosity of the wetting phase (μ_w), and the permeability of the medium (kk_{rw}). In the experiments described in the previous section, we varied IFT and density differences, and injection rates to obtain a wide range of capillary and Bond numbers. To check the other parameters, we review the experimental results of Morrow and Songkran[91] and Morrow *et al.*[92]. In both studies, they varied the capillary number and Bond number by changing different bead sizes and injection rates. Changing bead size changes the permeability of the bead pack. The permeability of a beadpack can be related to the bead size

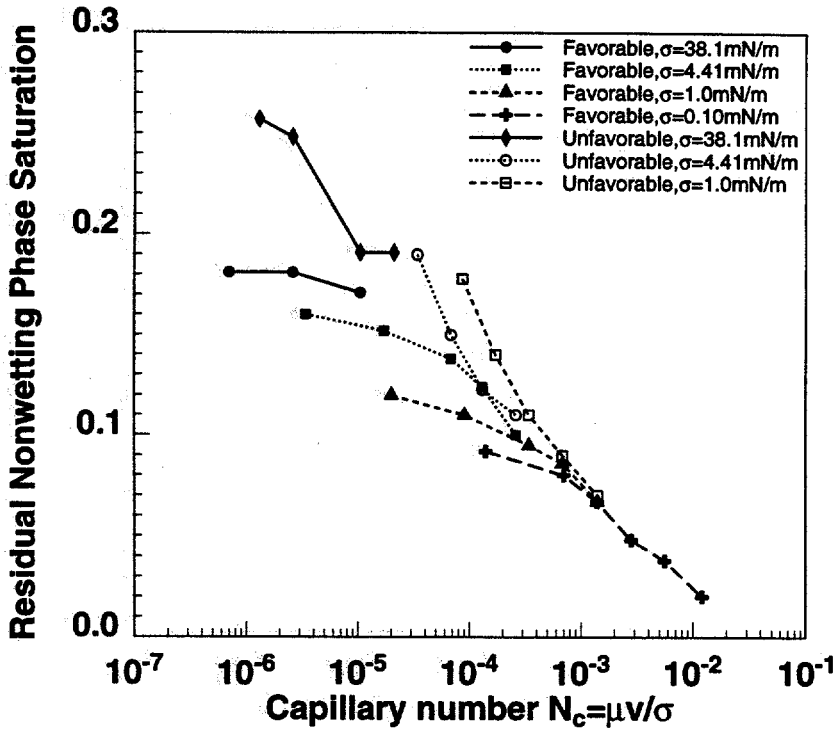

Figure 4.5: The Correlations of residual nonwetting phase saturation with the capillary number alone for all displacements.

through the Kozeny-Carman equation

$$k = \frac{\phi^3}{k_z(1-\phi)^2 A_s^2}, \tag{4.32}$$

where A_s is the specific surface area per unit solid volume, for spherical bead $A_s = 3/R$, K_z is the Kozeny constant, which is approximately equal to 5 for bead packings, and ϕ is the porosity of the packing, which is about 0.38 for bead packings. Therefore, the permeability of a bead pack can be simply related to bead size as

$$k = 0.00317R^2. \tag{4.33}$$

Thus, the correlation given by Morrow and Songkran [91] and by Morrow *et al.* [92] can rearranged in terms of N_B as

$$S_{or} = f(N_{c1} + 0.445N_B). \tag{4.34}$$

Comparison of Eq. 4.34 with our theory indicates that the wetting-phase relative permeability at the trailing edge of the displacement front is about 0.445, which is consistent with the reported measurements for a mimilar system [91, 92] ($k_{rw} = 0.5$).

We used a procedure similar to that used by Morrow and Sougkran [91], and obtained a least-squares fit of our residual oil saturations from gravity-favorable displacements with an effective number defined as $N_e = N_{c1} + cN_B$. As Fig. 4.6 shows, a straight-line correlation on the semi-log plot exists when $c = 0.5$. The value of c is the relative permeability of the wetting phase according to Eqs. 4.20 and 4.29. This value is very close to the measured relative permeability by Morrow and Songkran [91] on a similar system. Again, our experiments suggest that a linear combination of the capillary and the Bond numbers correlates the residual oil saturations, and the appropriate coefficient is the wetting-phase relative permeability.

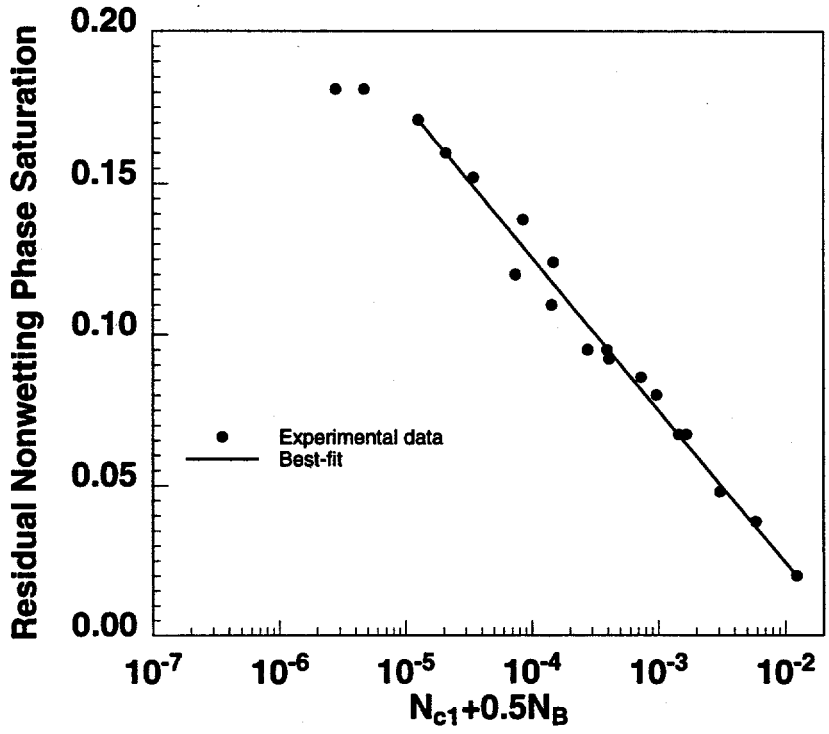

Figure 4.6: Correlation of the residual oil saturations and the sum of the capillary and Bond numbers for gravity-favorable displacements.

Using the same value of c, we correlated all our experimental results, as Fig. 4.7 shows, for both gravity-favorable and gravity-unfavorable displacements. At high values of N_e, the correlation is excellent, while it is less satisfactory when N_e is small. The difference between the gravity-favorable and unfavorable displacements may result partly from the accuracy of the flow rate and permeability measurements, because the subtraction of the two numbers enhanced the significance of the measurement error when these two values are comparable. In general, the correlation is good and we obtain the following correlation of the residual oil saturation with the capillary and the Bond numbers.

$$S_{or} = 0.02 + 0.0505 log(\frac{0.01227}{N_{c1} + 0.5N_B}). \tag{4.35}$$

Fig. 4.8 shows a comparison of the experimental data and the correlation given by Eq. 4.35. Fig. 4.8 also demonstrates the significant directional effects of gravity forces on residual nonwetting phase saturations. For a system with gravity forces comparable with viscous forces, gravity-favorable displacements have much lower residual oil saturation than do gravity-unfavorable displacements. This directional effect of gravity forces on residual oil saturation shows that gravity forces can reduce the residual oil saturations, as well as macroscopic sweep efficiency [136].

For a given system, it would be useful to determine which forces are most important. Therefore, we rearrange the linear combination to obtain

$$N_e = N_{c2}(1 + \frac{\Delta\rho g k}{\mu_w v}). \tag{4.36}$$

The relative magnitudes of N_{c2} and N_B in a system can be reflected by the gravity number

$$N_g = \frac{\Delta\rho g k}{\mu_w v}. \tag{4.37}$$

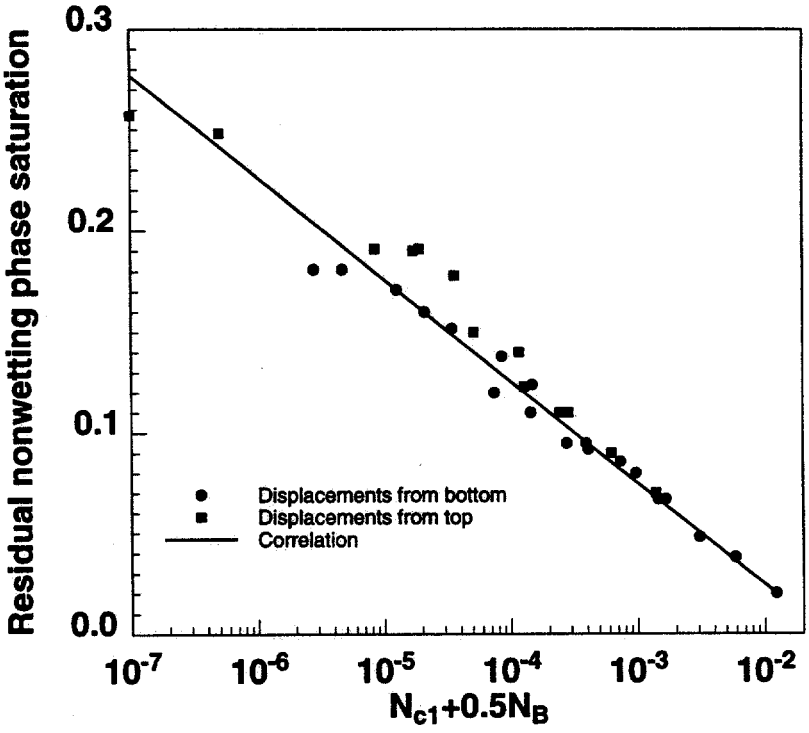

Figure 4.7: Correlations of Residual oil saturations and the sum of capillary and Bond numbers from percolation theory and best-fit of the experimental data.

When $N_g > 1$, the Bond number is the dominating factor, whereas when $N_g < 1$, capillary number is the controlling parameter in determining the residual oil saturation.

We should note that the gravity number (N_g) is proportional to the medium permeability. Thus, flow in a high-permeability medium will have larger gravity effects than that in a low-permeability medium. To illustrate this concept, let us compare typical oil-spill and oil recovery situations. The permeability of a typical soil is about 50 darcy, water viscosity is around $10^{-3} N*s$ (1 cp), and the flow rate can be estimated to be 1 ft/day, which is about 3.5 x $10^{-6} m/s$. We also assume that the density difference is about $300 kg/m^3$ and the IFT is about 40 x $10^{-3} N/m$. The gravity number (N_g) is about 2.5, that is, the gravity forces are larger than the viscous forces in typical spilled-oil clean-up processes. For a waterflood oil recovery process, however, with a permeability of the order of 100 md and the same fluid properties, the gravity number is about 5×10^{-3}. Thus, the effects of density difference and flow direction will be more important in oil-spill applications than in typical waterflood situations.

Conclusions

In this work, we presented two different models of oil entrapment mechanisms, and experimental results from oil displacements with gravity forces assisting and impeding the oil recovery processes. We draw the following conclusions:

1. We demonstrated theoretically and experimentally that a linear combination of gravity and viscous forces can be used to correlate residual nonwetting phase saturations for both gravity-favorable and gravity-unfavorable displacements.

2. Changing the value of capillary and Bond numbers by varying interfacial tension, density difference and injection rate give similar effects on residual nonwetting phase saturations in our

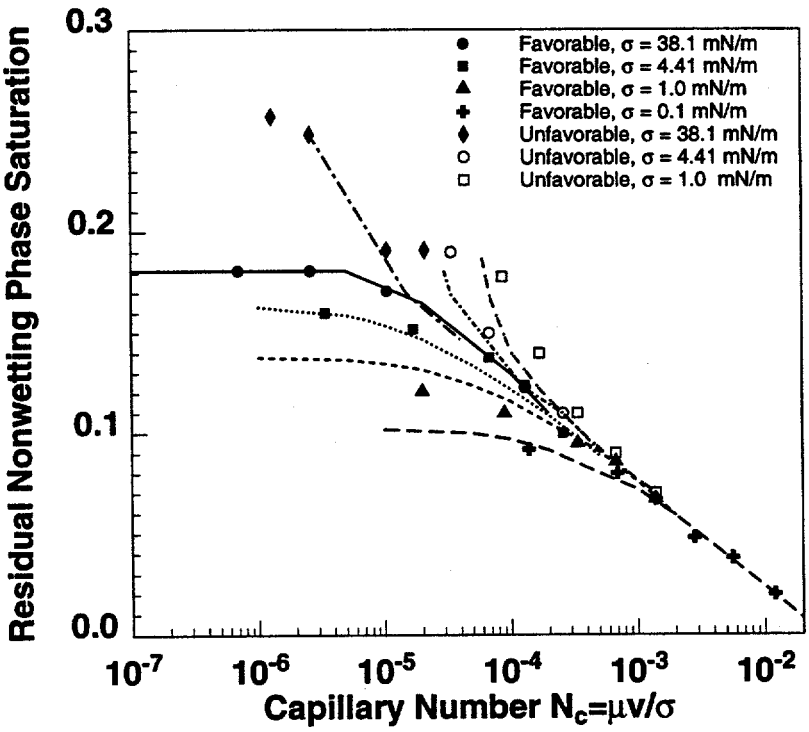

Figure 4.8: Comparison of the correlation with experimental data (lines are correlations and dots are the experimental data).

experiments.

3. When gravity forces are comparable to or larger than the viscous forces, gravity-unfavorable displacements have significantly higher residual nonwetting phase saturation than gravity-favorable displacements.

4. Because soils have much higher permeabilities than oil reservoirs, gravity effects on residual nonwetting phase saturations are much more significant in spilled-oil clean-up than in oil recovery processes.

4.2 Three Phase Flow and Gravity Drainage in Porous Media

Dengen Zhou and Martin Blunt

4.2.1 Introduction

The displacement of oil by gas in the presence of water is an important recovery process in gas injection processes and similar ideas apply in the cleanup of contaminants spilled below ground. The displacement of oil by gas under gravity (gravity drainage) occurs in oil reservoirs when the gas cap expands as the pressure drops, when oil condensate forms, or when gas is injected into the gas cap. Three phase flow is also seen when natural gas, nitrogen, carbon dioxide or steam are injected into the field to displace oil. In an environmental context, the spilling and leakage of hydrocarbons and organic solvents can be significant contributors to groundwater contamination. The low solubility of these products means that they are often present in their own phase. An oil that is less dense than water, such as a fuel, will migrate downwards until it rests above the water table. The effects of water table movement, capillarity and gravity will smear the oil in

a region above and below the water table, where both air and water are also present. Artificial lowering of the water table by pumping results in the displacement of oil by air through a wet soil. This again is a gravity drainage process. Since the work of Dumore and Schols [35] , it has been known that gravity drainage in water-wet rock can lead to a high oil recovery, with residual oil saturations of a few percent in the presence of immiscible gas and water, which is much lower than the residual oil saturation in the presence of water alone. Further studies on sandstone cores, bead packs and sand columns [18, 71, 127] confirmed these results. It was suspected that the high oil recovery was due to drainage through films of oil that lie between the water and the gas in the pore space. This film drainage has been observed directly in two dimensional etched glass micromodels by Kantzas et al. [72], Oren et al. [97], Oren and Pinczewski [96], Kalaydjian [69] and Soll et al. [113]. It was shown by Oren et al. [97], Vizika [127] and Kalaydjian [70] that systems with a positive spreading coefficient, which means that the oil spontaneously spreads over a water/gas interface, would experience film drainage and high recoveries, whereas nonspreading systems would see lower recoveries. It was suggested by Kantzas et al. [72] that the recovery could be determined by the stability of the oil film, which is controlled by capillary and intermolecular forces, rather than the spreading coefficient alone. In this work, we investigate the fundamental mechanisms of oil recovery in three phase flow, in water-wet porous media, starting at the molecular scale, and provides a predictive theory of gravity drainage. The principal issues are: (1) the thickness and stability of thin oil films controlled by intermolecular forces; (2) the thickness of oil layers during drainage; (3) the flow rate in these layers; (4) the final oil recovery and fluid distribution. We will show that for a spreading system (typical of most fluids in polluted soil and oil reservoirs), the oil layer provides pressure continuity for the oil phase, thus preventing it from being trapped. Oil can drain rapidly by swelling these layers to occupy the crevices and roughness in the pore space. However, the final oil saturation can be essentially zero, with the oil confined to thin, molecular films. In vertical capillary/gravity equilibrium, where the oil density is less than that of water, there is a finite height above the water table (or the water/oil contact) where the connected oil saturation is zero. This height is determined solely by the height of the oil bank, and the surface tensions and densities of the fluids, but is independent of the pore size distribution. Non-spreading systems do not allow drainage of oil layers and give lower recoveries from gravity drainage. These findings are confirmed by a series of experiments on sand columns and capillary tubes.

4.2.2 Does Oil Spread on Water?

With three phases present in a porous medium, it is possible for oil to spread between water and gas in the pore space. This phenomenon is determined by the spreading coefficient C_s

$$C_s = \gamma_{gw} - \gamma_{go} - \gamma_{ow}, \tag{4.38}$$

where γ_{gw}, γ_{go} and γ_{ow} are the gas/water, gas/oil and oil/water surface tensions respectively measured on the fluids before they are brought into contact with each other. If $C_s > 0$, the contact line between the three phases is unstable and the oil spreads, as Fig. 4.9 illustrates. Most solvents, hydrocarbons and crude oils (see p. 104, Table 5 of [93]) do have a positive spreading coefficient.

In this work we will distinguish between an oil film, a few nanometers across, and an oil layer which may occupy crevices in the pore space and be microns thick. On a flat substrate, the oil eventually forms a film of approximately molecular thickness, between 0.5 and 5 nm across. This behavior is consistent with everyday experience: gasoline spilled on a puddle of water, for instance, will spread until it forms a thin, iridescent film on the water that is only of order a molecular diameter across. The water/gas interface containing this oil film has a much lowered effective surface tension for which, if there is no pressure difference across the film, the effective spreading coefficient is zero or negative [3, 46, 110]. The thickness of an oil film can be predicted by calculating

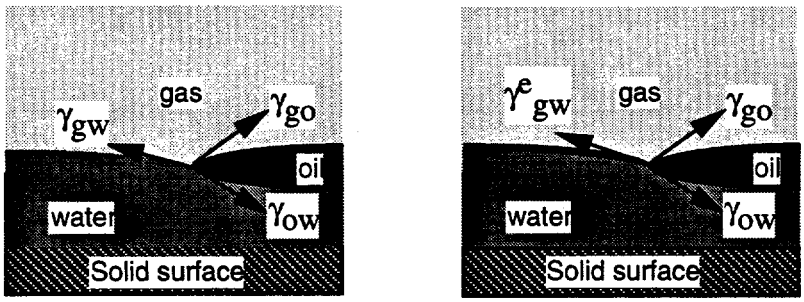

Figure 4.9: Distributions of three fluids in contact.

the van der Waals forces between the water, oil and gas. Our computation of the film thickness is similar to the work of Oren and Pinczewski [95], although we use the complete expression for the van der Waals force [?]. We have shown [11] that on a flat surface most hydrocarbons form a film, whose thickness depends on the capillary pressure and displacement history. The same behavior has been predicted for wetting films [57]. The film provides pressure continuity for the oil phase. This means that isolated oil ganglia, trapped and surrounded by water, can become connected during gas injection, when the gas contacts the oil. However, we will show that the drainage rate through these films is far too slow to account for the oil recoveries observed experimentally. Thicker oil layers in crevices of the pore space must provide channels for more rapid drainage. The calculation of film thickness using van der Waals forces is presented in Section 4.3.

4.2.3 Configuration of Three Phases in the Pore Space

Oil films in a cylinder

Fig. 4.10 shows the schematic arrangement of fluid in a cylindrical concavity of the pore space. Water wets the solid. Oil is intermediate-wet and occupies a film of thickness t, while the gas, being nonwetting, fills the center of the cylinder. The equilibrium film thickness is found from the augmented Young-Laplace equation

$$P_{cgo} = \Pi_o(t) + \frac{\gamma_{go}}{r - t - w} = \Pi_o(t) + \frac{\gamma_{go}}{r_{go}}, \tag{4.39}$$

where P_{cgo} is the gas/oil capillary pressure, w is the water film thickness, r_{go} is the radius of curvature of the gas/oil interface and $\Pi_o(t)$ is the disjoining pressure that accounts for the influence of intermolecular forces on the oil [27]. A positive disjoining pressure is equivalent to a repulsion between the gas and the water, leading to swelling of the oil film, whereas $\Pi_o(t) < 0$ corresponds to an attractive force that makes the film thinner. At distances greater than a few molecular diameters, the main contribution to the disjoining pressure comes from the dispersive, van der Waals force, which gives a small positive $\Pi_o(t)$ for t greater than approximately 10 nm for most alkanes. For t less than around 10 nm, the intermolecular forces are controlled by steric forces, can be very large and are significant compared with the curvature term in Eq. 4.39. A similar expression can be written for the pressure difference between the oil and water phases

$$\Pi_{cow} = \Pi_w(w) + \frac{\gamma_{ow}}{r_{ow}}, \tag{4.40}$$

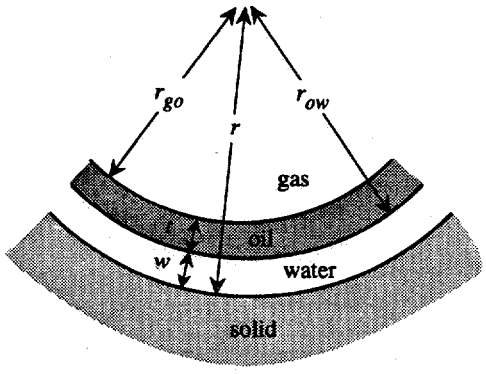

Figure 4.10: Distribution of three fluids in a cylindrical region of the pore space.

where $\Pi_w(w)$ is the disjoining pressure of the water film. Fig. 4.11 shows $\Pi_o(t) + \gamma_{go}/r_{go}$ plotted as a function of t for an n-octane/water/gas system with a representative water film thickness of 10 nm on a quartz capillary of radius 500 μm. The computation of $\Pi_o(t)$ is described in our previous work [?] and is accurate if $r_{go} >> t$. For t less than 10 nm, the intermolecular forces are most significant, whereas when t becomes close to $r - w$, the second term in Eq. 4.39 diverges. Stable solutions are found when both Eq. 4.39 is obeyed and $dP_{cgo}/dt < 0$. As indicated in Fig. 4.11, there is a narrow range of capillary pressures, just above γ_{go}/r_{go} , for which a film of thickness between 24 nm and 242 nm is stable, due to the long-range influence of van der Waals forces. At higher capillary pressures, the film collapses to molecular thickness. Such thin films are also observed on convex (protruding) surfaces. If we lower the capillary pressure below γ_{go}/r_{go}, there is no stable solution unless the oil occupies the whole of the cylindrical cross-section and there is no gas present. This spontaneous filling of a pore throat is similar to the snap-off mechanism, which has been described before [87, 109]. The maximum oil film thickness on a cylindrical concavity can be hundreds of nanometers. While this is much thicker than a molecular film, it is still more than three orders of magnitude smaller than the radius of curvature of the solid surface.

Oil layers in an angular crevice

Fig. 4.12 shows the distribution of oil, water and gas in a square crevice. From geometrical considerations, an oil layer is present if $r_{go} \geq r_{ow}$. From the augmented Young-Laplace Eqs. 4.39 and 4.40 this means that

$$\frac{P_{cow} - \Pi_w}{\gamma_{ow}} \geq \frac{P_{cgo} - \Pi_o}{\gamma_{go}}. \tag{4.41}$$

If we consider thick oil layers, with w and t taken to be 100 nm or more, the disjoining pressures will be negligible, in which case the inequality above reduces to

$$\frac{P_{cow}}{\gamma_{ow}} \geq \frac{P_{cgo}}{\gamma_{go}}. \tag{4.42}$$

If the oil/water pressure difference is much larger than the gas/oil pressure difference, it is possible for a thick oil layer to occupy most of the crevice. A large oil/water capillary pressure forces the water into the corner, while a relatively low gas/oil capillary pressure allows a thick oil layer to develop. This can be true for any angular or sharp groove in the pore space. Since pore sizes are typically in the range of 1 μm to 100 μm or more, oil layers several microns across can exist. If,

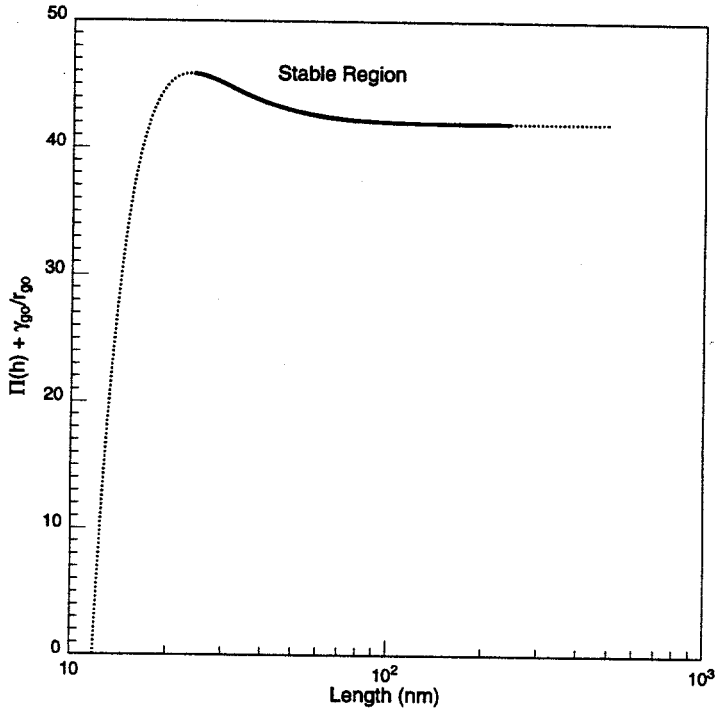

Figure 4.11: $\Pi_o(t) + \gamma_{go}/r_{go}$ computed as a function of oil film thickness, t, using the van der Waals intermolecular force.

however, the inequality (Eq. 4.42), is not obeyed, only a film of molecular thickness will be stable, where the disjoining pressures in Eq. 4.41 become significant.

To recap: on locally flat or convex portions of the pore space, the oil film thickness is a few nanometers; a cylindrical concavity, with a radius of several 100 microns, can support films tens to hundreds of nanometers across; whereas for sharp or angular crevices, layers several microns thick will form if the oil/water capillary pressure is much larger than the gas/oil capillary pressure. If the spreading coefficient is negative, a three phase contact line is stable, as shown in Fig. 4.9, and no oil films are seen.

4.2.4 Drainage Rates

Predicted rates

Fig. 4.13 shows the vertical arrangement of water, oil and air (gas) in a capillary tube. There are two oil ganglia separated by an air bubble of height h. If there is a film of oil that connects the two blobs, there will be pressure continuity in the oil phase which allows the upper ganglion to drain into the lower one under gravity. Since the air has a low density, the pressures in the two ganglia are approximately equal when drainage starts. The gas/oil interfaces at $z = 0$ and $z = h$ are assumed to be hemispherical caps of radius r, with a total curvature of $2/r$. Thus the gas/oil capillary pressure is approximately $2\gamma_{go}/r$. In a capillary tube of square cross-section, the fluid configuration is shown in Fig. 4.12. If $P_{cgo} = 2\gamma_{go}/r$, then the gas/oil radius of curvature, $r_{go} = r/2$. Water will also occupy the corner, but as we increase z, the oil/water capillary pressure will rise, forcing water further into the corner. Thus, for large values of h, the oil can occupy almost all the corner of the tube, resulting in rapid drainage. For smaller values of h, the water occupies more of the corners, and the drainage rate is lower. The calculation of drainage rates in capillaries of square and circular cross-section was reported in our previous work [133].

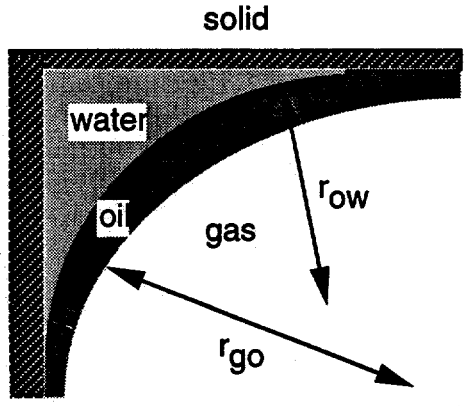

Figure 4.12: The arrangement of water, oil and gas in a square crevice.

Table 4.3: Fluid properties for the experiments presented

Experiments	γ_{ow}(mN/m)	$\rho_w - \rho_o$(kg/m^3)	ρ_o(kg/m^3)	μ_o(kg/(ms))	α
Mineral oil	54	157	833	0.005	8.9
Fig. 4.14	38.1	310	690	0.00048	4.03
Fig. 4.15	4.41	305	690	0.00049	0.47

Despite its simple geometry, the analysis for a cylindrical capillary is less straightforward. There is no obvious force balance on the oil film and the oil pressure is not easily determined. $P_{cgo} = 2\gamma_{go}/r$ implies a thin, molecular film and a negligible drainage rate. However, when the tube is held upright, gravity forces instantaneously lead to an increase in oil pressure. Moreover, small vibrations can perturb the pressure in the oil and gas phases. γ_{go}/r is only 42 Pa in the experiments we perform, compared with the atmospheric pressure of 10^5 Pa. To match the experimental results below, it appears that the oil pressure rises to make $P_{cgo} \approx \gamma_{go}/r$ and the oil film swells to reach its maximum stable thickness.

Experimental confirmation

We tested our predictions for the drainage times by performing a series of experiments with glass capillary tubes. We first filled the tube with water. Then oil was introduced into the tube at one end to form the lower oil blob. For runs without a lower oil ganglion ($h_2 = 0$) this step was omitted. Water was subsequently drained out of the opposite end to allow air to enter the tube. By controlling the amount of water that drained out, we controlled the height of the gas bubble, h. The last step was to allow some oil into the tube, above the gas. The tube was then placed vertically and we recorded the time for all the oil in the upper ganglion to drain. We conducted experiments for high (iso-octane and distilled water) and low (a mixture of iso-octane, water and iso-propanol partitioned into two phases) oil/water surface tensions. The fluid properties are shown in Table 1. For a capillary tube of circular cross-section with $r = 500$ μm, $h_2 = 0$ and $h = 2$ cm, it took three weeks to drain 0.8 mm^3 of iso-octane from the upper ganglion. The uncertainty in our measurement of the oil volume was 0.4 mm^3. This is the same system for which we performed the intermolecular force calculation in the previous section. An oil film of thickness t=310 nm would give this drainage rate. Our predicted oil film thickness from the previous section is 242 nm, which is consistent with our measurements.

We then performed a series of experiments in a capillary tube of square cross-section with

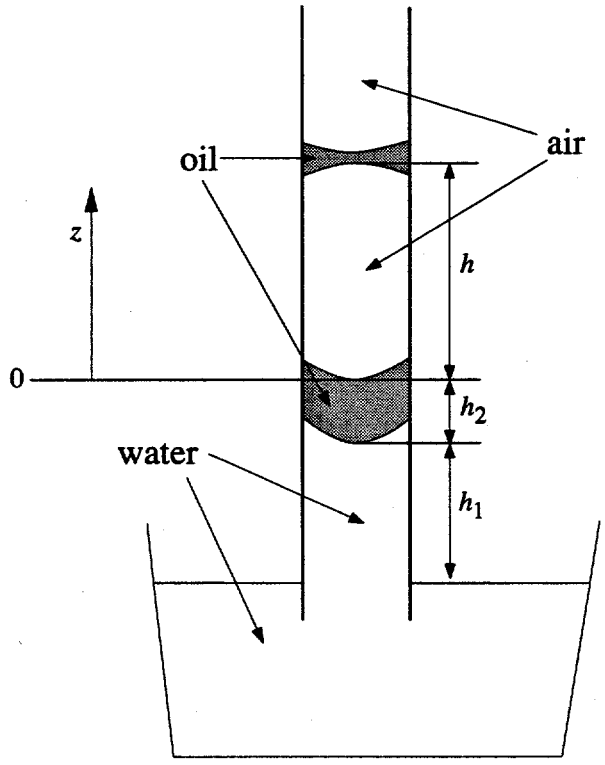

Figure 4.13: Fluid configuration in a capillary tube with square cross section at the beginning of drainage.

a side of length 150 μm. We repeated the experiment for various values of h_2 and h. In each experiment the volume of oil above the gas was 0.225 mm^3.

Fig. 4.14 shows the results for the system with a high interfacial tension (IFT). The triangles are the drainage times for different values of h when there is no initial oil bank ($h_2 = 0$) and the squares are the drainage times for the same fluids for various h and $h_2 = 4$ cm. Increasing h reduces the drainage time. The solid and dotted curves are our predicted times. The only unknown parameter in the prediction is the conductance constant for the oil layer. This was estimated to match the experimental results – only one parameter was used to match both curves. The agreement between experiment and theory is good. Notice that the minimum drainage time is just a few minutes, or several thousand times faster than in the capillary tube, even though the tube is smaller for this experiment. The reason for this is that the oil can form a much thicker layer (up to 15 μm across) in the corners of the tube than can be supported on a smooth, concave interface (only around 200-300 nm).

Fig. 4.15 shows the results from the low IFT system in the same capillary tube. Again the agreement between experiment and theory is good. The drainage times are longer because the viscosities of the water and oil phases are higher than for the high IFT fluids. We performed the same experiments with a mineral oil that has a negative spreading coefficient. In this case there was no drainage of the oil, since a spreading film was never established. On square capillaries with a side of 1 mm or larger, droplets of the oil were observed to fall down the glass, like rain droplets on a window pane. However, this phenomenon is only seen for large droplets and large capillaries and is unlikely to be significant in porous media. Real porous media do contain angular or sharp

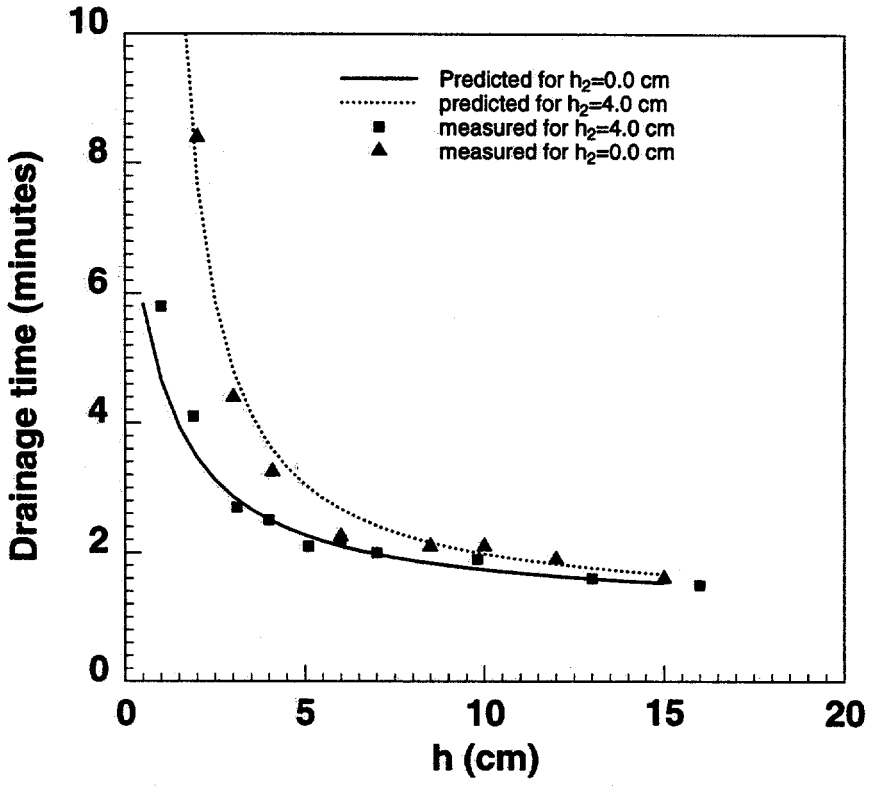

Figure 4.14: Comparison of measured and predicted drainage times in a capillary tube of square cross-section for a system with a high oil/water surface tension.

crevices that can support thick oil layers of order microns across during gravity drainage. This provides a mechanism for relatively rapid displacement of oil. Flow rates across flat surfaces or on uniformly concave interfaces are much slower. In all cases there is agreement between the predicted and measured flow rates.

4.2.5 Vertical Equilibrium

A critical height

We now analyze the fluid distribution in vertical capillary/gravity equilibrium, at the end of drainage, for systems with a positive spreading coefficient and for oils less dense than water. Consider again the arrangement of fluid illustrated in Fig. 4.12. Since there is no direct contact of water by gas, to the gas phase, oil and water combined appear to be the wetting phase. This means that the gas/oil capillary pressure can be represented as a function of total liquid saturation $(S_o + S_w)$, as first suggested by Leverett [83] and confirmed by Parker et al. [102]. In contrast, when $Cs < 0$, oil remains in the system as lenses and is influenced by both oil and water separately. As shown by Kalaydjian [69], this results in a gas/oil capillary pressure that is a function of both S_w and S_o rather than $S_o + S_w$ alone.

Fig. 4.16 shows gas, oil and water in vertical equilibrium. $z = 0$ is defined as the level at which oil is first mobile, or continuous, through the soil or rock. $z = H$ corresponds to the height at which gas is first continuous. Above $z = H$ all three phases may be continuous. This diagram corresponds to the arrangement of nonaqueous phase pollutant resting on the water table, or oil

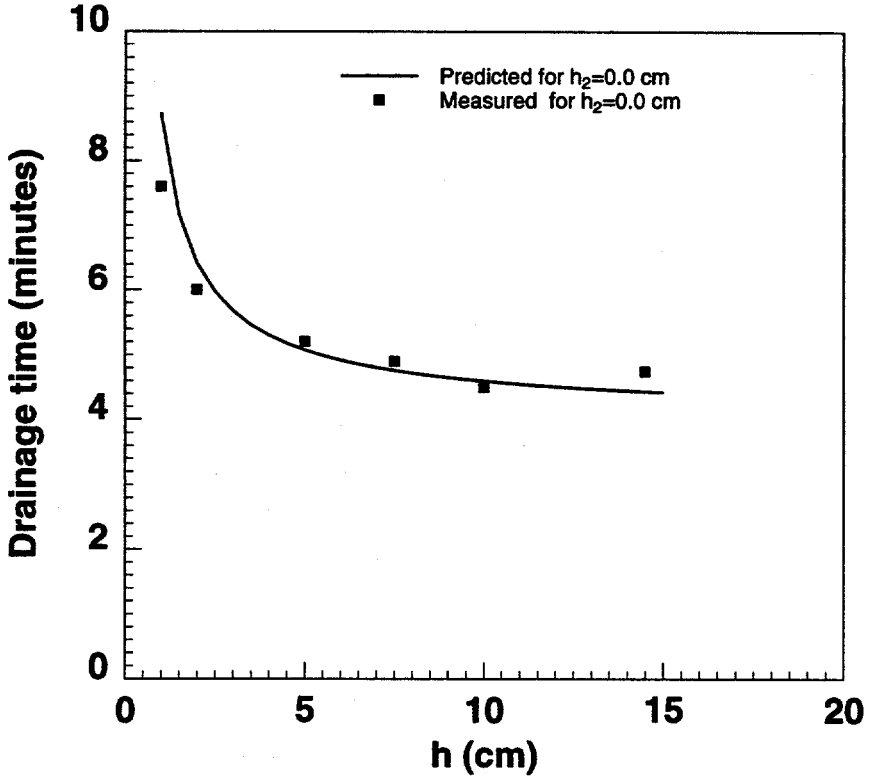

Figure 4.15: Comparison of measured and predicted drainage times in a capillary tube of square cross-section for a system with a low oil/water surface tension.

and gas in a reservoir. Where the phases are connected we can write down expressions for the pressures as a function of height

$$P_w = -z\rho_w g, \tag{4.43}$$

where P_w is the water pressure, g the acceleration due to gravity and we define $P_w = 0$ at $z = 0$. Similarly we may write

$$P_o = P^*_{cow} - z\rho_o g, \tag{4.44}$$

$$P_g = P^*_{cgo} + P^*_{cow} - H\rho_o g - (z - H)\rho_g g, \tag{4.45}$$

where P^*_{cow} and P^*_{cgo} are the threshold capillary pressures for oil invasion into water and gas invasion into oil respectively. The capillary pressures are

$$P_{cow} = P_o - P_w = P^*_{cow} + z(\rho_w - \rho_o)g, \tag{4.46}$$

$$P_{cgo} = P_g - P_o = P^*_{cgo} + (z - H)(\rho_o - \rho_g)g. \tag{4.47}$$

If the spreading coefficient is positive, the gas/oil capillary pressure is a function of the sum of the water and oil saturations. The oil/water capillary pressure, where water is the wetting phase, is a function of S_w. We assume that the functional forms of both capillary pressures are the same, but multiplied by their respective surface tensions, which control the relative strength of capillary forces [7, 83].

$$P_{cow} = \gamma_{ow} J(s_w) + \Pi_w, \tag{4.48}$$

$$P_{cgo} = \gamma_{go} J(s_w + s_o) + \Pi_o, \tag{4.49}$$

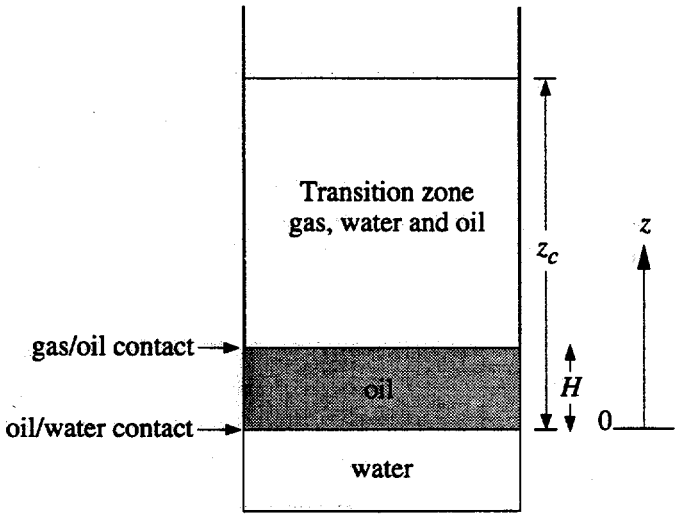

Figure 4.16: A schematic of the arrangement of water, oil and gas in vertical equilibrium.

where J is a capillary pressure function that represents the curvature of the fluid interfaces as a function of saturation. In terms of the microscopic configuration of fluid, shown in Fig. 4.12, $J(S_w)$ in Eq. 4.48 is $1/r_{ow}$ and $J(S_w + S_o)$ is $1/r_{go}$ However, this argument is completely general and does not rely on any particular model of the pore level fluid distribution. The threshold capillary pressures can be written $P^*_{cow} = \gamma_{ow} J^*$ and $P^*_{cgo} = \gamma_{go} J^*$, where J^* is the curvature necessary for a phase to first enter the porous medium. The capillary pressure decreases with wetting phase saturation [7]. Hence

$$J(S_w) \geq J(S_w + S_o). \tag{4.50}$$

This is equivalent to stating that $r_{go} \geq r_{ow}$ for an oil layer to exist in Fig. 4.12. From Eqs. 4.48 and 4.49 the inequality above becomes

$$\frac{P_{cow} - \Pi_w}{\gamma_{ow}} \geq \frac{P_{cgo} - \Pi_o}{\gamma_{go}}. \tag{4.51}$$

Notice that this is identical to Eq. 4.41. By using a capillary pressure analysis, or by considering the microscopic arrangement of fluid in a pore, we arrive at the same inequality for continuity of the oil phase. We substitute Eqs. 4.46 and 4.47 into 4.51 to find

$$\frac{z - \frac{\Pi_w}{(\rho_o - \rho_g)g}}{(z - H) - \frac{\Pi_o}{(\rho_w - \rho_o)g}} \geq \alpha, \tag{4.52}$$

where

$$\alpha = \frac{\gamma_{ow}}{\gamma_{go}} \frac{\rho_o - \rho_g}{\rho_w - \rho_o}, \tag{4.53}$$

Thus, α is a property of the fluid surface tensions and densities. This expression, without accounting for disjoining pressure, was first derived by Kantzas et al.[72]. For a bulk phase to be present, the disjoining pressures will be negligible and we may write

$$\frac{z}{z - H} \geq \alpha. \tag{4.54}$$

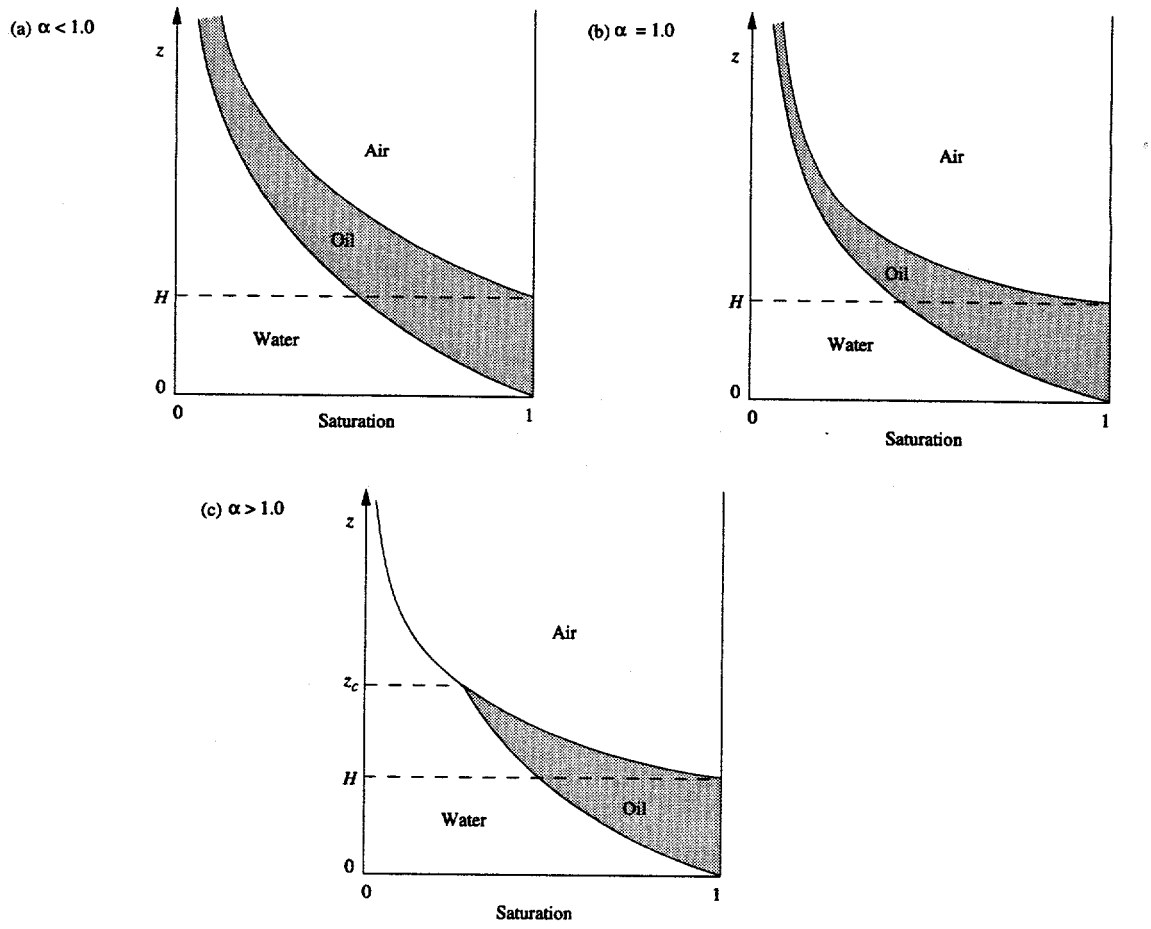

Figure 4.17: The distributions of water, oil and gas in vertical equilibrium. (a) for $\alpha < 1$; (b) for $\alpha = 1$; and (c) for $\alpha > 1$.

For $0 < \alpha < 1$, the inequality above is always obeyed, which means that connected oil exists at all heights above the oil bank. If $\alpha > 1$, there is a finite height at which oil in thick layers cannot exist, which means that oil must reside in thin films a few nanometers across, where the disjoining pressures are significant. The oil saturation of this film will be at most 0.01% and may be considered negligible. The critical height z_c at which the oil saturation becomes virtually zero is

$$z_c = \frac{\alpha H}{\alpha - 1} = H + \frac{H}{\alpha - 1}. \tag{4.55}$$

For systems with $\alpha > 1$ the minimum oil saturation is zero. In contrast, residual oil saturations in the range 0.1 to 0.5 are encountered in water-saturated porous media [34]. Lowering the water table in a region polluted by free product, or gas cap expansion into a waterflooded reservoir, will mobilize this trapped oil and allow some of it to be recovered by direct pumping.

Fig. 4.17 shows schematic graphs of saturation versus height for different values of α. Fig. 4.17(c), for $\alpha > 1$, demonstrates how the connected oil saturation decreases to zero at some critical height z_c. Above z_c, the fluid distribution is governed by the gas/water capillary pressure (the sum of Eqs. 4.46 and 4.47). The gas/water interfaces will be covered with an oil film, giving a lowered effective gas/water surface tension and an effective spreading coefficient that is approximately zero [3, 110]. For continuity of the water phase at $z = z_c$ the effective gas/water surface tension must be $\gamma_{ow} + \gamma_{go}$.

How much oil can be trapped?

If gas displaces connected oil, there is no mechanism for the oil to become trapped and the oil saturation above z_c will be zero. If gas displaces trapped oil, such as waterflood residual oil in a reservoir, or immobile product just below the water table, oil can remain trapped if it has not been directly contacted by gas. This interpretation is consistent with sand column experiments which showed better recoveries for gravity drainage from continuous oil than for drainage of hitherto residual oil [71].

In this section we will consider gravity drainage of previously discontinuous oil. An indication of the amount of oil that can remain trapped is the water saturation at z_c. Trapped oil at $z = z_c$ is contained in ganglia completely surrounded by water that has not been displaced by gas. At heights above and below z_c less oil will be trapped. Above z_c, the water saturation is lower and more oil will have been contacted by gas. Below z_c the mobile oil will have reconnected previously trapped ganglia. If we know the three phase capillary pressures, we can calculate the oil and water saturations. One possible parameterization for the capillary pressure function J is [15]

$$J(S_w) = J^* S^{-1/\lambda}, \tag{4.56}$$

where J^* represents the threshold entry curvature [22], S is the wetting phase saturation and λ is a constant that depends on the pore structure of the medium and is generally in the range 0.2 1.0 [81]. Other expressions for the capillary pressure have been proposed [102, 126]. The capillary pressure we use has no irreducible or residual water saturation [81]. We could allow an irreducible water saturation, but we do assume that all the oil filled pores can be accessed by gas.

We use Eqs. 4.46, 4.48, 4.53 and 4.56 to find the water saturation as a function of height

$$S_w = \left(1 + \frac{z(\rho_o - \rho_g)g}{\alpha J^* \gamma_{go}}\right)^{-\lambda}. \tag{4.57}$$

and at $z = z_c$, from Eq. 4.55

$$S_w(z_c) = \left(1 + \frac{H(\rho_o - \rho_g)g}{(\alpha - 1)J^* \gamma_{go}}\right)^{-\lambda}. \tag{4.58}$$

If we increase H, the water saturation at z_c decreases, as illustrated in Fig. 4.18. This means that the trapped oil saturation at z_c decreases and the gravity drainage process is more efficient. If we take typical values for a polluted sandy soil: $H = 0.1$ m, $J^* = 10^4$ m^{-1}, $\alpha = 4$, $\lambda = 1$, $\rho_w - \rho_g = 10^3$ kgm^{-3}, $\rho_o - \rho_g = 700$ kgm^{-3} and $\gamma_{go} = 0.02$ Nm^{-1}, we find $S_w = 0.47$, which could allow some oil to be trapped. However, if the pore size distribution is uniform, very little oil remains trapped, even for small values of H, as demonstrated in sand column experiments [71]. In contrast, a large oil bank in a water-wet reservoir, with the same values as above, except $J^* = 10^5$ m^{-1} and $H = 100$ m, gives S_w as less than 1%. The residual oil saturation at z_c must therefore be much less than 1%. Oil is only trapped if we have a mixed-wet or oil-wet system.

If we have a nonspreading system, three phase contact lines between the phases are stable, oil films and layers do not form and oil can remain trapped. The recovery from gravity drainage will be lower than for systems with $C_s > 0$ with the same value of α.

Experimental confirmation

Several investigators have performed gravity drainage experiments, where gas displaces water and residual oil, or oil and residual water, under gravity [11, 18, 35, 71, 72, 127] and have shown that final oil saturations as low as 1% are possible. These very good recoveries have been

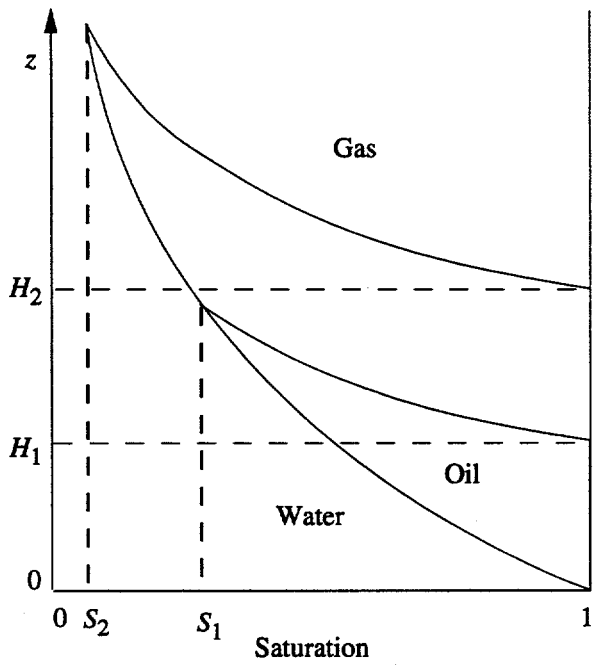

Figure 4.18: A schematic of water saturation variation with the increases in the height of oil bank.

explained by the drainage of oil layers between the gas and water [69, 70, 97, 96, 113]. It has been shown that lower final oil saturations are seen for systems with a positive spreading coefficient than for nonspreading oils [70, 97, 127]. However, none of these authors made quantitative predictions of the variation of recovery with fluid properties.

We performed experiments in sand columns of two heights: a long column of 97.5 cm, and a short column of 47 cm. Both columns had a diameter of 2 cm. They were filled with a clean, well-sorted sand with a mean grain diameter of approximately 0.3 mm, a permeability of 48 D and porosity of 0.28.

The sand column was first fully saturated with water. The top and bottom valves at the end of the column were then both opened to allow the invasion of air and the free drainage of water. We waited at least 24 hours until no further water was produced. 30 cm^3 of oil was then slowly poured into the top of the column to represent the migration of draining oil towards the gas/water contact. Oil accumulated at the bottom of the column and was allowed to drain out freely. Periodically, air at just above atmospheric pressure was pumped into the top of the column to displace the oil bank. This exercise stopped when there was no further production of fluids. No further oil was recovered after two weeks of drainage.

For a nonspreading mineral oil (Drakeol 5), we found that 14 cm^3 remained in the long column and 9 cm^3 remained in the short column. Zhou and Blunt [133] conducted the experiment described here for spreading systems with various values of α. By using Corey type capillary pressures, Eq. 4.56, the amount of oil left in the columns could be matched using $\lambda = 0.92$, a value previously measured on a well-sorted sand by Lenhard and Parker [81].

Fig. 4.19 plots the results for both the spreading and nonspreading oils. There is little change in oil saturation for the short column. This is because the critical height z_c is above the top of the column for most of the experiments, and thus it is difficult to distinguish between $\alpha < 1$, $\alpha > 1$, spreading and nonspreading systems. For the long column, however, the average saturation at the end of the experiment decreases from approximately 16% for $\alpha = 0.47$ to 8% for $\alpha = 4.0$. The difference in recovery for the two columns represents the amount of oil remaining in the upper

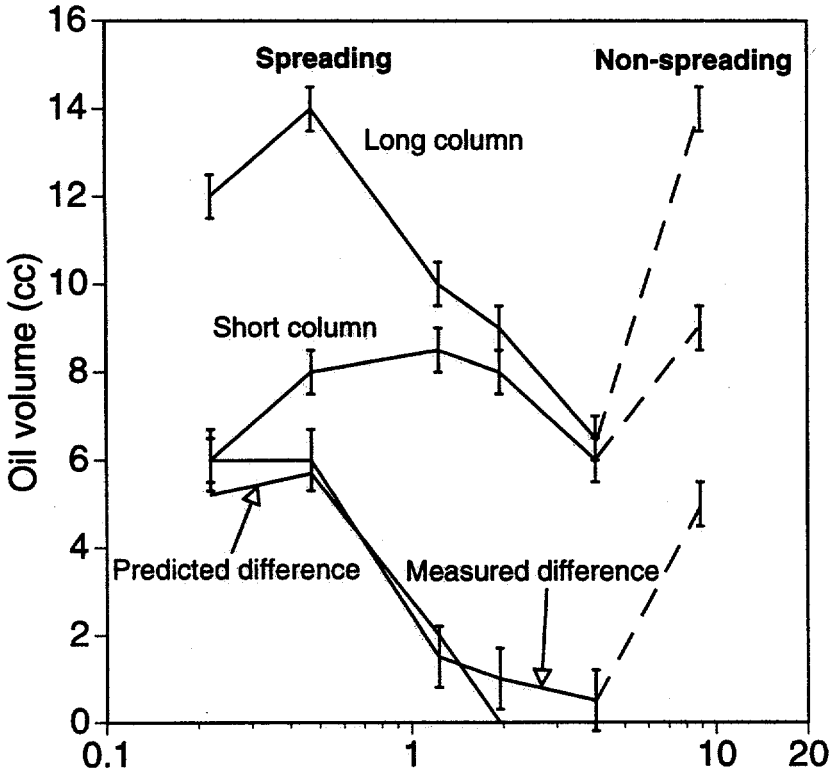

Figure 4.19: The amount of oil remaining in the sand columns as a function of α.

portion of the long column which varies from 14 1for $\alpha = 0.47$ to 1±1% for $\alpha = 4.0$. For a spreading system, the final oil saturation well above the oil/water contact changes by a factor of twelve with α . The oil remaining can be predicted successfully, as shown in Fig. 4.19. For large α the amount left is zero to within experimental error. The nonspreading oil (the points to the right in Fig. 4.19) gives a poor recovery, even though it has a large value of α, because in this case oil can be trapped.

Discussion

The critical parameter that determines oil recovery by gravity drainage for a spreading system is α, which is a property of the fluid system alone and independent of the porous medium, as long as it is water-wet. For most fluids $\alpha > 1$, which means that above a critical height the residual oil saturation can be zero. However, if surfactant flooding is used to displace oil in the presence of gas, this will dramatically decrease γ_{ow}, and α will be less than 1. This will mean that in vertical equilibrium, appreciable quantities of oil can be retained above the oil/water contact. The recovery of oil from gravity drainage is most efficient for large α, which can be achieved by lowering the gas/oil surface tension. In oil reservoirs, the natural gas may be almost miscible with the oil, leading to very low values of $\gamma_{go}/(\rho_o - \rho_g)$ and an extremely high oil recovery.

4.2.6 Conclusions

The mechanism of gravity drainage is transport through thick oil layers sandwiched between water and gas, which occupy the crevices of the pore space. These layers form spontaneously if the

spreading coefficient is positive. In the experiments we performed, nonspreading systems did not form oil layers and gave poorer recoveries.

The distribution of oil, water and gas in vertical equilibrium for a spreading system is controlled by the parameter α, Eq. 4.53. Typically $\alpha > 1$, and there is a finite height above which the oil saturation can be zero, apart from thin molecular films. This height is a function only of the fluid densities and surface tensions and is independent of the soil or rock type. For $\alpha < 1$, which is seen for surfactant floods, a large quantity of oil can be contained above the oil bank.

4.3 Predicting the Spreading and Stability of Thin Hydrocarbon Films

Darryl H. Fenwick

4.3.1 Introduction

In the previous section, the importance of oil films to three-phase gravity drainage was established, and experimental results were reported that show that low saturations can be achieved. In this section we examine the fundamental forces that create and maintain oil films. The goal of this work is to establish a physical explanation for transport of oil at low saturations, whether that transport is due to viscous forces or gravity forces, and to provide understanding of the physical mechanisms that can be used in the design of gas injection processes to create conditions at which that transport is possible.

One of the first recorded experiments concerning the spreading of oil on a water surface in the presence of air was performed by Benjamin Franklin [120] in 1770. Franklin observed during an ocean voyage that as the cooks dumped their greasy water overboard, it had the effect of smoothing the wake of the ships. Inspired, Franklin performed an experiment on Clapham pond in London, where on a windy day he poured a small amount of oil on the rough pond, which rapidly spread out and covered nearly half an acre, smoothing the surface of the pond. Franklin found it remarkable that the same oil that remains in droplets when placed upon a marble table could spread so rapidly to such a small thickness when placed upon water. It may not have been apparent to Franklin at the time that this phenomena is caused by very subtle intermolecular forces that govern the interfacial tensions. Interestingly, since he knew the volume of oil which he placed upon the water, and he approximated the area that the oil covered, he could have made a calculation as to the thickness of the oil film. If he had, the thickness would of been on the order of 1 nanometer, which would've given Franklin remarkable insight into the size of molecules for his time.

Due to the effort of Franklin and the many scientists that followed him, it is common knowledge that many hydrocarbons will spread on water. Many oils, such as mineral oil or n-decane, will not spread on water. The spreading of oil on water in the presence of air is determined by the equation that defines the initial spreading coefficient,

$$S^I = \gamma_{gw} - (\gamma_{go} + \gamma_{ow}), \tag{4.59}$$

where γ_{ij} is the interfacial tension between phases i and j. Fig. 4.20a shows that Eq. 4.59 is simply a force balance at the three phase contact line of water/oil/gas. If $S^I > 0$, then there is no contact angle θ that balances the forces in the horizontal direction. Hence, the oil will spread.

When oil molecules are allowed to occupy the gas/water interface, either through the spreading of the oil over the water or through adsorbtion from the vapor phase, then the gas/water interfacial tension is reduced and is defined as an effective gas/water interfactial tension, γ^e_{gw}. It is

the lowering of the gas/water interfacial tension that causes the smoothing of the waves observed by Franklin. When the three phases are at equilibrium, the equilibrium spreading coefficient can be defined as

$$S^{eq} = \gamma_{gw}^{e} - (\gamma_{go} + \gamma_{ow}) . \tag{4.60}$$

If $S^{eq} = 0$, then the contact angle θ will be zero, and the oil will reside in a flat film (Fig. 4.20b). If $S^{eq} < 0$ and $S^{I} > 0$, then the oil will spread initially, but a finite contact angle θ^{e} exists such that the oil will be found in blobs connected by thin films that occupy the gas/water interface (Fig. 4.20c). The latter is found to be the case for benzene [3] as well as pentane, hexane, and heptane [26].

When gas contacts oil in a water-wet porous medium, which occurs during gas injection into a water-wet oil reservoir, the three phases will behave in the same manner as Benjamin Franklin observed. If the initial spreading coefficient of the oil is positive, the oil will spread between the water and gas. The equilibrium configuration will depend on S^{eq}, as indicated in Fig. 4.20. The initial spreading coefficient has important implications for the recovery of oil from porous media. In many experiments simulating gas injection processes, final oil saturations as low as 1% have resulted from the displacement of oil in the presence of both water and gas. It has been suggested that this high recovery is because of the existence of a layer of oil between the water and gas phases, making a continuous channel through which the oil can drain ([10], [?], [12], [18], [73], [99], [98]). In gas condensate reservoirs, the condensed fluid will also be found in continuous films between the water and gas. Since γ_{go} will be small, the initial spreading coefficient will most likely be positive. The condensate can also be recovered by drainage through the layers between the water and gas. For CO_2 injection as well, γ_{go} will be small as miscibility is approached, and S^{I} may increase positive values, creating continuous oil films. This may be another method in which CO_2 helps to increase recovery.

Therefore, a positive spreading coefficent enables the oil to be connected down to very low saturations through the thin films between the water and gas that results in a low residual oil saturation. The stable thickness of the oil film also has consequences for the recovery of oil. If the equilibrium thickness of an oil film is found to be very small, such as the molecular size film that Benjamin Franklin might have found, then the drainage of oil through the thin film is expected to be much slower than a thicker film [10].

Of course, one cannot approximate a porous medium by the surface of a pond. Most oil reservoirs are at elevated temperature, which can affect the interfacial tensions (and consequently S^{I} and S^{eq}). The presence of the rock can affect the intermolecular forces that govern the spreading coefficients. Water salinity can also affect the initial and equilibrium spreading coefficient. Also, the surfaces in porous media are not flat, but contain many corners, edges, grooves, and asperities. The curvature of the water surfaces may enhance or diminish the stability of thick films of oil to exist. Also, Dong et al. [31] demonstrated that oil is capable of imbibing between water and gas in the corners of the pore space. The imbibition of oil is constrained by the curvature of the oil/water interface and the angle of the corner where the oil might imbibe. Because oil imbibition into corners is dependant upon pore geometry, it may not be the more common method for oil to be established in films between water and gas. However, this phenomena may help to explain certain experimental results (such as Dumoré and Schols [35]). This section will not discuss oil imbibition into corners.

This section presents an analysis of the intermolecular forces that determine the initial and equilibrium spreading coefficients and the stability (i.e. the equilibrium thickness) of hydrocarbon films on water in the presence of gas. Lifshitz theory (see [37]) is used to evaluate the intermolecular interactions. Lifshitz theory uses quantum field theory to provide an exact expression of the

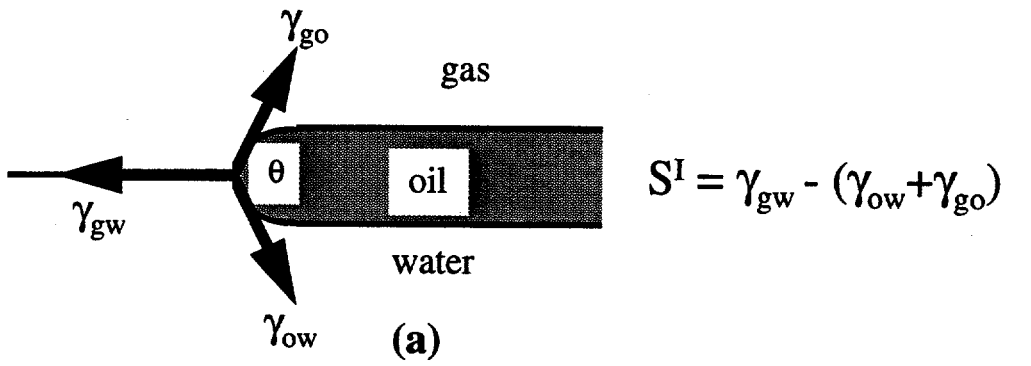

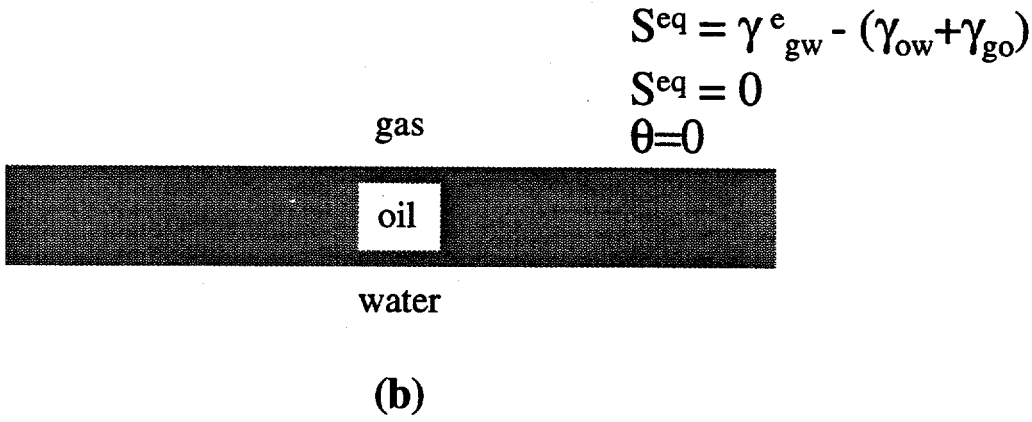

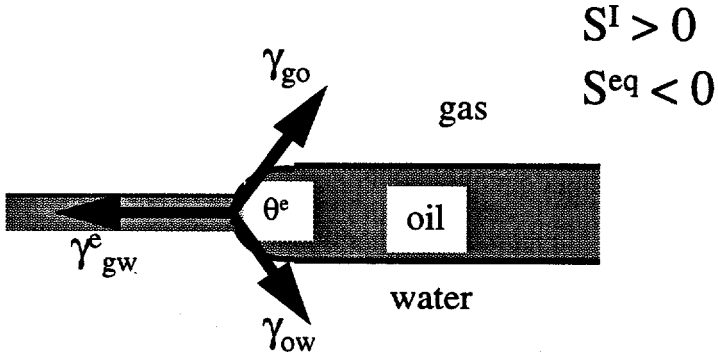

Figure 4.20: (a) A blob of oil initially resting on water in the presence of gas, (b) the configuration of the three phases when $S^{eq} = 0$, (c) The configuration when $S^I > 0$, and $S^{eq} < 0$.

energy and force across thin films. The expressions can only be solved for simple geometries, such as the semi-infinite slab configurations in Figs. 4.21a and 4.21b. For even simple systems such as those depicted, the equations are very complex. Thus, most authors use approximate forms when calculating intermolecular interactions ([57], [58], [59], [95], [105]). Hirasaki [58] used an approximate form for the Lifshitz theory equations and an equation to approximate the intermolecular interactions at very small film thicknesses (discussed in Section 4.3.2) to predict the initial and equilibrium spreading coefficients with good accuracy. Here, the full expression will be used to predict the behavior of several of the n-alkanes as well as benzene and cyclohexane.

The spreading and stability for flat hydrocarbon films, such as the film in the experiment of Benjamin Franklin and shown in Fig. 4.21a, will be considered first. Systems more applicable to porous media will consequently be discussed. The influence of an underlying solid underneath the water depicted in Fig. 4.21b will be investigated. The effect of water salinity and temperature on flat films will be demonstrated. Finally the influence of curvature on film stability will be considered. First, a brief introduction to Lifshitz theory and the concept of disjoining pressure is required.

4.3.2 Calculation Procedure

The full expression of the energy for the system depicted in Fig. 4.21a is expressed as [37],

$$\begin{aligned} E(l) &= \frac{kT}{8\pi l^3} \sum_{n=0}^{\infty\,\prime} \left(\frac{2\xi_n l\sqrt{\epsilon_2}}{c}\right)^2 \int_1^\infty p(\ln(1-\Delta_{12}\Delta_{32}\exp(-2p\xi_n l\sqrt{\epsilon_2}/c))) \\ &+ p\,(\ln(1-\bar{\Delta}_{12}\bar{\Delta}_{32}\exp(-2p\xi_n l\sqrt{\epsilon_2}/c)))\,dp. \end{aligned} \tag{4.61}$$

In Eq. 4.61,

$$s_1 = \sqrt{\epsilon_1/\epsilon_2 - 1 + p^2}, \qquad s_3 = \sqrt{\epsilon_3/\epsilon_2 - 1 + p^2},$$

$$\Delta_{12} = \frac{s_1 - p}{s_1 + p}, \quad \Delta_{32} = \frac{s_3 - p}{s_3 + p} \quad \bar{\Delta}_{12} = \frac{s_1 - p\epsilon_1/\epsilon_2}{s_1 + p\epsilon_1/\epsilon_2}, \quad \bar{\Delta}_{32} = \frac{s_3 - p\epsilon_3/\epsilon_2}{s_3 + p\epsilon_3/\epsilon_2},$$

ϵ_1, ϵ_2, ϵ_3, are functions of the imaginary frequency $i\xi_n$, where $\xi_n = 2\pi nkT/\hbar$ (n=1,2,3, ...), k is Boltzmann's contant, T is absolute temperature, c is the speed of light, $2\pi\hbar$ is Plank's constant, p is an integration variable, and ϵ is the dielectric permittivity of the material. The summation is over integral values of n, and the prime on the summation means that the first term in the summation should be multiplied by 1/2. Most authors approximate the energy of the configuration shown in Fig. 4.21a as,

$$E(l) = \frac{A_{123}}{12\pi l^2}, \tag{4.62}$$

where A_{123} is called the Hamaker constant. A comparison of Eq. 4.61 and Eq. 4.62 demonstrates that A_{123} is a function of film thickness and temperature, and is not a constant value. However, the Hamaker constant approaches a constant value for very small film thicknesses.

The derivative of the energy with respect to the thickness gives the force [37],

$$\begin{aligned} F(l) &= \frac{kT}{\pi c^3} \sum_{n=0}^{\infty\,\prime} \epsilon_2^{3/2}\xi_n^3 \int_1^\infty p^2 \left(\left[\frac{1}{\Delta_{12}\Delta_{32}}\exp(2p\xi_n l\sqrt{\epsilon_2}/c) - 1\right]^{-1}\right) \\ &+ p^2 \left(\left[\frac{1}{\bar{\Delta}_{12}\bar{\Delta}_{32}}\exp(2p\xi_n l\sqrt{\epsilon_2}/c) - 1\right]^{-1}\right) dp. \end{aligned} \tag{4.63}$$

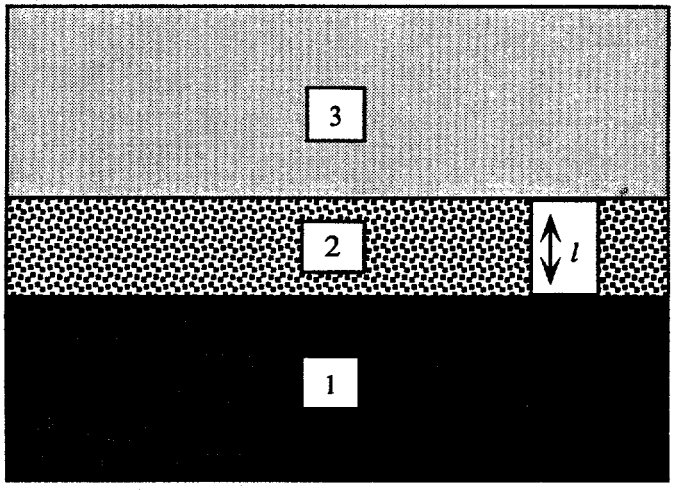

(a)

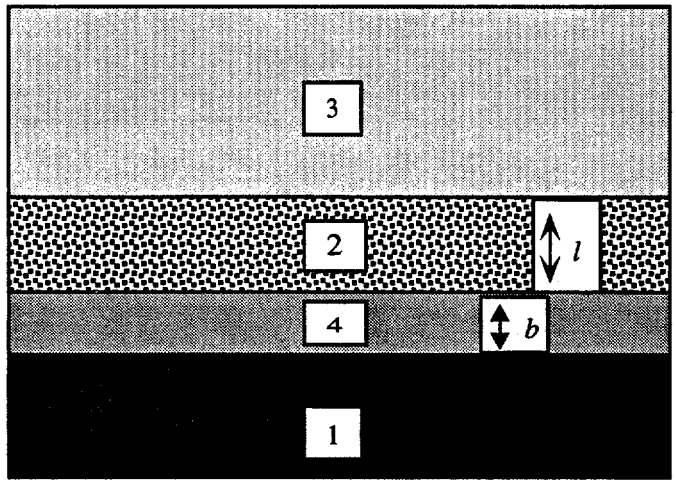

(b)

Figure 4.21: (a) Two semi-infinite slabs of materials 1 and 3 separated by medium 2 of thickness l. (b) Additional layer of material 4 of thickness b on material 1.

Eq. 4.61 and Eq. 4.63 can be solved given the dielectric permittivity ϵ as a function of electromagnetic frequency for materials 1, 2, and 3. The behavior of $\epsilon(i\xi_n)$ for the materials in the system will determine the disjoining pressure curve. (The form of $\epsilon(i\xi_n)$ for the molecules discussed in this section can be found in [59] and [103].) The dielectric permittivity is also a function of temperature. Unfortunately, the variation of ϵ with temperature is not well defined. Hirasaki [58] made approximations to find the variation of the disjoining pressure with temperature, which will be discussed later. Increasing salinity also affects the values of $\epsilon(i\xi_n)$ for water ([108]), and thus the disjoining pressure curve.

For the case of Fig. 4.21b, where material 4 is covering material 1, the expressions for energy and force are the same as Eqs. 4.61 and 4.63, except that

$$\Delta_{21} = \frac{\Delta_{24} + \Delta_{41}\exp(-bs_4/l)}{1 + \Delta_{24}\Delta 41\exp(-bs_4/l)},$$

where s_4, Δ_{41}, and Δ_{24} are analagous to the expressions given above.

A well known and useful term, the disjoining pressure Π is simply the opposite of the force,

$$\Pi = -\frac{\partial E}{\partial l} = -F(l). \tag{4.64}$$

The oil disjoining pressure is found in the augmented Young-Laplace equation for the capillary pressure between gas and oil,

$$P_{c_{go}} = 2H\gamma_{go} + \Pi(l)_o,$$

where $P_{c_{go}}$ is the gas/oil capillary pressure, γ is the interfacial tension, and $2H$ is the mean curvature of the interface between the phases. The disjoining pressure can be thought of as the additional pressure a film of fluid exerts to promote its stability. Thus a positive disjoining pressure indicates that the thin film can support a difference in pressure beyond that which the curvatures between the two phases would indicate.

The condition of stability for the system depicted in Figs. 4.21a and b is [28],

$$P_{c_{go}} = \Pi_o, \qquad \frac{\partial \Pi_o}{\partial l} < 0,$$

that is, the pressure difference between the two bulk phases must intersect the disjoining pressure curve where the slope is negative. It is important to note, however, that Eq. 4.61 and Eq. 4.63 approximate the molecules as single points in the medium. Thus, when the thin film approaches the size of the molecule, the equations deviate from the true values.

The deviation from Lifshitz theory is due to structural forces ([21], [28]). Structural forces account for the finite-sized molecular effects on the behavior of the thin film. Due to the very complex nature of finite-sized molecular interactions, very few forms for the structural forces exist. A semi-empirical exponential decay expression for structural forces has been proposed ([21], [60]),

$$\Pi_s(l) = A\exp(-l/\sigma), \tag{4.65}$$

where σ is the characteristic molecular size of the film. Since the energy of the system at zero thickness is equal to the initial spreading coefficient (see [10], [25]), the constant A is equal to S^I/σ. Eq. 4.65 is usually added to the general Lifshitz expression (Eq. 4.64) up to a given decay length. However, the energy of the system is not continuous if this is the case, which is unphysical. Thus, a scheme has been developed that combines the structural forces to the continuum disjoining

pressure equation such that the energy is a smooth function. This expression approximates the structural forces well. Unfortunately, the initial spreading coefficient of the system must be known.

Hirasaki [58] has also derived an expression for the structural force of a thin film by assuming that under molecular thickness, the film behaves like a two dimensional gas. This assumption allows an expression for the structural forces to be obtained by using the 2-D van der Waals equation of state.

$$\Pi_s(l) = -\frac{A_{123}}{6\pi(l^*)^3} + \frac{2a_2 l}{v^2} - \frac{kT}{v}\left(\frac{v}{v - b_2 l} - \ln\left(\frac{v}{lb_2} - 1\right)\right) \tag{4.66}$$

For Eq. 4.66, A_{123} is the Hamaker constant evaluated at small thickness l^*, v is the specific volume of material 2, and a_2 and b_2 are the 2-D van der Waals equation of state parameters. The transition from structural forces to the continuum model occurs when the two curves intersect. This approach works well in predicting the initial and equilibrium spreading coefficients of many systems. However, the energy is also discontinuous at the intersection of the two curves. Eq. 4.66 gives an expression of the structural forces that contains more physical insight than the semi-empirical Eq. 4.65. Later, a comparison of the results using the two expressions will be made.

Once the expression for the disjoining pressure as a function of length is evaluated, the initial and equilibrium spreading coefficient of the system can be determined. The initial spreading coefficient is given by ([90]),

$$S^I = \lim_{l \to \infty} \int_{\Pi(l=0)}^{\Pi(l^*)} l' d\Pi'. \tag{4.67}$$

Eq. 4.67 allows us to predict the spreading coefficient given $\Pi(l)$. Consequently, any change in $\epsilon(i\xi_n)$ or temperature will affect S^I. The equilibrium spreading coefficient is given by ([90]),

$$S^{eq} = -\int_{\infty}^{l_{eq}} \Pi' dl' + (\Pi l)_{eq}. \tag{4.68}$$

The subscript eq indicates the values should be evaluated at equilibrium. Thus, Eq. 4.68 shows how the equilibrium spreading coefficient varies as the thin film varies in thickness. If an initial and equilibrium spreading coefficient for a given system is known, Eqs. 4.67 and 4.68 can be used to determine whether a reasonable characterization of the intermolecular forces has been found.

4.3.3 The Behavior of Flat Films - No Curvature

Several authors have already investigated the stability of flat hydrocarbon films such as those depicted in Figs 4.21a (where material 1 is water, material 2 is oil, and material 3 is water or a gas) [108], [59], [26], [60], [58]. However, each approach had its limitations. Richmond et al. [108] and Del Cerro and Jameson [26] used a numerically dangerous and unnecessary interpolation procedure in obtaining $\epsilon(i\xi_n)$. Hirasaki [58] and Hough and White [59] used an approximate form of Eq. 4.61 accurate only for small film thicknesses (< 5nm). Israelachvili [60] used an approximate form of Eq. 4.61 as well as an approximate form of $\epsilon(i\xi_n)$. Only Hirasaki [58] included an expression for the structural forces.

Fig. 4.22 and Fig. 4.23 presents the disjoining pressures for a water/hydrocarbon/air system for several of the n-alkanes using Eq. 4.66 and Eq. 4.65 respectively for the structural forces. For

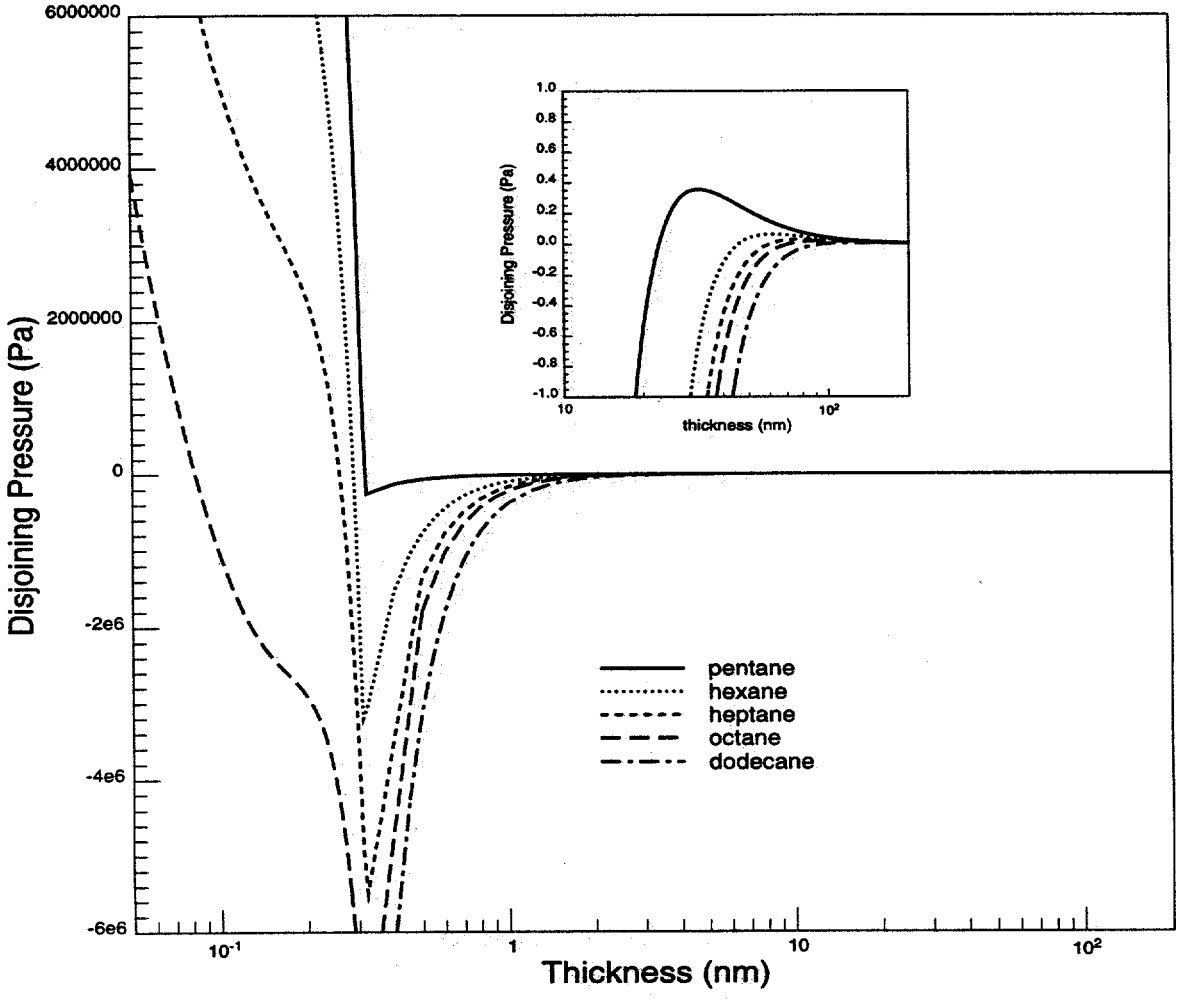

Figure 4.22: The disjoining pressure at 20°C as a function of film thickness for various n-alkanes using Eq. 4.66. Inset shows the disjoining pressure at large thicknesses.

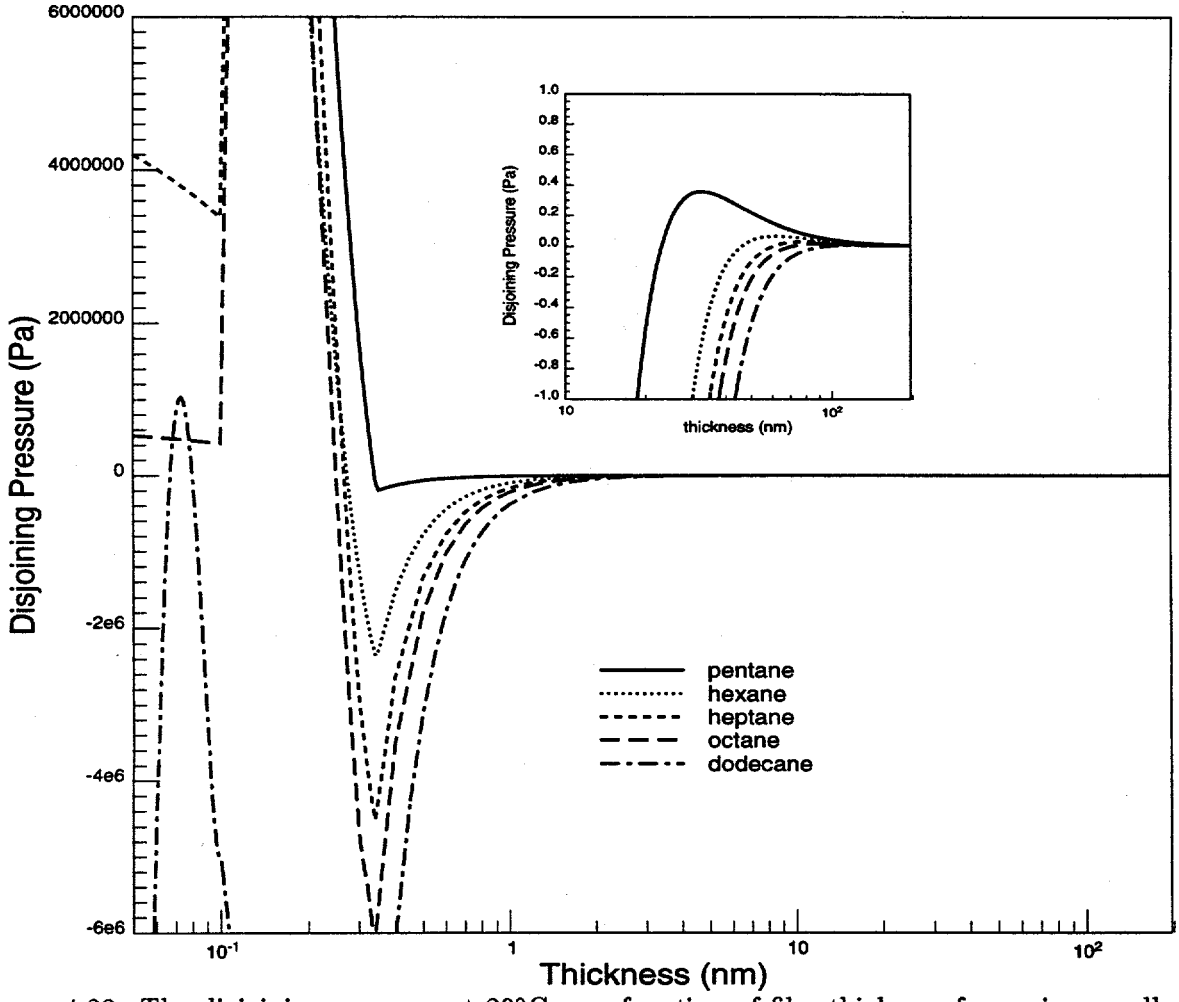

Figure 4.23: The disjoining pressure at 20°C as a function of film thickness for various n-alkanes using Eq. 4.65.

Table 4.4: Comparison of results with experiment using different forms for the structural forces (Eq. 4.65 and Eq. 4.66) at 20°C.

All values in mN/m

	Exp. Decay		Hirasaki		Experimental	
	S^I	S^{eq}	S^I	S^{eq}	S^I	S^{eq}
pentane	6.14	-0.04	6.39	-0.04	6.10	-0.50
hexane	3.51	-.52	3.31	-0.55	3.40	-0.50
heptane	1.40	-0.96	0.92	-1.12	1.20	-0.70
octane	0.35	-1.35	-1.25	-2.10	-0.80	-1.90
decane	-3.36	-3.06	-4.65	-4.89	-3.40	-3.90
dodecane	-5.79	-4.54	-6.77	-6.86	-5.80	-6.10
benzene	9.57	-4.45	4.71	-2.17	8.9	-1.6
cyclohexane	-2.86	-3.68	-3.32	-4.34	-2.95	-4.16

Fig. 4.23, σ was set to the value used by Hirasaki [58], which was 2.3 $\AA$. The decay length was chosen to be 1.5σ, which is a reasonable value [60]. Fig. 4.23 demonstrates the limitations of using the semi-empirical Eq. 4.65. Although the energy is a continuous function, the disjoining pressure is not. Also, the alkanes exhibit seemingly unphysical behavior as the film approaches $1\AA$. However, Table 4.4 indicates the simplified equation does agree well with the more physically based Eq. 4.66 and with the experimental results (taken from [58]), with the exception of decane and dodecane. These alkanes have $S^{eq} > S^I$, which is not physically possible. Note that the results for octane for the exponential decay structural forces used an initial spreading coefficient of $0.15mN/m$ ($S^{eq} = -0.85mN/m$) from the Girifalco and Good data taken from Hirasaki [58]. Note also that the data using the structural forces in Eq. 4.66 predict that at room temperature octane and heavier alkanes do not spontaneously spread on fresh water, but the lighter alkanes do spread.

Figs. 4.22 and 4.23 indicate that, for values of $P_{c_{go}}$ that we find in typical petroleum reservoirs ($\sim$ 5,000 Pa), the equilibrium film thickness of the hydrocarbons examined are on the order of molecular size or smaller. This has important consequences for film conductivity, which would be extremely low at such thicknesses. Note that the strength of the structural forces (the pressure scale is in MPa) can maintain the small film up to extreme pressure differences, which indicates that in gas injection processes or gas condensate reservoirs where oil can spread, a layer of oil between the water and gas will always be present.

Fig. 4.24 demonstrates that if $P_{c_{go}}$ were near 0.2 Pa, pentane could have a stable film thickness in the region of 55 nm. It is well documented that pentane exhibits strange behavior when placed on water [26]. The disjoining pressure curve for pentane demonstrates how the equilibrium thickness (and correspondingly the equilibrium spreading coefficient) can vary under subtle changes in pressure. If the capillary pressure were to drop even further, hexane, heptane, and octane could also form stable, thick films up to 100 nm. Such low capillary pressures are unlikely to exist under reservoir conditions.

4.3.4 The Influence of Underlying Rock

In water-wet reservoir rocks, the water will reside on the rock grains, possibly in very thin films. To determine whether the rock influences the stability of the hydrocarbon films, calculations were made for the configuration depicted in Fig. 4.21b, where material 1 is now crystalline quartz, material 4 is water of thickness b, material 2 is octane, and material 3 is air. The behavior of

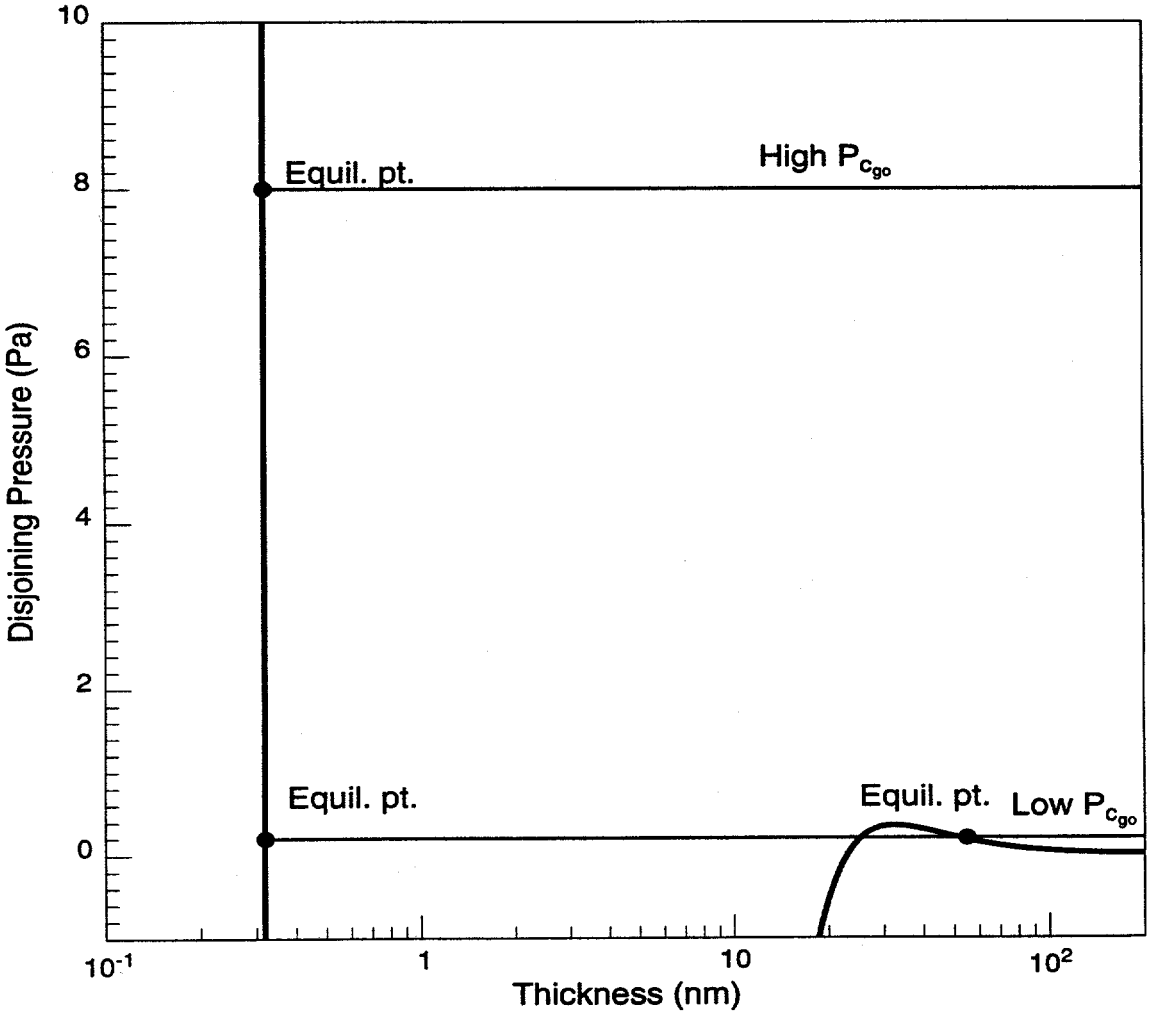

Figure 4.24: The disjoining pressure at 20°C of pentane showing stable equilibrium film thickness and how they vary with $P_{c_{go}}$.

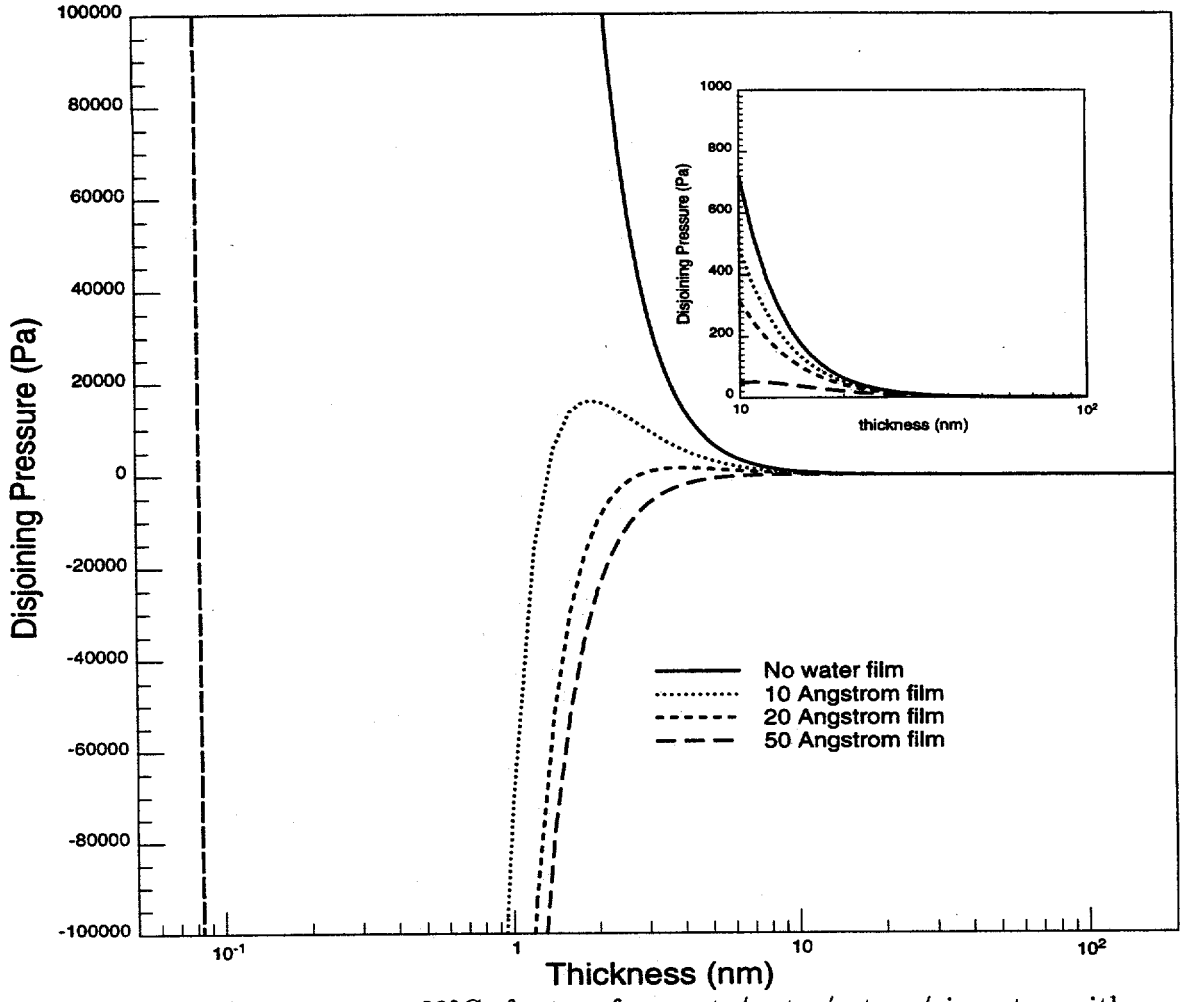

Figure 4.25: Disjoining pressure at 20°C of octane for quartz/water/octane/air system with varying water film thicknesses.

pentane, heptane, and hexane on quartz can be inferred from the calculations.

Fig. 4.25 shows the disjoining pressure of octane for various water film thicknesses. Hirasaki's [58] expression for structural force was used for Fig. 4.25. If there is no water, the disjoining pressure is always positive, and octane will wet the quartz surface in the presence of air. The same will be true of all hydrocarbons. If there is a 10 $\AA$ film of water on quartz, thick octane films from 2 nm and above can exist up to capillary pressures up to 20,000 Pa. For a 20 $\AA$ film, $P_{c_{go}}$ must be below 1,500 Pa before thick films of 20 nm and above can be found. Above the peak capillary pressures, the octane films can only be found at the small thicknesses stabilized by structural forces. Of course, an octane film must be established first before it may reside in thick films. The calculation of S^I for the curves in Fig. 4.25 indicates that octane does not spread at 20°C. However, the initial and equilibrium spreading coefficients are found to increase ($S^I = -0.7$, $S^{eq} = -1.6$ at 10 $\AA$). The smaller alkanes will be able to maintain stability at large thicknesses at higher values of $P_{c_{go}}$. In general, for a water-wet porous media, the thickness of water films on the rock grains will be greater than 50 $\AA$ due to the very strong structural forces of water [21]. Thus, the influence of the solid on the stability of the oil will be minimized, and the hydrocarbon films will most likely be of monomolecular thickness. However, for those particular cases where the water film is 20 $\AA$ or less, or non-existent, the oil film may be 1 to 100 nm thick, depending on the composition of the oil and the disjoining pressure.

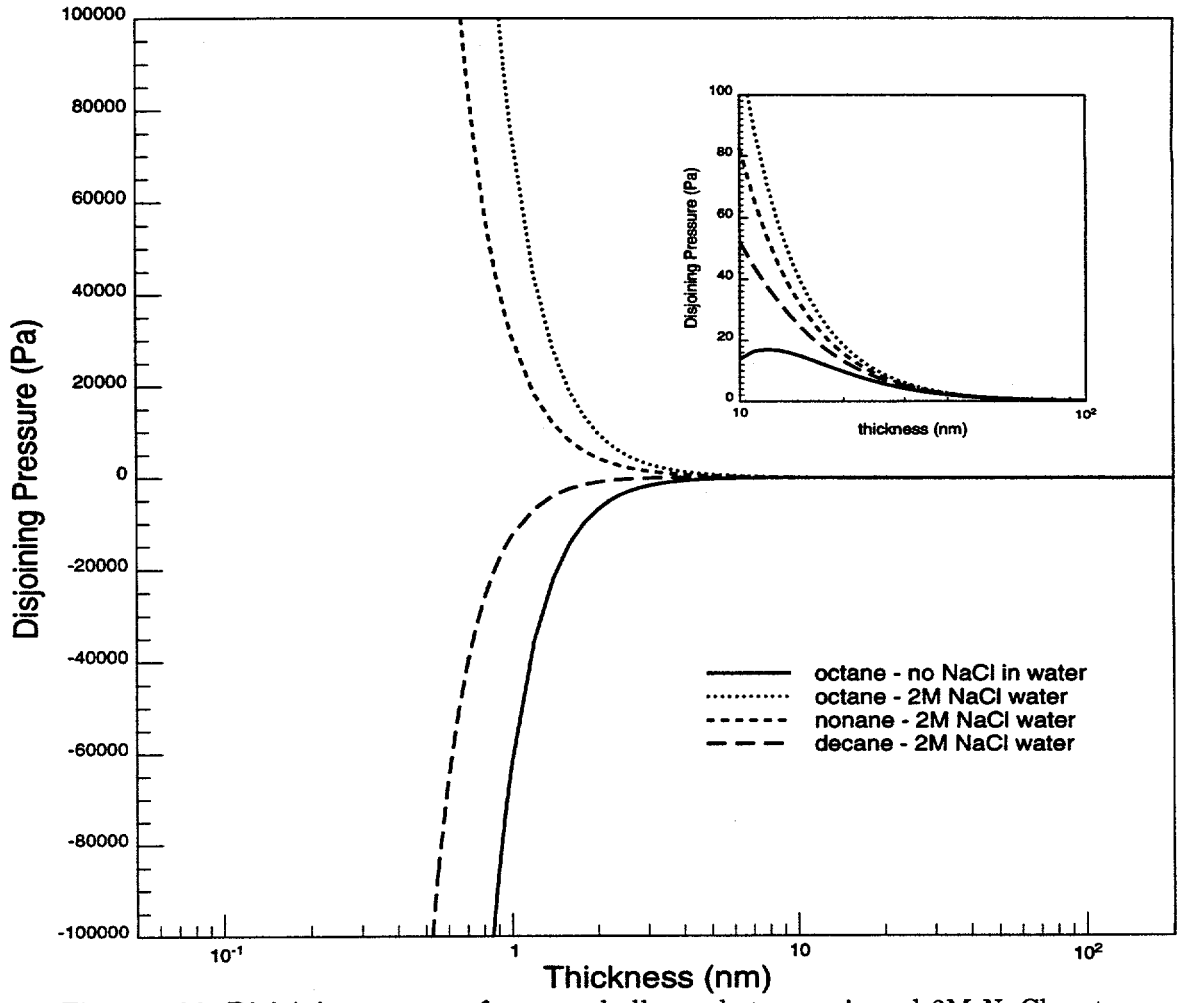

Figure 4.26: Disjoining pressure for several alkanes between air and 2M NaCl water.

4.3.5 The Influence of Salinity on Hydrocarbon Films

Richmond et al. [108] indicated that the addition of salt to water would change the dielectric permittivity. Their calculations showed that the change to $\epsilon(i\xi_n)$ results in a dramatic change of the behavior of hydrocarbon films on water. However, their expression for the dielectric permittivity used an incorrect interpolation method. Fig. 4.26 gives the disjoining pressure curve for a water/alkane/air system with 2M NaCl dissolved in the water. Note that a different expresssion for $\epsilon(i\xi_n)$ from the previous calculations is used, which tends to overestimate slightly the ability of the alkanes to maintain thick films. The results show that at 2M NaCl solution, octane forms stable, thick films of water without the influence of structural forces. The results also indicate that the initial spreading coefficient for 2M water/octane/air is positive (refer to Eq. 4.67). Thus, the addition of NaCl can significantly change the behavior of water/hydrocarbon/vapor systems. Heavy alkanes may be able to spread on water and form thick layers, which will enhance the connectivity of the oil and increase the flow of oil through the films. The calculations also show that nonane will spread and form stable layers on 2M NaCl water, though this result can be questioned because the dielectric permittivity used is not precisely known.

If more salt is added to the water, the heavier alkanes can spread and begin to form stable layers. Fig. 4.27 indicates that tetradecane can spread and form stable, thick layers, for a 4M NaCl water. Note again that this result is uncertain due to the poor description of $\epsilon(i\xi_n)$. However, the trend of increasing S^I and film stability with increasing salinity is evident.

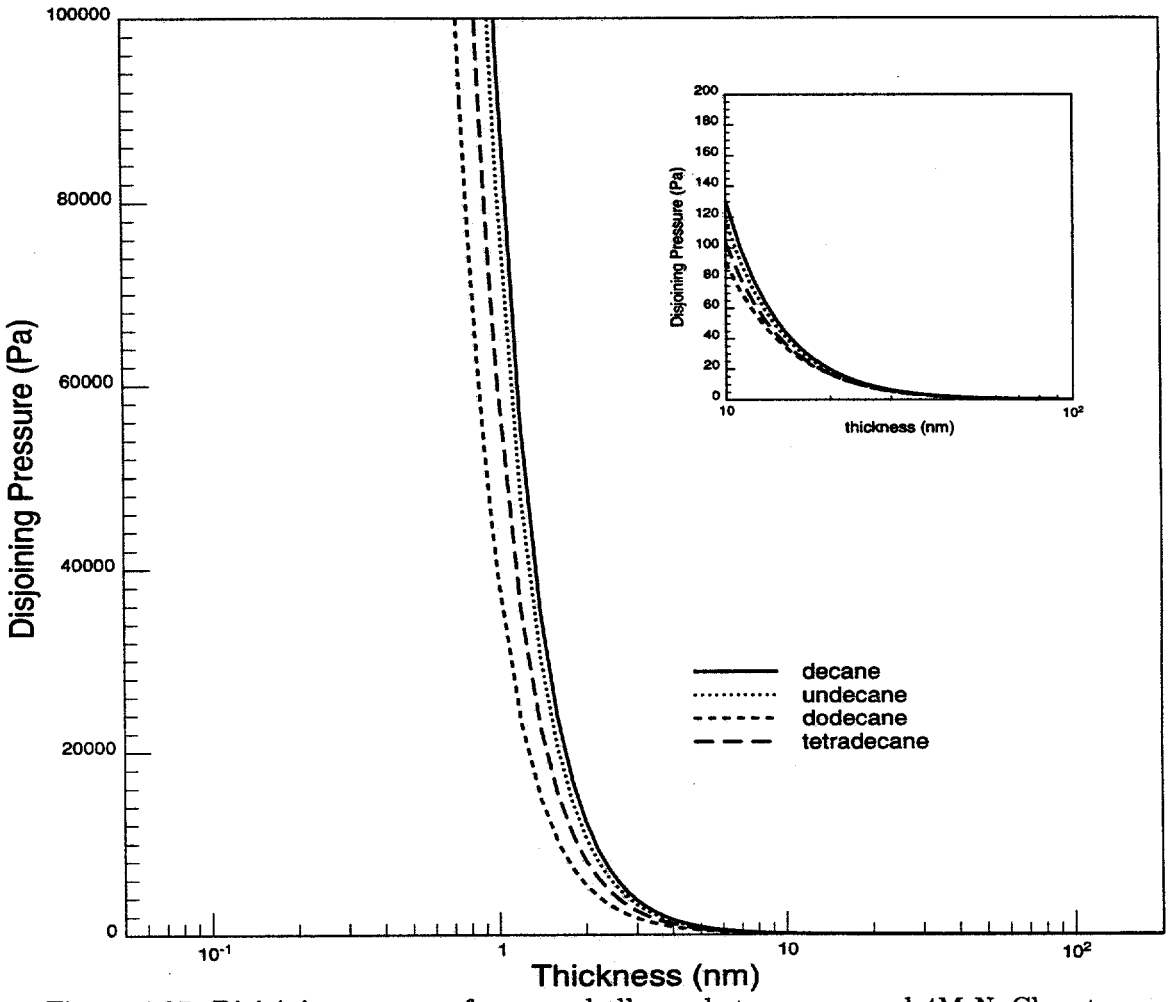

Figure 4.27: Disjoining pressure for several alkanes between gas and 4M NaCl water.

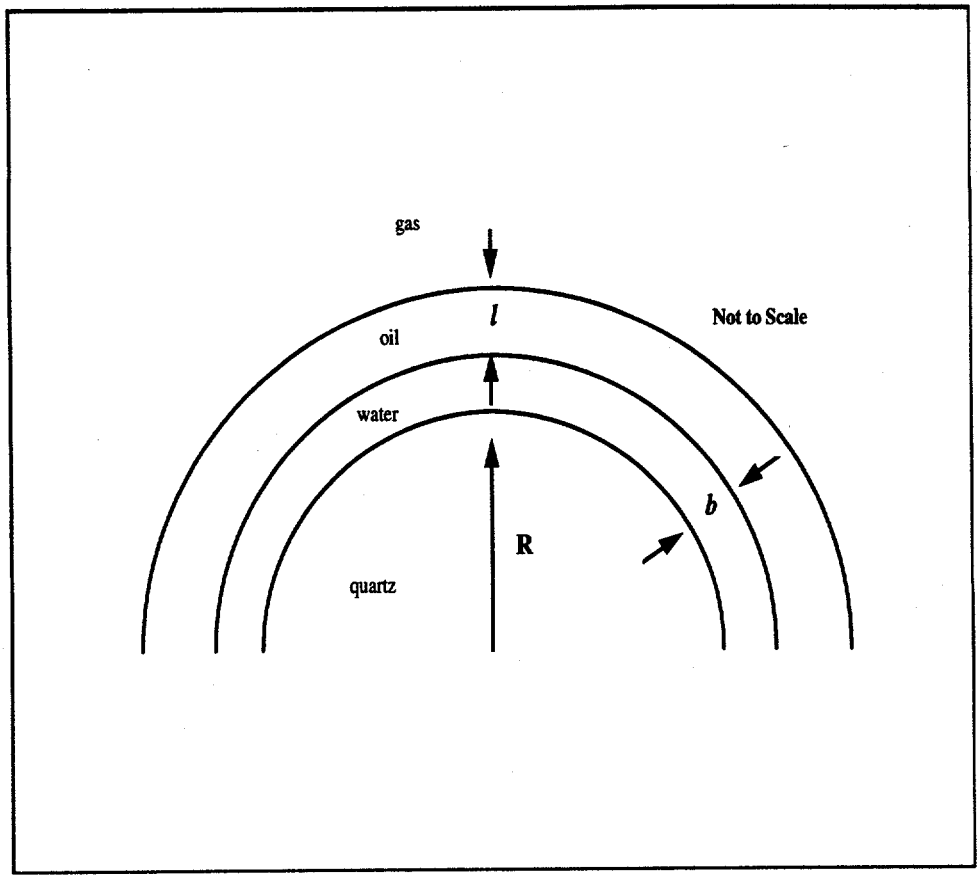

Figure 4.28: A smoothly curved quartz grain of radius R with a water layer of thickness b separated from a gas by a layer of oil.

4.3.6 The Influence of Temperature

Hirasaki [58] investigated the effects of temperature on the wetting behavior of hydrocarbons on poly(tetrafluoroethylene) (PTFE). He found that the equilibrium spreading coefficient was affected strongly by the change in temperature. S^{eq} for hexane was found to go to zero for temperatures above 60° C. The equilibrium spreading coefficient of octane increased to zero at 125 °C. S^{eq} of decane was zero at 180°C. No calculations were made for hydrocarbons on water. The behavior of hydrocarbon films upon water can be expected to be similar, but not exactly like the behavior on PTFE. More work on the influence of temperature on the spreading and stability of hydrocarbons is forthcoming.

4.3.7 The Influence of Curvature on Hydrocarbon Films

Surfaces in porous media do not resemble Fig. 4.21. Reservoir rocks are characterized by rough surfaces with many corners, crevices, edges, and protrusions. Unfortunately, equations for the disjoining pressure do not exist for such complex geometries. However, valid approximations for many smoothly curved surfaces are available. Fig. 4.28 is a depiction of a curved quartz grain with a radius of curvature R with a water film coating the surface separated from a gas by a thin film of oil. If $R \gg l$, an expression for the disjoining pressure for curved surfaces Φ can be written

as,

$$\Phi(l) = 2H\gamma_{go} + \Pi(l), \tag{4.69}$$

where $2H$ for a convex spherical quartz surface as depicted in Fig. 4.28 is,

$$2H = \frac{-2}{R + l + b}. \tag{4.70}$$

The condition for stability for the curved surface is,

$$\Phi = P_{c_{go}}, \qquad \Phi' < 0.$$

Fig. 4.29 shows the results for quartz/water/octane/air at various values for R for $\gamma_{go} = 21mN/m$ and $b = 50\mathring{A}$, using Eq. 4.70. When there is no curvature, thick, stable films can exist as evident by the inset picture. When there is a convex curvature, the disjoining pressure becomes negative until the structural interactions dominate at small thicknesses. Thus, for large thicknesses of octane to exist, the condition $P_{c_{go}} < 0$ must exist, which for reservoir conditions is unlikely. Hirasaki [57] found in his work that thick, wetting water films can be collapsed due to convex curvature of the solid substrate. This work extends this conclusion to oil films as well.

For a concave spherical curvature $2H$,

$$2H = \frac{2}{R - l - b}, \tag{4.71}$$

an increase in the stability of thick oil films is found. Fig. 4.30 demonstrates how the disjoining pressure can vary with thickness for concave surfaces. The $P_{c_{go}}$ required to reduce a thick film of octane to monomolecular size is much greater than the same film if no curvature existed. In addition, if $P_{c_{go}}$ decreases such that it falls below Φ, then the oil/gas curvature must decrease, and the concave body will fill with oil. The increase in Φ beyond 20 nm, evident for the $R = 1000$ nm curve (but existing for the other curves as well at larger thicknesses) is caused by the denominator in Eq. 4.71. Although $\Phi' < 0$, the presumption of instability is misleading. As $l \to R$, at the point where Φ' changes sign the oil will spontaneously fill the concave body (much like snap-off of water in a pore throat).

Thus, curvature of the solid surface has the effect of supporting (concave curvature) or hindering (convex curvature) the existence of large thicknesses of oil films between water and gas. One can then expect in a porous medium where oil films exist ($S^I > 0$) that in the corners and edges of the pore space, thick films of oil may be found, but over flat surfaces, protrusions, or asperities, the oil films may be only a few molecules thick. The oil film thickness will also vary with the water salinity and the temperature of the reservoir.

4.3.8 Conclusions

From the work performed, several conclusions can be drawn.

(i) The initial and equilibrium spreading coefficients for various conditions can be predicted with good accuracy given the temperature and the dielectric permittivity of the materials.

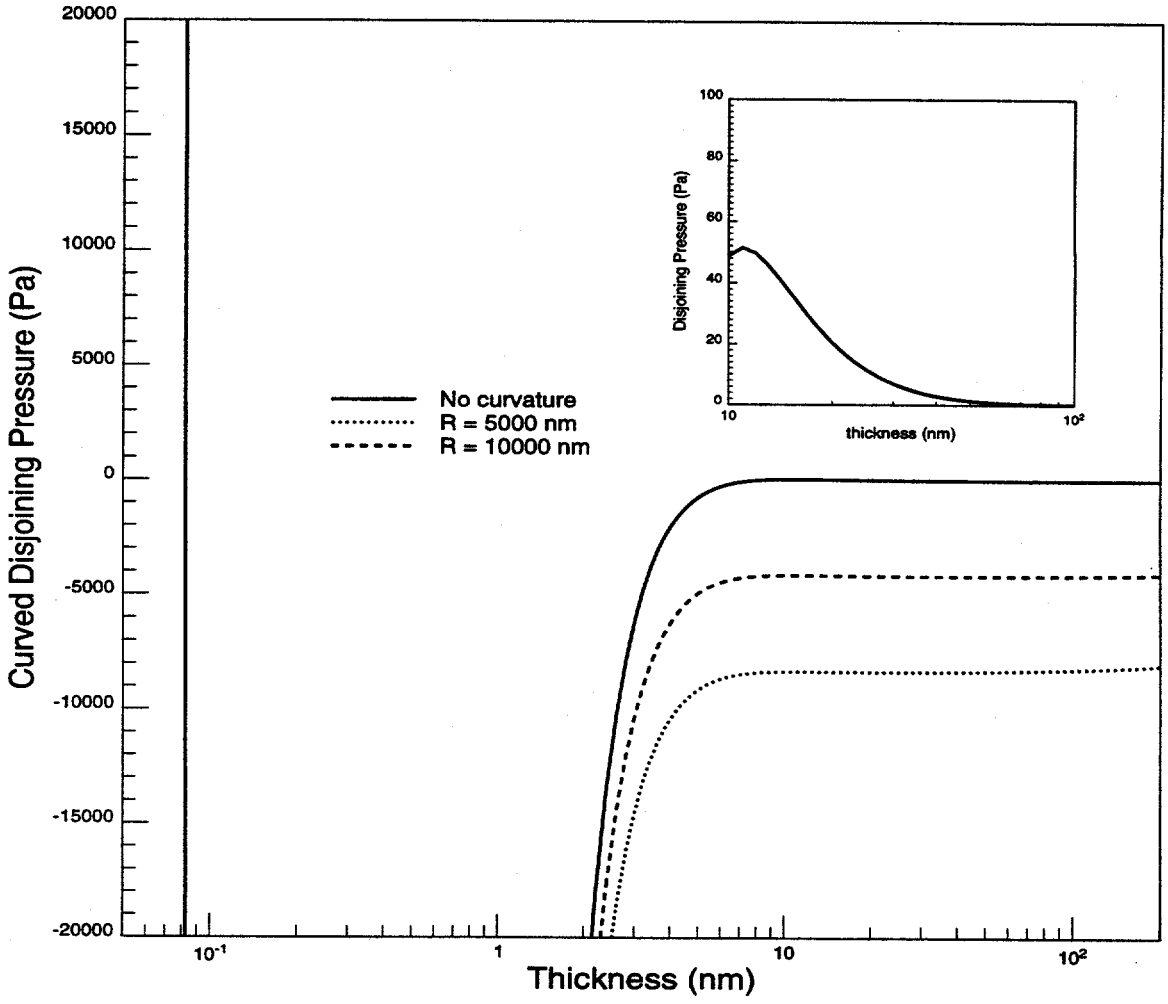

Figure 4.29: Disjoining pressure at various convex curvatures for quartz/water/octane/air system at 20°C with 50$\mathring{A}$ water thickness and $\gamma_{go} = 21mN/m$.

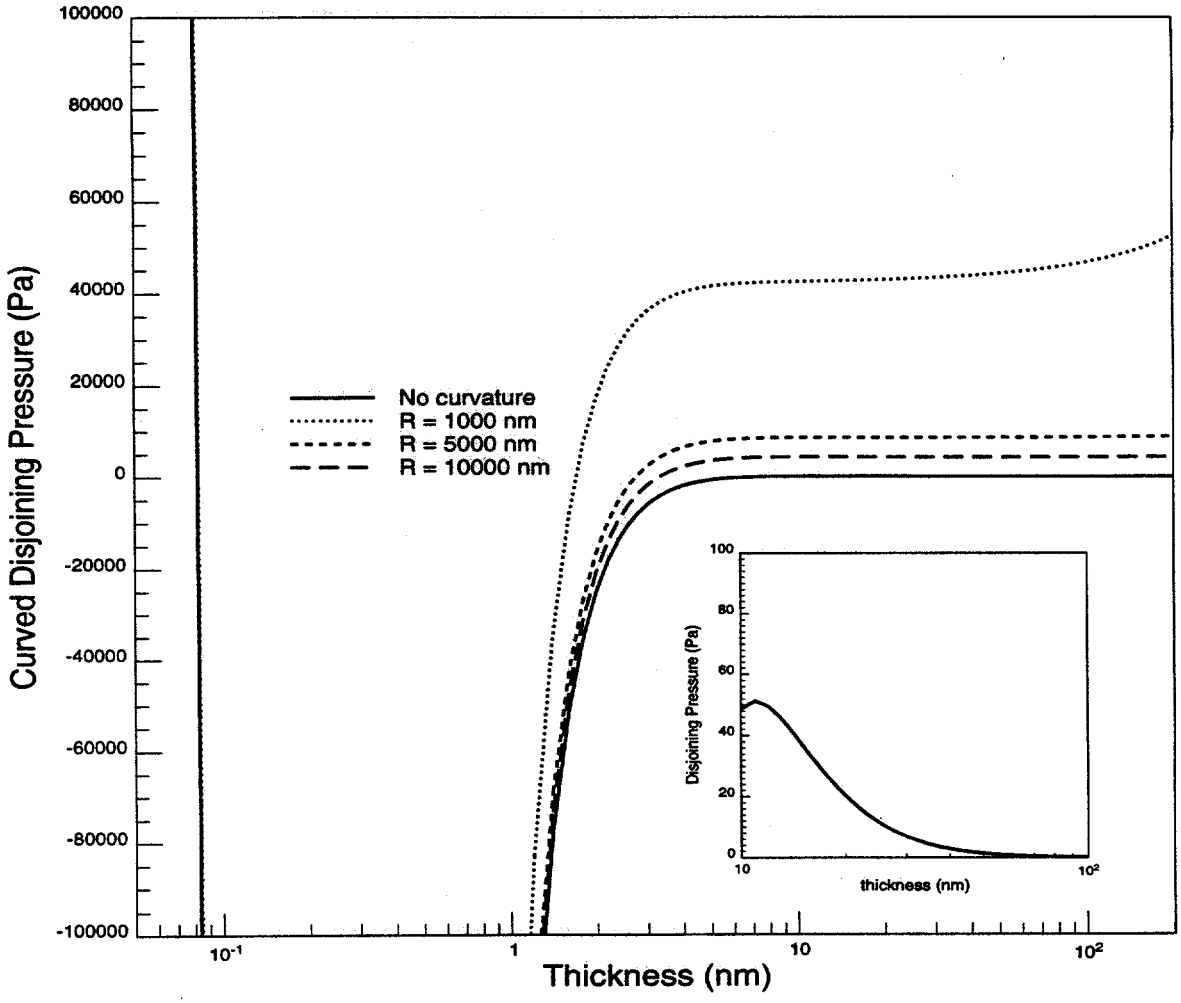

Figure 4.30: Disjoining pressure at various concave curvatures for quartz/water/octane/air system at 20°C with 50$\mathring{A}$ water thickness and $\gamma_{go} = 21mN/m$.

(ii) Pentane, hexane, heptane and benzene are predicted to spread on fresh water at 20°C. Increases in water salinity or temperature can cause heavier alkanes to spread on water. Thus, at reservoir conditions, many hydrocarbons may have a positive initial spreading coefficient between water and gas.

(iii) Hexane, heptane, and benzene will form stable layers of monomolecular thickness on fresh water at 20°C. Pentane most likely will form stable monomolecular films at those conditions, but some films of larger thickness may exist.

(iv) Increases in temperature or water salinity may allow stable, thick films of hydrocarbons to form on water. This has important consequences for the drainage of oil through thin films.

(v) If the underlying water layer becomes thin, then the intermolecular forces of the solid surface become important. The effect of the solid substrate tends to increase the spreading coefficient and the equilibrium thickness of the oil film.

4.4 Gravity Drainage of Crude Oil in the Presence of Carbon Dioxide

Dengen Zhou

Our recent experiments and theoretical analysis have demonstrated that gravity drainage at low interfacial tension could be an efficient oil recovery mechanism from vertically fractured reservoirs [111]. However, the analysis was based on experimental data from model fluid systems, such as a binary liquid mixture of C_1 and nC_7 used by Stensen et al. [116]. The question that one would ask when we apply the analysis to field design is whether the complex nature of crude oil leads to drainage behavior different from that of model systems. There is little data in the literature about crude oil drainage for injection gases that exhibit multicontact miscibility. One such gas is CO_2. In this section we report results of experiments to determine whether transfers of components between CO_2-rich and oil-rich phases can lead to gravity drainage of crude oil. We have designed an experimental apparatus to investigate the effects of the development of miscibility at various pressures and temperatures on the drainage rates and final crude oil recovery in the presence of CO_2. In this section, we report our preliminary experimental results for gravity drainage of Means/crude oil in the presence of high pressure CO_2.

When CO_2 is injected into a reservoir, mass transfer will occur between the CO_2 phase and the crude oil, because of the large solubilities of some hydrocarbon molecules in CO_2, and also the solubility of CO_2 in the crude oil. This mass exchange leads to the variations of phase properties such as interfacial tension and densities, which would alter the relative magnitudes of the gravity and capillary forces and influence the drainage rates of the oil phase. Gravity forces drain the heavier phase (crude oil) out of the rock, while capillary forces and the end effect tend to keep oil in the rock. The magnitude of gravity forces is proportional to the absolute length of the core. Therefore, relatively long cores are needed to investigate gravity drainage mechanisms in a way that is suitable for oil reservoirs. Our experimental setup was designed to use 2-ft long cores, which are significantly longer than the cores used in some past studies of gravity drainage experiments [116, 118].

4.4.1 Experimental Setup

Fig. 4.31 is a schematic of the gravity drainage apparatus. The use of a visual cell enables us to measure the volume of oil drained at any given time without disturbing the system. The

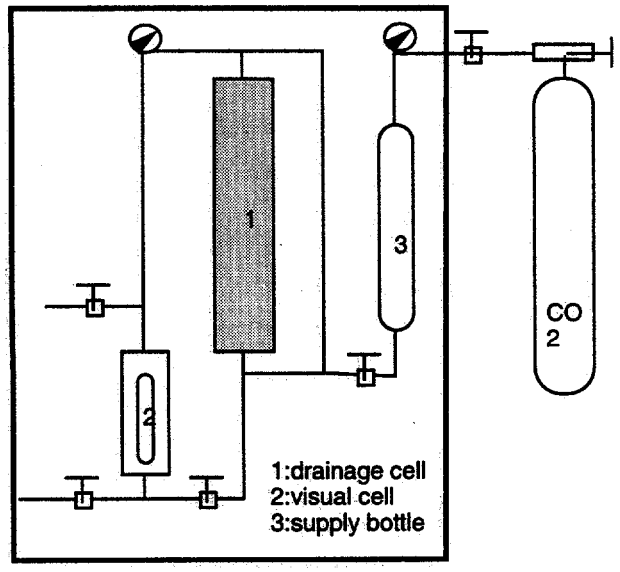

Figure 4.31: Schematic of the gravity drainage rig

drainage apparatus was designed to operate up to 7,000 psia and 200°F. Fig. 4.32 shows the inside arrangement of the drainage cell. The annular space between the core and the cell wall is about 1 mm, a space that simulates an open fracture through which oil and gas can flow. We attempted to minimize the volume ratio of this space and the rock matrix in order to observe similar mass transfer mechanisms as in oil reservoirs. The inside dimensions of the drainage cell are height of 2 ft and a diameter of 2.5 in. In order to avoid oil displacement when gas flows into the cell, the cell was designed to allow gas flow into the cell from both ends.

Means stock tank crude was used for our preliminary studies, because it has been relatively well characterized in our laboratory [117, 50].

4.4.2 Experimental Procedures

Because we are using stock tank oil, we can saturate cores at room temperature and pressure. We first saturated the core with water by evacuating it and then allowing water to imbibe into the core. Weighing the core before and after saturation gave the pore volume. The core was then moved into the core holder for oil displacements to establish initial water saturation. We considered the initial water saturation to be reached after injection of 1.5 pore volume of crude oil, at which time the water production was small although it had not completely stopped. The amount of water produced was used to calculate oil saturation. The core was then weighed again to check the material balance.

The cell and CO_2 were then preheated to the desired temperature before inserting the saturated core into the drainage cell. The core was kept in the drainage cell for two days before the introduction of CO_2 in order to be sure that temperature equilibrium was achieved in the drainage cell.

Pure CO_2 was then introduced into the cell to replace the oil in the annulus. At present stage, the pressure in the cell is controlled manually by periodically introducing additional CO_2 into the cell. However, we are in the process of modifying the system to keep the pressure constant automatically.

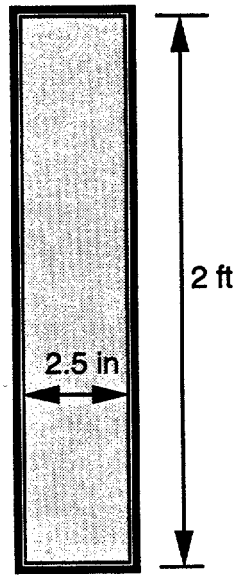

Figure 4.32: Schematic of the gravity drainage cell

The difference in density between the CO_2 and the oil creates a gravity driving force for oil drainage. That force is opposed by capillary forces which depend on the interfacial tension of the gas/oil system. That interfacial tension changes as components transfer between the phases and the oil swells as the CO_2 dissolves in it. Thus, the experiment determines whether the component transfers lead to significant recovery of crude oil.

4.4.3 Results

We have conducted two drainage experiments at different temperatures and pressures. Fig. 4.33 shows the crude oil recovery curves. Experiment 1 was performed at room temperature (72.5 °F) and relatively low pressure (900 psi) in a 500 md sandstone core. After three weeks of drainage, there was about 27% of original oil in place (OOIP) recovered. The experiment was stopped after six weeks of drainage. There was little additional oil recovered in the last three weeks. No additional oil was recovered when we blew down the system to ambient pressure. The calculations of the phase properties presented below show that the interfacial tension was relatively high (about 4.0 mN/m). Therefore, this low recovery is not surprising.

In experiment 2, the temperature was elevated to 120°F, and the pressure was kept at 1500 psia for the first five weeks and jumped to 1700 psia in the last week of the experiment. Two recovery periods were observed in this experiment. Drainage was fast in the first week of drainage, and then it slow down in the remaining four weeks. That behavior is consistent with the observations of Schechter et al.[111]. Comparison of experiments 1 and 2 suggests that gravity drainage is faster and more efficient at the higher temperature and pressure. At same temperature, we recovered additional 6 % OOIP when the pressure was increased from 1500 psia to 1700 psia. This additional recovery indicates that gravity drainage at high pressure is more efficient in the pressure range of the experiments, presumably because interfacial tension was lower at the higher pressure, and because solubility of CO_2 in the oil increased somewhat. Experiment 2 was terminated by blowing down the pressure from 1700 psia to ambient pressure in about 20 minutes. We collected additional 5% of oil with a lighter color than the crude oil. Thus, we recovered 50% of OOIP from experiment 2.

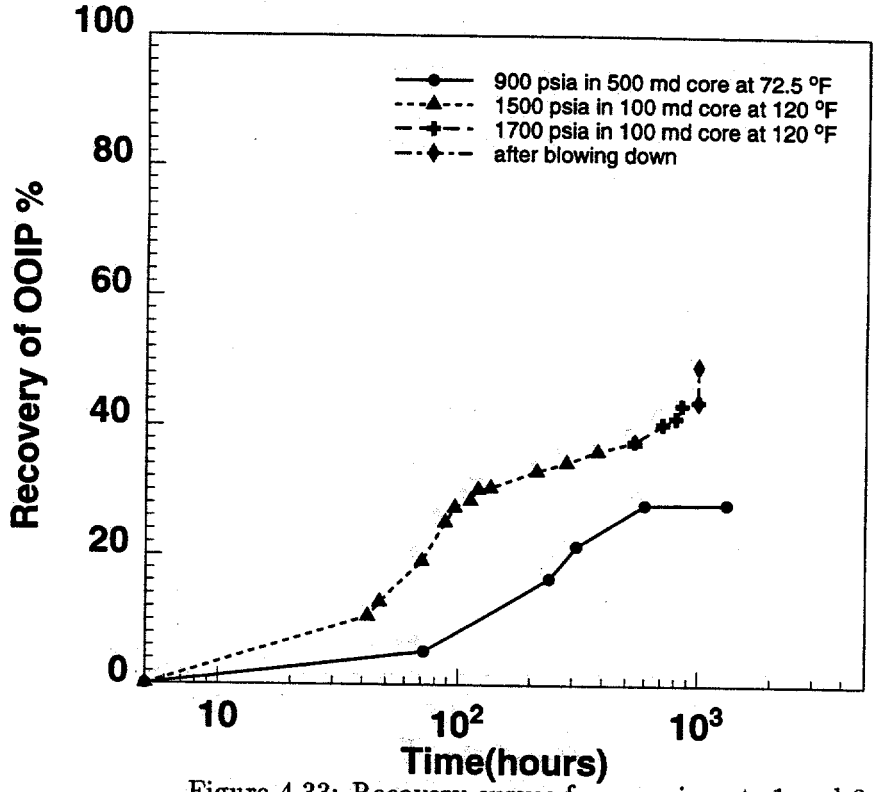

Figure 4.33: Recovery curves for experiments 1 and 2

4.4.4 Discussion

Oil recovery from gravity drainage is the result of interactions between capillary forces created by interfacial tension and gravity forces from the density difference of the gas and oil phases. The relative magnitudes of capillary and gravity forces determine the efficiency of a drainage process. The ratio of the capillary to gravity forces can be represented by the inverse Bond number N_B^{-1}, defined here as

$$N_B^{-1} = \frac{c\sigma\sqrt{\frac{\phi}{k}}}{\Delta\rho g H} \tag{4.72}$$

where c is a scaling constant for a given medium (c is about 0.2 for most of the media), σ is interfacial tension, $\Delta\rho$ is the density difference between oil and gas phases, k and ϕ are the permeability and porosity of the medium, and H is the height of the core.

Fayers and Zhou [42] proposed the following equation to correlate the remaining oil saturation (S_{rm}) at the end of a drainage process to the corresponding value of N_B^{-1} by scaling the capillary pressure curves.

$$S_{rm} = N_B^{-1}\left(2 - N_B^{-1}\right)(1 - S_{or}) + S_{or} \tag{4.73}$$

where S_{or} is the irreducible oil saturation. They used 0.25 as S_{or} in correlating their experimental data collection.

To estimate the corresponding values of N_B^{-1} for our experiments, we performed calculations of the phase properties for the Means/CO_2 system. The Peng-Robinson equation of state (PR-EOS) was used to calculate phase densities. Interfacial tensions were calculated with the Parachor methods. Detailed compositions of stock tank Means reported by Stessman [117] were used in these calculations. Figs. 4.34 and 4.35 show the calculated densities and interfacial tensions of the oil-rich and CO_2-rich phase at 72.5°F and various pressures. Figs. 4.36 and 4.37 show the same calculation for the high temperature and pressure experiment. Our calculations indicate that the interfacial tensions were not ultra-low (10^{-3} mN/m) but were about 1 mN/m. Using $\sigma = 4.0$ mN/m, $\Delta\rho =$

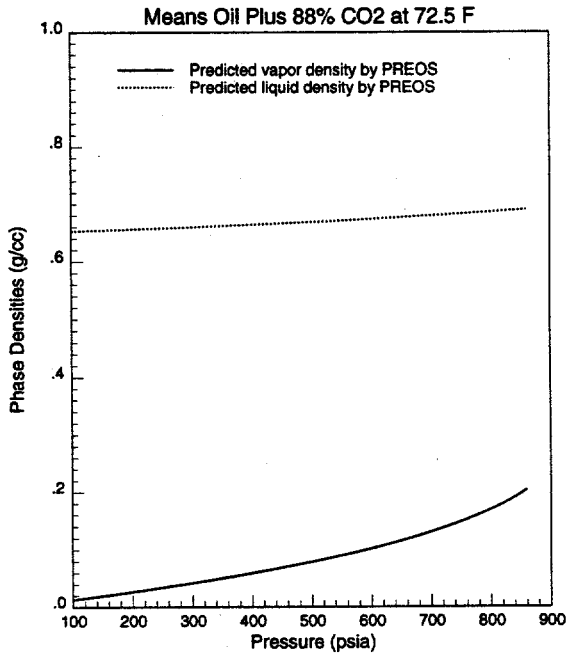

Figure 4.34: Calculated densities of Means/CO_2 mixture at 72.5°F and various pressures

400 kg/m^3 for experiment 1 and $\sigma = 0.5\ mN/m$, $\Delta\rho = 180$ kg/m^3 for experiment 2, we obtained the corresponding N_B^{-1} values as 0.23 and 0.14 for experiments 1 and 2 respectively. Fig. 4.38 shows the comparison of the two experiments and the correlation proposed by Fayers and Zhou. Although the remaining oil saturation is slightly larger than the correlation, the trend agrees well with the earlier comparisons.

The recovery results shown in Fig. 4.38 suggest that substantial recovery of oil from fractured reservoirs is possible by CO_2 injection. If fracture heights larger than 2 ft exist, for example, inverse Bond numbers will be lower still and better recovery efficiency can be expected. Furthermore, if the porous medium is not strongly water wet, then injection of water will yield poor recovery, because imbibition will be relatively inefficient. Even if the porous medium is water wet, the film drainage mechanisms discussed in this chapter can lead to improved recovery after water injection. Thus, there is considerable evidence that the use of gas injection processes in fractured reservoirs should be investigated further.

4.4.5 Conclusions

From the preliminary experimental results and calculations of the phase properties of Means/CO_2 systems, we draw the following conclusions.

(i) Crude oil can be efficiently recovered by gravity drainage in the presence of CO_2 at relatively low pressure (1500 psia), in which the interfacial tension between oil and CO_2 rich phase is not necessarily ultra-low.

(ii) Final crude oil recovery can be related to the inverse Bond number of the model systems, although the Means/CO_2 fluids were not pre-equilibrated.

(iii) Additional oil can be recovered by blowing down the system pressure after a drainage process, and the recovered oil is lighter than the original crude oil.

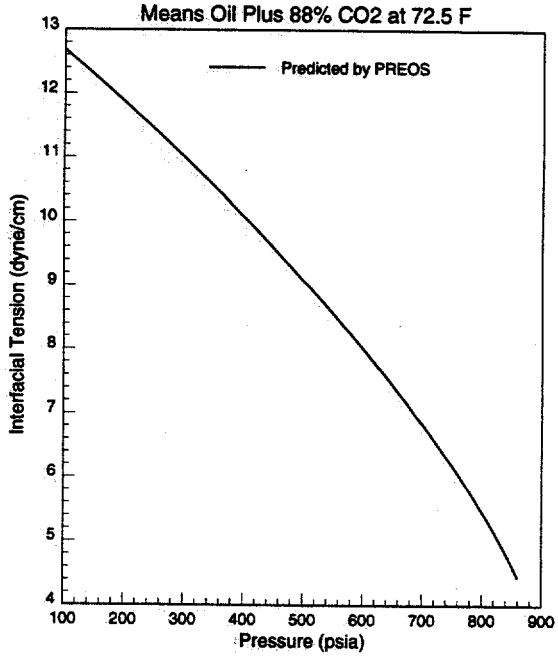

Figure 4.35: Calculated interfacial tension of Means/CO_2 mixture at 72.5°F and various pressures

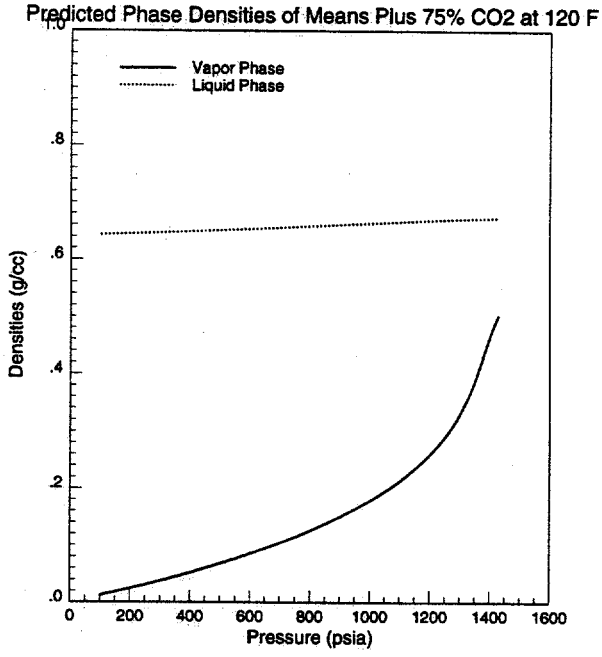

Figure 4.36: Calculated densities of Means/CO_2 mixture at 120°F and various pressures

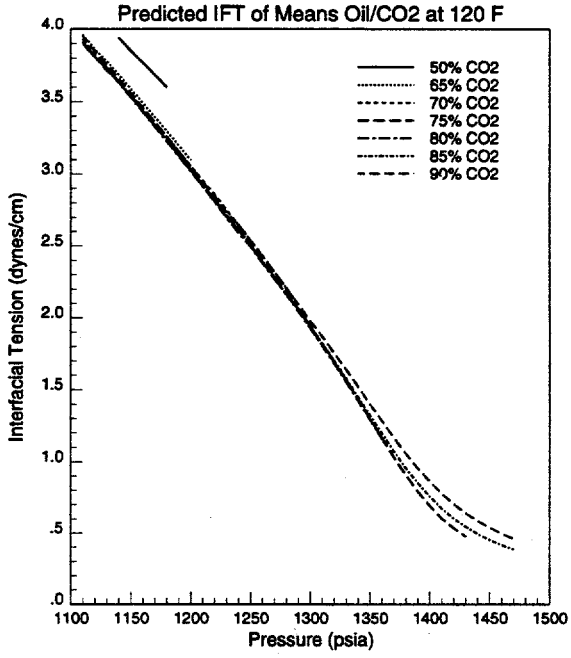

Figure 4.37: Calculated interfacial tension of Means/CO_2 mixture at 120°F and various pressures

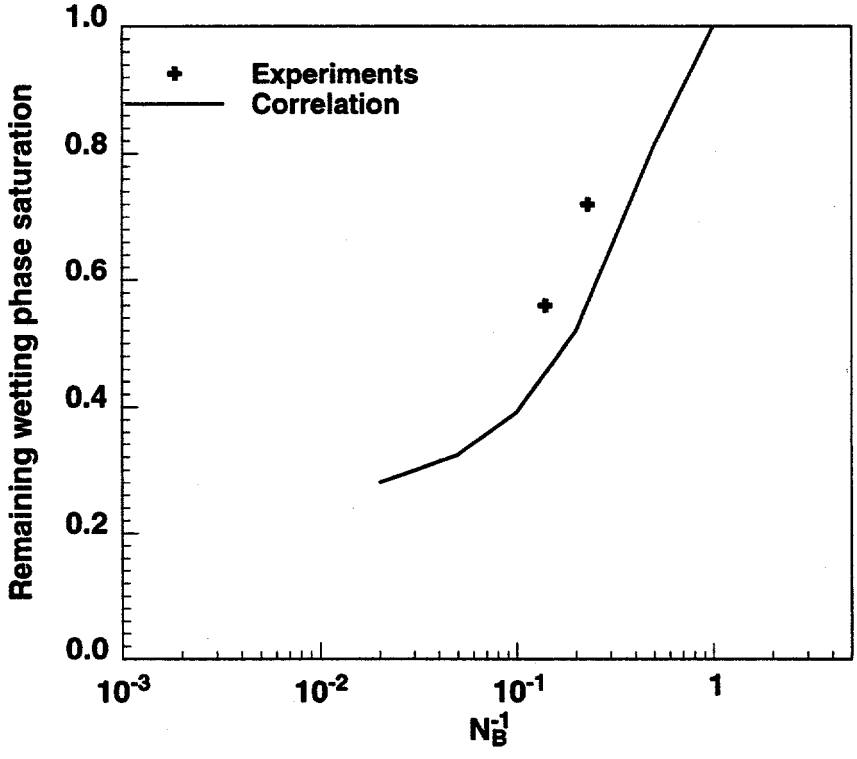

Figure 4.38: Correlation of the remaining crude oil saturation with the inverse Bond numbers

5. Summary

This report outlines research results in three areas:

(1) representation by streamtube method of displacement processes in heterogeneous reservoirs,

(2) improved methods for rigorous calculation of minimum miscibility pressure for multicomponent systems, and

(3) improved understanding of the interplay of gravity, viscous and capillary forces that control formation of residual oil saturations.

The computational approach described in the first area builds on much previous work on use of streamtubes to describe flow in heterogeneous reservoirs. The approach used here combines updating of streamtubes, which represents the effects of mobilities that changes as the displacements proceed, with use of a one-dimensional representation of flow within a streamtube. The one-dimensional flow solution contains all the representation of the physical mechanisms. For example, compositional effects of phase behavior can be represented in the one-dimensional solution. The decoupling of the representation of local displacement process mechanisms from the calculations of the effects of heterogeneities means that predictions of process performance with orders of magnitude less computer time than is required for conventional finite difference simulations. While the approach is certainly an approximation, the examples given suggest that the errors associated with the approximation are not severe. Indeed, the fact that the method is not affected by numerical dispersion is a significant advantage.

The procedure outlined in area (2) for calculation of minimum miscibility pressures or enrichments (MMP's or MME's) is a significant step toward the formulation of a completely rigorous method for calculation of the conditions required for multicontact miscibility for multicomponent systems. In addition, the analysis given of the mathematical structure of the coupling of multicomponent phase equilibrium with multiphase flow points the way toward completion of the multicomponent theory. That theory demonstrates clearly the limitations of development of miscibility that rely on use of ternary phase behavior.

In area (3) we report results of a wide-ranging investigation of the fundamentals of multiphase flow in which gravity, capillary, and viscous forces interact to determine displacement process performance. In particular, we focus on the conditions required for the formation of films of oil between gas and water, because those films provide flow paths for oil that are essential if oil saturations are to be reduced to low values. It is understanding of those mechanisms that will enable us to design gas injection processes that create the conditions required for efficient displacement of oil by gas in the presence of water. Finally, we report the first results from experiments to demonstrate that gravity drainage of crude oil can be obtained using high pressure CO_2. The preliminary results give us confidence that appropriately designed gas injection processes can lead to significant recovery of oil from fractured reservoirs.

The results discussed in this report are but part of a broad-ranging examination of the scaling of the physical mechanisms that control displacement performance in gas injection processes. The work in progress includes experiments to delineate physical mechanisms and test models, and simulations to explore combinations of physical mechanisms that are difficult or impossible to study experimentally. Predictions of process performance at field scale will inevitably make use of simulation. It is the goal of this project to make those simulation predictions based on analysis of the physics of the flow rather than on empirical models that may not represent scaling behavior

accurately. Therefore, a significant part of the research effort is aimed at fundamental description of the capillary, gravity and viscous-driving forces that move multicomponent fluids and phases in heterogeneous reservoirs. It will be improvements in understanding of the scales on which those mechanisms operate that give us the tools we need to design more effective recovery processes for very heterogeneous reservoirs.

References

[1] Abbaszadeh-Dehghani, M.: *Analysis of Unit Mobility Ratio Well-to-Well Tracer Flow to Determine Reservoir Heterogeneity*, PhD dissertation, Stanford University (December 1982).

[2] Abrams, A.: "The Influence of Fluid Viscosity, Interfacial Tension, and Flow Velocity on Residual Oil Saturation Left by Waterflood," *Soc. Pet. Eng. J.* (1975) **14**, 927–935.

[3] Adamson, A. A.: *Physical Chemistry of Surfaces*, John Wiley & Sons, Inc., New York (1990).

[4] Aleonard, B.: "Criticality Conditions and Minimum Miscibility Pressure for Four-Component Gas Drives," Master's thesis, Stanford University, Stanford, CA (1994).

[5] Araktingi, U.G. and Orr, F.M., Jr.: "Viscous Fingering in Heterogeneous Porous Media," *SPE Advanced Technology Series* (1993) **1**, No. 1, 71–80.

[6] Arya, A., Hewett, T.A., Larson, R.G., and Lake, L.W.: "Dispersion and Reservoir Heterogeneity," *SPE Reservoir Engineering* (February 1988) 139–148.

[7] Bear, J.: *Dynamics of Fluids in Porous Media*, American Elsevier, New York (1972).

[8] Bedrikovetsky, P. and Chumak, M.: "Riemann Problem for Two-Phase Four- and More-component Displacement (Ideal Mixtures)," (June 1992) Third European Conference on the Mathematics of Oil Recovery, Delf, Netherlands.

[9] Blunt, M., King, M.J. and Scher, H.: "Simulation and Theory of Two-Phase Flow in Porous Media," *Phys. Rev. A* (1992) **46**, No. 12, 7680–7698.

[10] Blunt, M.J.: "Oil Films and Three Phase Flow in Porous Media," unpublished (1993).

[11] Blunt, M.J., Fenwick, D. and Zhou, D.: "What Determines Residual Oil Saturation in Three Phase Flow?," paper SPE 27816 presented at the 1994 Ninth Symposium on Improved Oil Recovery, Tulsa, OK, April.

[12] Blunt, M.J., Zhou, D., and Fenwick, D.H.: "Three Phase Flow and Gravity Drainage in Porous Media," to be published in *Transport in Porous Media* (1994).

[13] Bommer, M.P. and Schechter, R.S.: "Mathematical Modeling of In-Situ Uranium Leaching," *Society of Petroleum Engineers Journal* (December 1979) 393–400.

[14] Bratvedt, F., Bratvedt, K., Buchholz, C.F. et al.: "A New Front-Tracking Method for Reservoir Simulation," paper SPE 19805 presented at the 1989 64th SPE Annual Technical Conference and Exhibition, San Antonio, TX, October.

[15] Brooks, R. H. and Corey, A. T.: "Properties of Porous Media Affecting Fluid Flow," *Irrigation and Drainage Division of the ASCE Journal* (1966) **92**, 61–88.

[16] Buckley, S.E. and Leverett, M.C.: "Mechanism of Fluid Displacement in Sands," *Trans., AIME* (1941) **249**, 107–116.

[17] Chatzis, I. and Morrow, N.R.: "Correlation of Capillary Number Relationships for Sandstone," *Soc. Pet. Eng. J.* (October 1984) **5**, 555–562.

[18] Chatzis, I., Kantzas, A. and Dullien, F. A. L.: "On the Investigation of Gravity-Assisted Inert Gas Injection Using Micromodels, Long Berea Sandstone Cores, and Computer-Assisted Tomography," paper SPE 18284 presented at the 1988 SPE Annual Technical Conference and Exhibition, Houston, TX, October 2–5.

[19] Christie, M.A. and Bond, D.J.: "Multidimensional Flux Corrected Transport for Reservoir Simulation," paper SPE 13505 presented at the 1985 Symposium on Reservoir Simulation, Dallas, TX, February.

[20] Christie, M.A., Muggeridge, A.H. and Barley, J.J.: "3D Simulation of Viscous Fingering and WAG Schemes," *Soc. Pet. Eng. Res. Eng.* (February 1993) 19–26.

[21] Churaev, N.V. and Derjaguin, B.V.: "Inclusion of Structural Forces in the Theory of Stability of Colloids and Films," *J. Colloid & Interface Sci.* (February 1985) **103**, 542–553.

[22] Corey, A. T.: *Mechanics of Immiscible Fluids in Porous Media*, Water Resources Publications, Littleton, CO (1986) 253.

[23] Dagan, G.: "Time–Dependent Macrodispersion for Solute Transport in Anisotropic Heterogeneous Aquifers," *Water Resources Research* (September 1988) **24**, No. 9, 1491–1500.

[24] Dake, L.P.: *Fundamentals of Reservoir Engineering*, Elsevier Scientific Publishing Company (1978).

[25] de Gennes, P.G.: "Wetting: statics and dynamics," *Reviews of Modern Physics* (July 1985) **57**, 827–853.

[26] Del Cerro, C. and Jameson, G.J.: "The Behavior of Pentane, Hexane, and Heptane on Water," *J. Colloid & Interface Sci.* (December 1980) **78**, 362–375.

[27] Derjaguin, B. v. and Kussakov, M. M.: "Anomalous Properties of Thin Polymolecular Films V," *Acta Physicochim URSS* (1939) **10**, 25.

[28] Derjaguin, B.V., Churaev, N.V., and Muller, V.M.: *Surface Forces*, first edition, Consultants Bureau, New York (1987).

[29] Dindoruk, B.: *Analytical Theory of Multiphase, Multicomponent Displacement in Porous Media*, PhD dissertation, Stanford University, Stanford, CA (1992).

[30] Dindoruk, B., Johns, R.T. and Orr, F.M., Jr.: "Analytical Solution for Four Component Gas Displacements with Volume Change on Mixing," (June 1992) Third European Conference on the Mathematics of Oil Recovery, Delft, Holland.

[31] Dong, M., Dullien, F.A.L., and Chatzis, I.: "Imbibition of Oil in Film Form over Water Present in Edges of Capillaries with an Angular Cross-Section," submitted to J. Colloid Interface Sci. (1994).

[32] Dougherty, E. and Sheldon, J.: "The Use of Fluid-Fluid Interfaces to Predict the Behavior of Oil Recovery Processes," *Society of Petroleum Engineers Journal* (June 1964) 171–182.

[33] Doyle, R.E. and Wurl, T.M.: "Stream Channel Concept Applied to Waterflood Performance Calculations For Multiwell, Multizone, Three-Component Cases," *Journal of Petroleum Technology* (March 1971) 373–380.

[34] Dullien, F. A. L.: *Porous Media, Fluid Transport and Pore Structure*, Academic Press, San Diego (1992).

[35] Dumoré, J.M. and Schols, R.S.: "Drainage Capillary Pressure Functions and the Influence of Connate Water," *Soc. Pet. Eng. J.* (1974) 437–444.

[36] Dumoré, J.M. Hagoort, J. and Risseeuw, A.S.: "An Analytical Model for One-Dimensional, Three-Component Condensing and Vaporizing Gas Drives," *Soc. Pet. Eng. J.* (April 1984) **24**, 169–179.

[37] Dzyaloshinskii, I. E., Lifshitz, E. M. and Pitaevskii, L. P.: "The General Theory of Van Der Waals Forces," *Advances in Physics* (1961) **10**, 165–209.

[38] Emanuel, A.S., Alameda, G.K., Behrens, R.A., and Hewett, T.A.: "Reservoir Performance Prediction Methods on Fractal Geostatistics," *SPE Reservoir Engineering* (August 1989) 311–318.

[39] Fatt, I.: "The Network Model of Porous Media I: Capillary Pressure Characteristics," *Petr. Trans., AIME* (1956) **207**, 144–159.

[40] Fatt, I.: "The Network Model of Porous Media II: Dynamic Properties of a Single Size Tube Network," *Petr. Trans., AIME* (1956) **207**, 160–163.

[41] Fatt, I.: "The Network Model of Porous Media III: Dynamic Properties of Networks with Tube Radius Distribution," *Petr. Trans., AIME* (1956) **207**, 164–170.

[42] Fayers, F. J. and Zhou, D.: "On the Importance of Gravity and three-Phase Flow in Gas Displacement processes," To be presented at the Petroleum Science and Tchnology Institue Conference on Advances in Reservoir Technology, London.

[43] Garnes, J.M., Mathisen, A.M., Scheie, A. and Skauge, A.: "Capillary Number Relations for Some North Sea Reservoir Sandstones," presented at the 1990 SPE/DOE Seventh Symposium on Enhanced Oil Recovery, Tulsa, OK, April.

[44] Gauglitz, P.A., Laurent, C.M. St. and Radke, J.C.: "Experimental Determination of Gas Bubble Breakup in a Constricted Cylindrical Capillary," *Ind. Eng. Chem. Res.* (April 1988) No. 17340, 27–31.

[45] Gelhar, L.W. and Axness, C.L.: "Three-Dimensional Stochastic Analysis of Macrodispersion in Aquifers," *Water Resources Research* (1983) **19**, No. 1, 161–180.

[46] Gibbs, J. W.: *The Collected Works of J. Willard Gibbs*, Longmans, Green, New York (1928).

[47] Gibbs, J.W.: "On the Equilibrium of Heterogeneous Substances, Part 1," *Connecticut Acad. Transactions (1876), reprinted in The Scientific Papers of J. Willard Gibbs, Dover, NY* (1961) **1**.

[48] Glimm, J., Lindquist, B., McBryan, O.A., Plohr, B., and Yaniv, S.: "Front Tracking for Petroleum Simulation," paper SPE 12238 presented at the 1983 Reservoir Simulation Symposium, San Francisco, CA, November.

[49] Gorell, S.: "Outlook for Calibration of Large Grid–Block Models for Miscible Flooding Applications," paper SPE 24186 presented at the 1992 1992 SPE/DOE Eight Symposium on Enhanced Oil Recovery, Tulsa, OK, April.

[50] Hagedorn, K.: *Component Partitioning in CO_2/Crude Oil Mixtures*, PhD dissertation, Stanford University (1992).

[51] Heidemann, R.A. and Khalil, A.M.: "The Calculation of Critical Points," *AIChE Journal* (1980) **26**, No. 5, 769–779.

[52] Helfferich, F.G.: "Theory of Multicomponent, Multiphase Displacement in Porous Media," *Soc. Pet. Eng. J.* (February 1981) **271**, 51–62.

[53] Hewett, T. and Behrens, R.: "Scaling Laws in Reservoir Simulation and Their Use in a Hybrid Finite Difference/Streamtube Approach to Simulation the Effects of Permeability Heterogeneity," *Reservoir Characterization, II*, L. Lake and J. Carroll, H.B. (eds.), Academic Press, Inc., London (1991).

[54] Higgins R.V. and Leighton, A.J.: "A Computer Method to Calculate Two–Phase Flow in Any Irregularly Bounded Porous Medium," *Journal of Petroleum Technology* (June 1962) 679–683.

[55] Higgins R.V. and Leighton, A.J.: "Computer Prediction of Water Drive of Oil and Gas Mixtures Through Irregularly Bounded Pororus Media — Three-Phase Flow," *Journal of Petroleum Technology* (September 1962) 1048–1054.

[56] Higgins, R.V., Boley, D.W., and A.J. Leighton: "Aids to Forecasting The Performance of Water Floods," *Journal of Petroleum Technology* (September 1964) 1076–1082.

[57] Hirasaki, G. J.: "Modeling the Effects of Trapping and Water Alternate Gas (WAG) Injection on Tertiary Miscible Displacements," paper SPE 17367 presented at the 1988 Sixth Symposium on Enhanced Oil Recovery, Tulsa, OK, April.

[58] Hirasaki, G.J.: "Structural interactions in the wetting and spreading of van der Waals fluids," *J. Adhesion Sci. Technol.* (1993) **7**, No. 3, 285–322.

[59] Hough, D. B. and White, L. R.: "The Calculation of Hamaker Constants from Lifshitz Theory with Applications to Wetting Phenomena," *Advances in Colloid and Interface Science* (1980) **14**, 3–41.

[60] Israelachvili, J.: *Intermolecular and Surface Forces*, second edition, Academic Press (1992).

[61] Johansen, T.: *Riemann Problems for Hyperbolic Systems of Conservation Laws Modeling Multicomponent, two-Phase Flow Through Porous Media*, PhD dissertation, University of Oslo, Oslo, Norway (1992).

[62] Johansen, T.: "Shocks and Simple Waves," (1992) In Skiaeveland, S. M. and Leppe, J., editor, *Recent Advances in Improved Oil Recovery Methods for North Sea Sandstone Reservoirs.* Norwegian Petroleum Directorate, Savanger.

[63] Johansen, T., and Winther, R.: "The Solution of the Riemann Problem for a Hyperbolic System of Conservation Laws Modeling Polymer Flooding," *SIAM J. Math. Anal.* (May 1988) **19**, 541–566.

[64] Johansen, T., and Winther, R.: "The Riemann Problem for Multicomponent Polymer Flooding," *SIAM J. Math. Anal.* (1989) **20**, 909–929.

[65] Johansen, T. and Winther, R.: "Mathematical and Numerical Analysis of a Hyperbolic System Modeling Solvent Flooding," (September 1990) Second European Conference on the Mathematics of Oil Recovery, France.

[66] Johns, R.T.: *Analytical Theory of Multicomponent Gas Drives With Two-Phase Mass Transfer*, PhD dissertation, Stanford University, Stanford, CA (1992).

[67] Johns, R.T., B. Dindoruk, and Orr, F.M. Jr.: "Analytical Theory of Combined Condensing/Vaporizing Gas Drives," paper SPE 24112 presented at the 1992 SPE/DOE Eighth Symposium on Enhanced Oil Recovery, Tulsa, OK, April.

[68] Johns, R.T., Fayers, F.J. and Orr, F.M., Jr.: "Effect of Gas Enrichment and Dispersion on Nearly Miscible Displacements in Condensing/Vaporizing Drives," paper SPE 24938 presented at the 1992 SPE Technical Conference and Exhibition, Washington, D.C.

[69] Kalaydjian, F. J.-M.: "Performance and Analysis of Three-Phase Capillary Pressure Curves for Drainage and Imbibition in Porous Media," paper SPE 24878 presented at the 1992 SPE Technical Conference and Exhibition, Washington, D.C.

[70] Kalaydjian, F. J.-M., Moulu, J.-C., Vizika, O. and Munkerud, P. K.: "Three-Phase Flow in Water-Wet Porous Media: Determination of Gas/Oil Relative Permeabilities under Various Spreading Conditions," paper SPE 26671 presented at the 1993 SPE Technical Conference and Exhibition, Houston, TX.

[71] Kantzas, A., Chatzis, I. and Dullien, F. A. L.: "Enhanced Oil Recovery by Inert Gas Injection," paper SPE 17379 presented at the 1988 Sixth Symposium on Enhanced Oil Recovery, Tulsa, OK, April.

[72] Kantzas, A., Chatzis, I. and Dullien, F. A. L.: "Mechanisms of Capillary Displacement of Residual Oil by Gravity-Assisted Inert Gas Injection," paper SPE 17506 presented at the 1988 Rocky Mountain Regional Meeting, Casper, WY.

[73] Kantzas, A., Chatzis, I., and Dullien, F.A.L: "Mechanisms of Capillary Displacement if Residual Oil by Gravity-Assisted Inert Gas Injection," paper SPE 17506 presented at the 1988 SPE Rocky Mountain Regional Meeting, Casper, WY, May.

[74] King, M.J., Falzone, A.J., Cook, W.R., Jennings, J.W., Jr. and Mills, W.H.: "Simultaneous Determination of Residual Oil Saturation and Capillary Pressure Curves Utilizing Ultracentrifuge," presented at the 1990 SPE Annual Technical Conference and Exhibition, New Orleans.

[75] Koval, E.J.: "A Method for Predicting the Performance of Unstable Miscible Displacements in Heterogeneous Media," *Soc. Pet. Eng. J.* (June 1963) 145–154.

[76] Lake, L.W., Johnston, J.R., and Stegemeier, G.L.: "Simulation and Performance Prediction of a Large-Scale Surfactant/Polymer Project," *Society of Petroleum Engineers Journal* (December 1981) 731–739.

[77] Lake, W.L.: *Enhanced Oil Recovery*, first edition, Prentice Hall, Engelwood Cliffs, NJ 07632 (1989).

[78] Larson, G.L., Davis, H.T. and Scriven, L.E.: "Displacements of Residual Nonwetting Fluid from Porous Media," *Chem. Eng. Sci.* (1981) **36**, 75–81.

[79] Larson, R.G.: "The Influence of Phase Behavior on Surfactant Flooding," *Soc. Eng. Pet. Eng. J.* (December 1979) 411–422.

[80] LeBlanc, J.L. and Caudle, B.H.: "A Streamline Model for Secondary Recovery," *Society of Petroleum Journal* (March 1971) 7–12.

[81] Lenhard, R. J. and Parker, J. C.: "Estimation of Free Hydrocarbon Volume from Fluid Levels in Monitoring Wells," *Ground Water* (January–February 1990) **28**, No. 1, 57–67.

[82] LeVeque, R. J.: *Numerical Methods for Conservation Laws*, Birkhaeuser Verlag (1992).

[83] Leverett, M. C.: "Capillary Behavior in Porous Solids," *Trans., AIME* (1941) **142**, 152–169.

[84] Martin, J.C. and Wegner, R.E.: "Numerical Solution of Multiphase, Two-Dimensional Incompressible Flow Using Streamtube Relationships," *Society of Petroleum Engineers Journal* (October 1979) 313–323.

[85] Martin, J.C., Woo, P.T., and Wegner, R.E.: "Failure of Stream Tube Methods To Predict Waterflood Performance of an Isolated Inverted Five-Spot at Favorable Mobility Ratios," *Journal of Petroleum Technology* (February 1973) 151–153.

[86] Mishra, S.: *On the Use of Pressure and Tracer Test Data for Reservoir Description*, PhD dissertation, Stanford University, Stanford, CA (1987).

[87] Mohanty, K.K., Davis, H.T. and Scriven, L.E.: "Physics of Oil Entrapment in Water-Wet Rock," *SPE Reservoir Engineering* (February 1987) 113–128.

[88] Monroe, W.W.: "The Effects of Dissolved Methane on Composition Paths in Quaternary CO_2-Hydrocarbon Systems," Master's thesis, Stanford University, Stanford, CA (August 1986).

[89] Monroe, W.W., Silva, M.K., Larsen, L.L. and Orr, F.M. Jr.: "Composition Paths in Four-Component Systems: Effect of Dissolved Methane on 1D CO_2 Flood Performance," *Soc. Pet. Eng. Res. Eng.* (August 1990) 423–432.

[90] *Interfacial Phenomena in Petroleum Recovery*, N. Morrow (ed.), Marcel Dekker, Inc., New York (1991) Ch. 2, 23–76.

[91] Morrow, N.R. and Songkran, B.: "Effects of Viscous and Buoyancy Forces on Nonwetting Phase Trapping in Porous Media," *Surface Phenomena in Enhanced Oil Recovery*, D. Shah (ed.), Plenum Press, New York City, NY (1982) 387–411.

[92] Morrow, N.R., Chatzis, I. and Taber, J.J.: "Entrapment and Mobilization of Residual Oil in Bead Packs," *Soc. Pet. Eng. Res. Eng.* (1988) **3**, 927–935.

[93] Muskat, M.: *Principles of Oil Production*, McGraw Hill, Boston (1949).

[94] Neuman, S.: "Universal Scaling of Hydraulic Conductivities and Dispersivities in Geologic Media," *Water Resources Research* (August 1990) **26**, No. 8, 1749–1758.

[95] Oren, P. E. and Pinczewski, W. V.: "The Effects of Film Flow on Mobilization of Waterflood Residual Oil by Immiscible Gas Flooding," (May 21–23 1991) 6th European IOR Symposium, Stavager, Norway.

University of Toledo NMR Laboratory

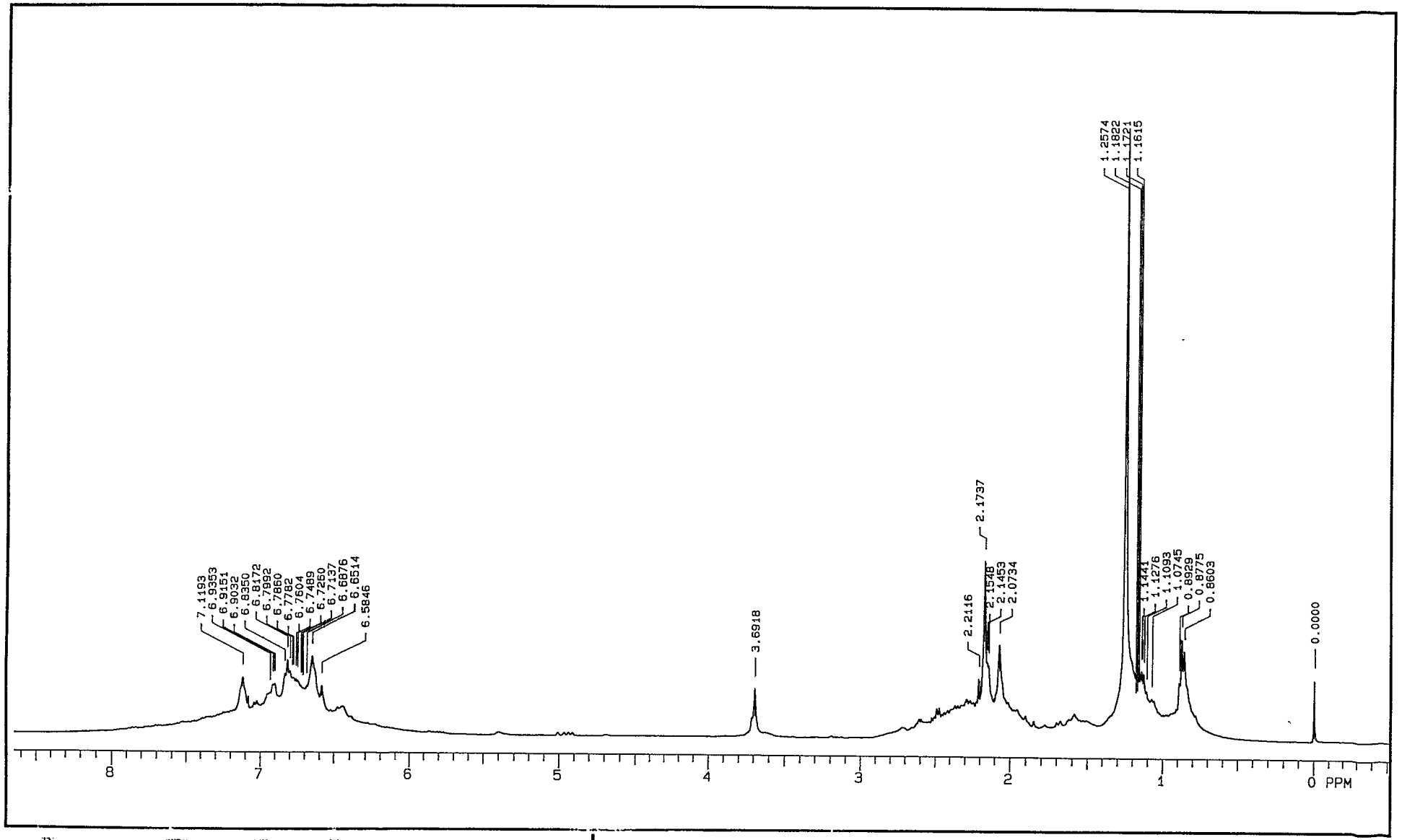

Acquisition

TN SFRQ MHz
SW Hz TOF Hz
AT sec D1 sec
PW μsec NT

Decoupling

DN DOF Hz
DM DLP dh
DMM DMF Hz
PI μsec DHP

Processing/Display

FN K RI sec CD
LB Hz M sec CCD
WP Hz ppm SP Hz ppm
Reference

Special

Pulse Sequence
Tube O D mm
Temp. °C

SAMPLE

Knife River CDL

Number
File
Date

12/12/1994 JSO (1)

UCRL-ID-118791

Facility Requirements to Test and Demonstrate a 6 MW Plasma Torch

M. C. Jackson and E. B. Hooper

October 4, 1994

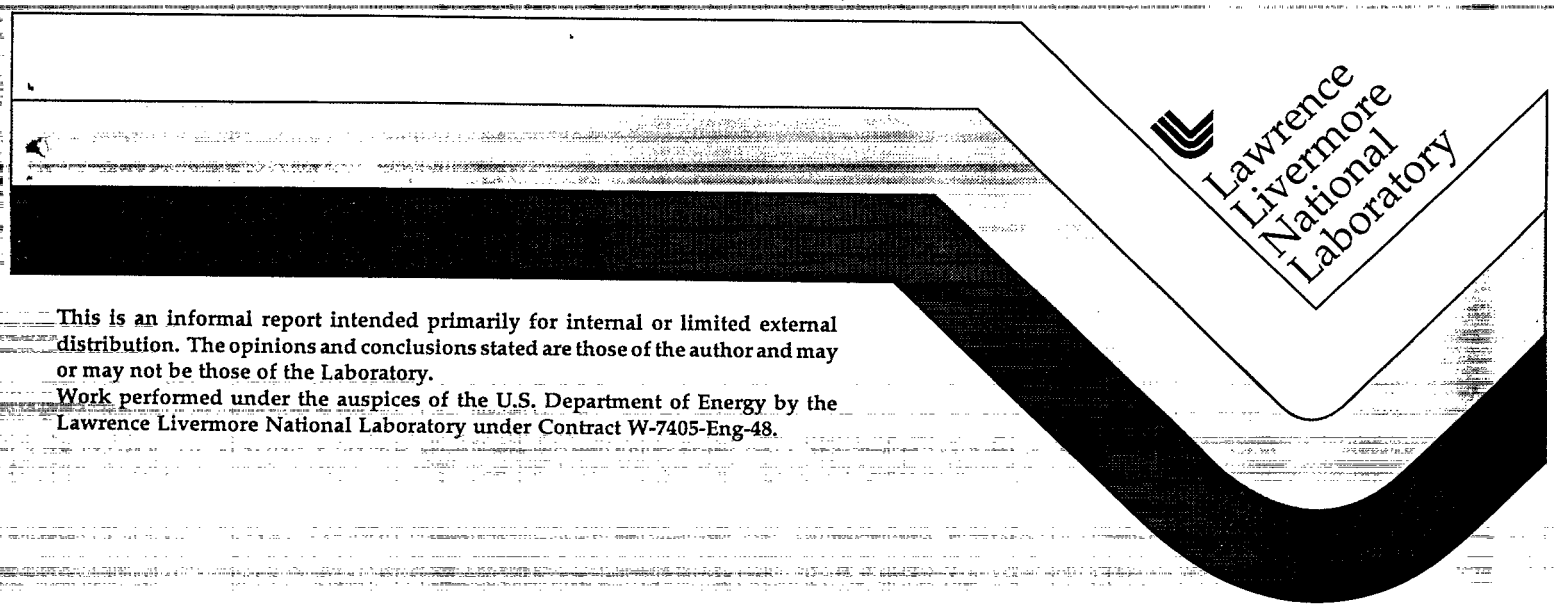

Work performed under the auspices of the U.S. Department of Energy by the Lawrence Livermore National Laboratory under Contract W-7405-Eng-48.

[127] Vizika, O.: "Effect of the Spreading Coefficient on the Efficiency of Oil Recovery with Gravity Drainage," Presented at the Symposium on Enhanced Oil Recovery, presented before the Division of Petroluem Chemistry, Inc., Denver, Colorodo (1993).

[128] Waggoner, J.R., Castillo, J.L., and Lake, L.W.: "Simulation of EOR Processes in Stochastically Generated Permeable Media," *Soc. Pet. Eng. Formation Eval.* (June 1992) 173–180.

[129] Walsh, B.W. and Orr, F.M. Jr.: "Prediction of Miscible Flood Performance: The Effect Of Dispersion on Composition Paths in Ternary Systems.," *IN SITU* (1990) **14**, No. 1, 19–47.

[130] Wilkinson, D.: "Percolation Effects in Immiscible Displacement," *Physical Review A* (1984) **30**, No. 1, 520–531.

[131] Wilkinson, D.: "Percolation Effects in Immiscible Displacement," *Physical Review A* (1986) **34**, No. 2, 1380–1385.

[132] Zauderer, E.: *Partial Differential Equations of Applied Mathematics*, second edition, Wiley-Interscience, New York, NY (1989).

[133] Zhou, D. and Blunt, M. J.: "Distribution of Light Non-aqueous Phase Liquid in Subsurface," unpublished (1994).

[134] Zhou, D. and Stenby, E. H.: "Displacement of Trapped Oil From Water-wet Reservior Rock," *Transport in Porous Media* (1993) **11**, 1–16.

[135] Zhou, D. and Stenby, H.E.: "Immiscible Displacement in a Porous Medium Simulated by a Statistical Model," *North Sea Oil and Gas Reservoirs-II* (1990).

[136] Zhou, D., Fayers, F.J. and Orr, F.M., Jr.: "Scaling Multiphase Flow in Simple Heterogeneous Porous Media," paper SPE 27816 presented at the 1994 Ninth Symposium on Improved Oil Recovery, Tulsa, OK, April.

☆U.S. GOVERNMENT PRINTING OFFICE: 1995 - 660-029/20003